Microfluidic Devices for Tissue, Cellular, Genetic and Proteomic Studies

By

Qiong Pan

A dissertation submitted in partial satisfaction of the

requirements for the degree of

Joint Doctor of Philosophy
with University of California, San Francisco

in

Bioengineering

in the

Graduate Division

of the

University of California, Berkeley

Committee in charge:

Professor Amy E. Herr, Chair
Professor Steven M. Conolly
Professor Bo Huang
Professor Gregory W. Aponte

Summer 2017

Abstract

Microfluidic Devices for Tissue, Cellular, Genetic and Proteomic Studies

By Qiong Pan

Joint Doctor of Philosophy

University of California, Berkeley

University of California, San Francisco

Professor Amy E. Herr, Chair

Microfluidic design forms a basis for precision measurements of even complex biological systems. Among the lines of inquiry that are thriving with the advent of microfluidic tools are biological mimetic tissues created “on-a-chip”. In this area, we have constructed a liver-on-a-chip system for drug hepatotoxicity screening. The liver-on-chip model is designed to include the liver’s sinusoid structure, oxygen diffusion, and the flow of nutrient supplies, in order to deliver a functional liver mimic for the study of drug metabolism. After design and fabrication of this organ mimic, we observed the liver-on-a-chip to yield improved hepatocyte life span and drug metabolism function, as compared to in vitro sandwich culture.

Cytometry – or single-cell resolution measurements – are another thriving line of inquiry. In cytometry, this dissertation research contributes three measurement aspects made possible with microfluidic tools: genomic processes (miRNA detection); targeted proteomics using electrophoresis, and function. By modeling and measuring the mass and heat transport processes limiting the precision of state-of-the-art cytometry tools, we optimize and validate a suite of new approaches. Specifically, in miRNA cytometry, we designed, fabricated, and demonstrated an isothermal quantification methodology that is coupled with microfluidic single-cell isolation, lysis, and amplification. The platform achieves high throughput and precise measurement of cell-to-cell miRNA levels. We analyzed miRNA expression in cancer cell lines and doxorubicin-resistant counterparts, which point to the existence of microRNA-dependent sub-population dynamics.

In cytometry of protein targets, we study a set of novel device architectures designed to minimize geometry-induced injection dispersion in electrophoresis of single-cell lysates. Single cells are commonly seated in microwells formed in hydrogels. Cells are chemically lysed in-situ, with the lysate subjected to electrophoresis in the surrounding gel. An analytical model was developed and experimentally validated to show that controlling both the geometry of the microwell and the thermodynamic partitioning characteristics of the microwell impact separation resolution and detection sensitivity.

Taken together, we establish a suite of microfluidic tools that mimic, manipulate, and measure processes important to factors that span from the protein to the genome, and from the cell to the whole organ.

In summary, this dissertation focuses on utilizing analytical chemistry and engineering approaches to advance microfluidic applications in tissue engineering and single-cell studies.

Acknowledgements

Scientific research is both enjoyable and challenging. During my graduate school, many people have accompanied me, helped and supported me in the pursuit of meaningful scientific contributions to our body of knowledge and the well being of the society.

First of all, I want to thank my thesis advisor Dr. Amy E. Herr. It was a privilege to be mentored by Amy. There is clearly so much effort, responsibleness and respectful working ethics involved in the whole research group and in our individual mentoring from Amy. I am grateful for her patient and concrete guidance, her words of reminders and encouragement, as well as her passion in helping the students and the whole society. I am also immensely benefited from her faithful upholding of scientific research standard that really helped me toward becoming a well-rounded researcher. There is still so much more to learn from Amy. I see myself taking a bigger leap than ever in every aspect of my research and professional development during the period of time with Amy.

Alongside, the positive and professional environment in the research group would be the result of her effort. With this, I would like to thank these extremely devoted scientists I had the pleasure to work with. It is through their joyful presence and kind-hearted support, as well as their persistent respect of scientific research standard, that I have gain fortitude to overcome challenges. Specifically, I would like to thank Dr. Chi-Chih Kang for her guidance when I first joined the lab, and her consistent help and communication about my research. I would like to thank Kevin Y. Yamauchi and Julea Vlassakis, who intellectually contributed generously to my research topics, and have been great examples of devoted scientists who take joy in challenges.

I would also like to thank the members of my qualifying exam and dissertation committees for their mentorship: Dr. Steven Conolly, Dr. Bo Huang and Dr. Gregory Aponte, for their generous and intriguing discussions about research, career and life.

I should also give thanks to Dr. Luke P. Lee, who had generously given me guidance and opportunities at the beginning stage of my research in Berkeley to explore beyond my previous expertise of analytical chemistry. His group introduced me to the attracting varieties of bioengineering applications, and greatly broadened my realm of research.

I want to also give my special thanks to my previous advisor Dr. Meiping Zhao in Peking University. Dr. Zhao introduced me to the field of microfluidics and had given me tremendous support and freedom in constructing our first microfluidic based assay. I am always grateful for her diligence and responsibleness in guiding me. Her gentle attitude toward the students and the fond memories in her group has left a deep impression in me and played part in shaping my character.

I am lucky that my family has always been supportive of my ventures. I want to thank my parents for their never-failing love and care for me. They may be quietly

working at the background, but it means so much to me. It is through them that I got the energy and courage to carry on through hard times. Their diligence, resilience, humbleness and positive attitude would be for me to learn in my whole life.

I was also fortunate to have friends whom I shared a lot of laughs with, which was special and effective remedy for challenges in graduate school. I am thankful for the presence of my friends in IGSM, my roommates who are also going through graduate school, and my family friends. Their friendship would be forever treasure for me.

Table of Contents

List of Figures and Tables

Chapter 1. Introduction

1.1 Microfluidics and Biology

The last two decades have seen a remarkable increase in interest in microfluidic lab-on-a-chip [1] or micro total analysis systems (μTAS), a field at the intersection of engineering and the life sciences. Microfluidics is defined as a device that handles and manipulates fluids at length-scales from one to one thousand microns with typical internal volumes of microliters to picoliters.

The advantages of microfluidics in biological applications include: smaller sample volumes or reagents are required due to the low fluid consumption [2]; the response times are remarkably faster due to the instantaneous reagent, heat transfer; offer high surface area-to-volume ratios as compared with macroscale containers and channels [3], reactions are also localized and can thus be compartmentalized leading to an unparalleled amount of control and safety [4, 5].

Applications of microfluidics on biological studies ranges from molecule (small molecule, protein and gene materials), sub-cellular organelles, single-cells, cell clusters as well as tissues. For example, in electrophoretic sample separation and detection on microfluidic devices, trace amount of sample is needed for measurement due to the small diffusion length scale. Higher electric field and a faster separation is available without deleterious effects of excessive diffusion or bubble formation. Furthermore, Microfluidic platforms not only can automate existing assays , but can also enable new types of measurements not previously possible. Single-cell level studies are the fields that are obviously benefited from microfluidics. Due to the precise and automatic fluidic control available in small length scale microstructures, automatic or semi-automatic, efficient single-cell handling is possible. The detection sensitivity also has the potential to be improved due to the limited dilution factors in microfluidic scale. Finally, microfluidics can also allow the study of human physiology in a physiologically realistic manner, due to its promotion in controlling variables that mimic cellular microenvironment as well as its response to various treatments. This allows bypassing of animal models [6] and conventional cell culture methods, which are unable to capture the structural, mechanical complexities of in vivo testing [7].

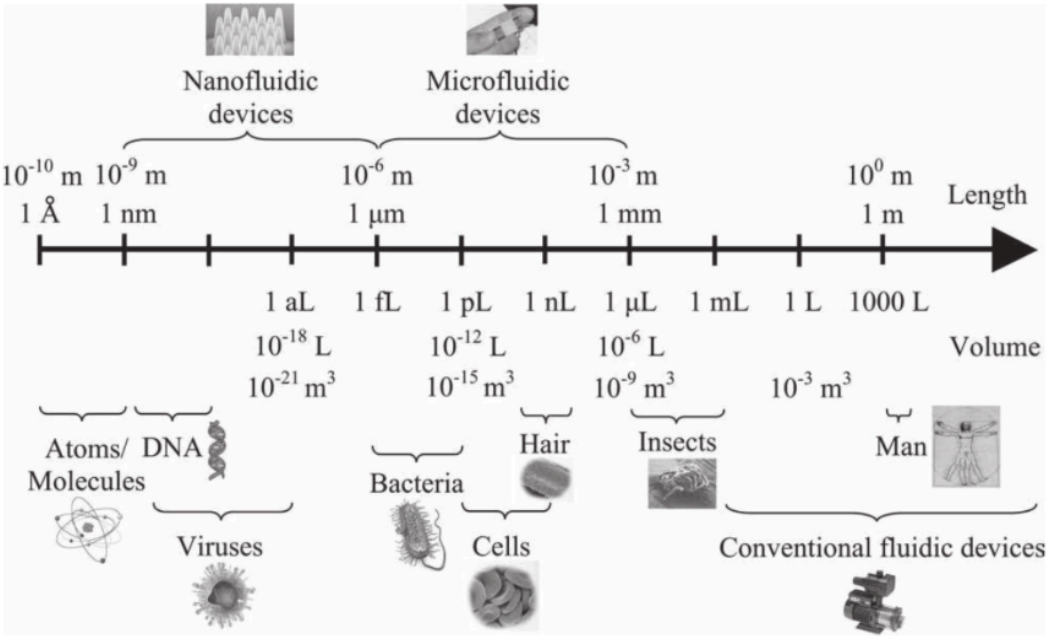

Figure 1.1 Scale of microfluidic devices ranges from single-atom/molecule level to single-cells, up to tissue, organ and even human level [8].

1.2 Single-cell Protein & Gene Measurement

A central challenge of biology is to understand how individual cells process information and respond to perturbations [9]. Much of our current knowledge is based on ensemble measurements. However, cell-to-cell differences are always present to some degree in any population of cells, and the ensemble behaviors of a population may not represent the behaviors of any individual cell. This heterogeneity from single-cells exists on proteomic level, genomic level as well as cellular and intercellular level. The population based cell measurement reflects the collective responses but obscures the individual cell behavior. Therefore, sensitive and precise single-cell resolution proteomic tools are desired [10].

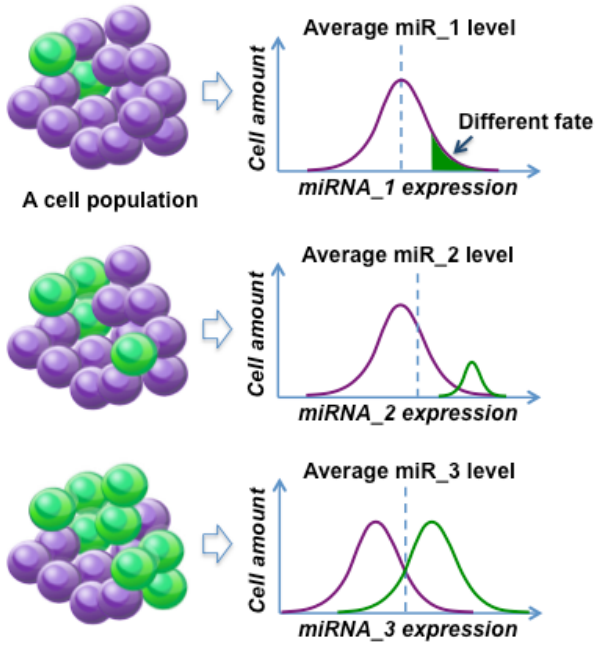

Figure 1.2 Single-cell heterogeneity is obscured by population-based measurements. Our single cell work does not suffer from this blurring of two populations.

As shown in Figure 1.2, even with a simple bell-shaped distribution of single-cell gene measurements, the high or low expression of a certain gene may represent dramatically different transcriptional states [9]. However, if we only measure the population based gene level, we will miss this distribution variation. An even more problematic situation is when the population-based measurement poorly reflects the internal states of the majority of the cells or any subpopulation of cells. Also, population based gene measurements can mask the presence of a rare subpopulations of cells. In this case, a population mean may represent the vast majority of cells. Therefore, capturing single-cell level difference among a population is a more accurate and informational method than population-based measurements.

Obtaining a statistically significant number of single-cell information is also essential to understand the cellular processes and their responses. Gene expression heterogeneity is essentially a statistical property of cellular populations. In Figure 1.3, we show an example of miRNA expression level from various amount of single cells. As we increase the number of cells being analyzed, we gradually see the unique three distinguishable peaks, indicating sub-populations, which have different miRNA expression level. Therefore, the ability to handle a large number of individual cells in a high-throughput manner is critical.

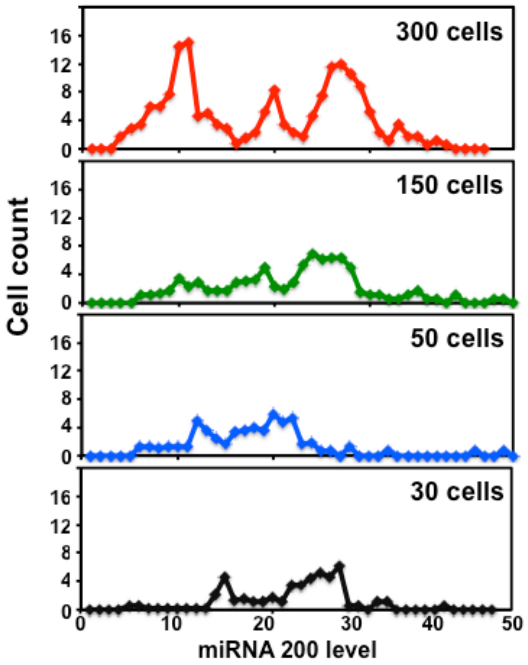

Figure 1.3 Sub-populations of cancer cells MCF7, which express different levels of miRNA 200 are revealed when analyzing large number of single cells.

1.3 Protein Electrophoresis

Proteins are intricate biomolecules that embody an enormous range of structural and functional diversity. Large interacting networks of proteins and other biomolecules determine biological outcomes. For researchers to deconstruct the complexity present in biological systems, there is a need for platforms that can conduct concurrent-analysis of multiple samples with multiplexed protein readouts.

Measurements to identify specific proteins can be performed using affinity reagents, for example antibodies or aptamers, or through mass spectroscopy based protein sequencing, or through protein microarrays. In affinity reagents, antibodies typically cannot distinguish between the protein of interest and isoforms or non-specific interactions, and their affinity can easily degrade over time [11]. Analytical protein separations are routinely used to fractionate complex mixtures of proteins by physiochemical parameters – such as charge, size [12], isoelectric point [13], hydrophobicity [14], or solubility [15]. Protein separations can be used to dramatically accelerate the detection of an affinity reagent [16].

The most effective and widely used protein separation method is through electrophoresis. The velocity of a particle in the presence of an electric field (E) is dictated by the relative electrophoretic force, $F_{EP}=qE$, and a Stokes drag force, $F_{drag}=6\pi\eta rU$. Where r is the particles hydrodynamic radius, U is the particle velocity, and η is the dynamic viscosity of the solution. Therefore, the particle velocity, $U= qE/6\pi\eta r$. The electrophoretic mobility of a particle (μ), is defined as

the velocity normalized by the applied electric field, $\mu = q/6\pi\eta r$. In a solution of different particles the 1/6πη term is typically constant. Therefore electrophoresis fractionates particles by their charge and size, q/r.

It needs to be noted that this is an oversimplification. For example, the effective charge of a particle in solution is dictated by the interaction between the particle and the ions in the solution - specifically, the formation of an electrical double layer. Usually, the injected sample zone experience molecular diffusion during separation. The protein concentrations follow Gaussian distribution over a period of separation due to diffusion. The process of diffusion can be estimated by the Stokes-Einstein equation, which defines a diffusion constant as the ratio of thermal energy to Stokes Drag, $D = k_B T/6\pi\eta r$. Where D is the diffusion constant, k_B is the Boltzmann's constant, and T is the absolute temperature. Since the peak intensity distribution along the separation axis follows Gaussian distribution due to diffusion, the one dimensional peak dispersion is defined as the square of a peak intensity distribution's standard deviation, $\sigma^2 = 2Dt + \sigma_0^2$ and is linearly related to time.

Electrophoretic separations at the most basic level consist of three phases, (1) injection, (2) separation, and (3) readout. Each phase plays an important role in the overall performance of the separation. For microfluidic or miniaturized electrophoresis, we introduce examples of two formats: microfluidic capillary electrophoresis and sieving hydrogel based electrophoresis. Figure 1.4 depicts a separation of a typical microfluidic capillary electrophoresis format [17]. The T-channel consists of orthogonal channels, one for the injection and another for the separation. In-channel electric field profiles are controlled with electrodes at all four channel reservoirs. To inject the sample, an electric field profile is used to drive the current from one performance by limiting the injection dispersion to within the width of the injection channel. After injection, the electric field profile is changed to initiate separations along the separation channel. The two species are separated by their differential electrophoretic velocities. To detect the separation either a plot profile is taken to observe the species concentration over length, for example using epi-fluorescence and a CCD camera, or an electropherogram is taken to observe the species concentration over time at a single point along the separation axis.

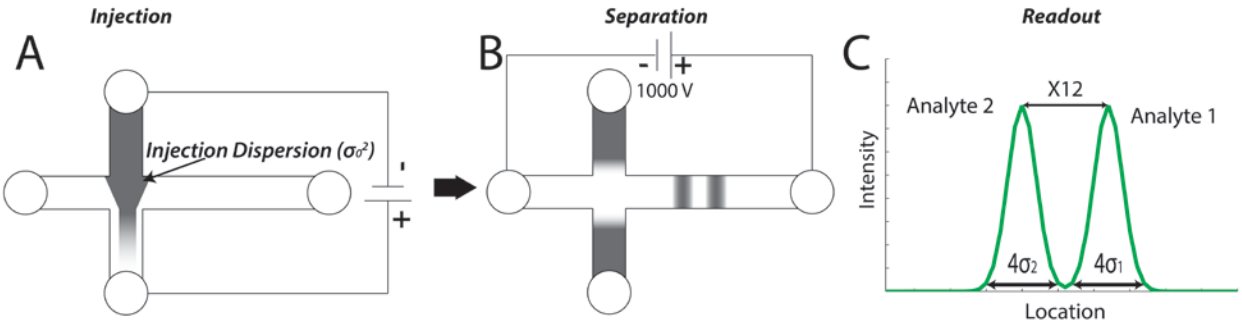

Figure 1.4 Microfluidic capillary electrophoresis procedure and detection [17]. There are three key steps of a complete analysis: (A) Sample injection, (B) Electrophoretic separation, (C) Signal readout.

Another category of protein electrophoresis is slab hydrogel electrophoresis. One state of the art separation matrix in this category is Polyacrylamide gel electrophoresis (PAGE) [12]. Polyacrylamide gel is a nano-porous hydrogel which acts as a sieve that impedes proteins on the basis of their size and structure. The polymer [$(\text{-}CH_2CHCONH_2\text{-})_n$] is made through a free-radical reaction from a precursor solution containing an acrylamide monomer [CH_2=CHCONH$_2$] and a crosslinker, typically methylene bisacrylamide [$(H_2C$=CHCONH$)_2CH_2$]. The nano-pore size of the gel and effective sieving properties can be tuned by simply modifying the concentration of its monomers. Figure 1.5 depicts a typical PAGE separation format [18]. The PA gel between two glass plates are set up on an electrophoresis stand with surrounding running buffer and electrodes applied at the top and bottom end. Proteins are loaded into the top sample slots. After applying electric field, protein bands are separated on the basis of relative molecular weight. The detection of protein bands can be done by dye staining or immunostaining. A most effective way of protein detection from a hydrogel is through a procedure called western blot [19]. In western blot, proteins are transferred onto a nylon / nitrocellulose membrane. The molecules are immobilized (fixed) on the membrane. The membrane will then be incubated with antibodies that are complimentary to the target proteins. Afterwards, fluorescent secondary antibodies are applied to visualize protein bands.

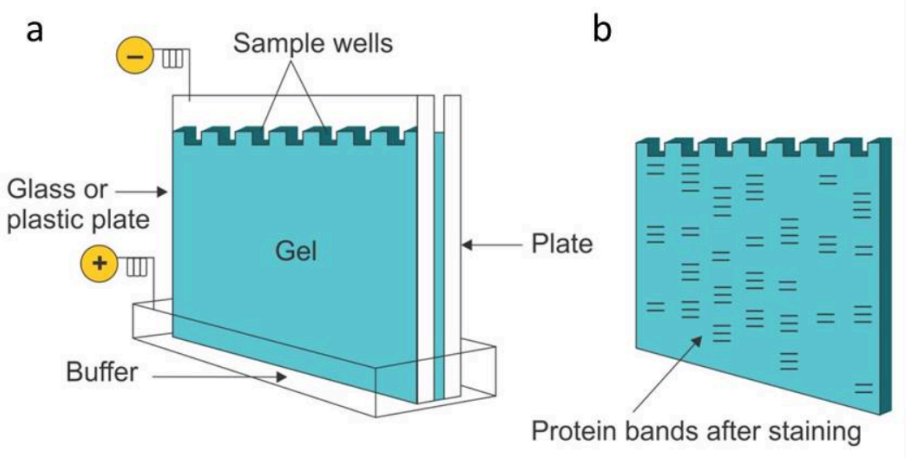

Figure 1.5 Polyacrylamide gel based protein electrophoresis setup, procedure and protein visualization [18]. Proteins are separated by their molecular weight in the gel and are detected by antibody probing after protein spot being transferred onto a nylon/ nitrocellulose membrane.

The performance of an electrophoretic protein separation can be evaluated by separation resolution (SR). SR is defined as the distance between the mean of two species (ΔL) normalized by the average peak width (4σ) of each species, SR $=\Delta L/ (2\ \sigma_1+2\ \sigma_2)$. For an electrophoretic separation, this equation can be expanded with the key control parameters of electrophoresis:

$$SR = \frac{(\mu_1 - \mu_2)\, Et}{4\sqrt{2Dt + {\sigma_0}^2}}$$

The strategies to improve separation performance can be dependent on several parameters: As the separation time or differential mobility is increased so does the separation performance. Conversely, as the diffusion constant or injection dispersion is increased, the separation performance is reduced. As the applied electric field relates to both an increase in separation distance between species and an increase in the rate of diffusion (via joule heating) a balance must be reached between separation speed and heat dissipation. In microfluidics the high surface to volume ratio allows for the efficient heat dissipation and for the electric field to be increased to higher values before consequences in increased diffusion rates are observed.

1.4 Tissue Engineering and Organ-on-a-chip

In pharmaceutical industry, there is a clear need for improvement of the predictive power of preclinical studies through more accurate modeling of human physiology. To meet this need, organ-on-a-chip technology was hatched through the convergence of two areas of research: microfluidics and tissue engineering [20]. Organs-on-a-chip mimic the functions and structure of organs of living human beings by compartmentalizing specific cell lines into microchambers and dynamically perfusing waste and nutrients. It provides the tool to analyze an organ's functionality and malfunctions in case of diseases. Although biological constructs are inherently complex and to fully mimic and deliver their functionality would be challenging, we can attempt to construct organs that represent the key functions that are essential for drug tests. Shuler et al. formulated the following basic tenets to modelling of living systems [21] by organ-on-a-chips:

1. The replication a physiologically realistic ratio of cell mass from one tissue to another.
2. The mimicking of the flow split of blood during recirculation of a blood surrogate.
3. The correct residence time of fluid in an organ/tissue compartment is established.
4. Shear stress flow rates that are maintained within a physiologic range.
5. A physiological ratio of free liquid to cells, and finally
6. The chip emulates an authentic biological response of cells.

Putting forward, integrated systems with multiple microscale cellular environments can be designed to simulate the human body and make new predictions about the pharmacokinetics of new drugs [22]. However, mimicking the true physiological complexity of the human body's four major aspects of activities- absorbing, distributing, metabolizing, and eliminating (known as ADME) across multiple organs is much more complex than simply connecting various cellular environment. One of the key to achieving this is the proportional scaling of each organ model to reflect the actual physiological relationships between

them [20].

Recently, heart-on-chips [23], together with nephron-on-chip [24], gut-on-a-chip [25] and Lung-on-a-Chip [26] are several successful examples in our organ-on-a-chip endeavor. For example, the heart-on-a-chip consists of a multi chamber array that replicates the tissue architecture in the heart [23]. By modelling the electric impulses controlling the heart rate, Grosberg et al. were able to investigate the biological structure-to-function relationship. Artery-on-a-chip developed by Guenther et al permits the on-chip fixation, long-term culture and automated acquisition of dose-response sequences of intact mouse artery segment [27].

Microfluidic organ-on-a-chip has been advancing rapidly. From Figure 1.7, the number of publications found from the search for each corresponding year was plotted from 2000 to 2015. The rise in publication exemplifies the increasing activity and interests in the respective field.

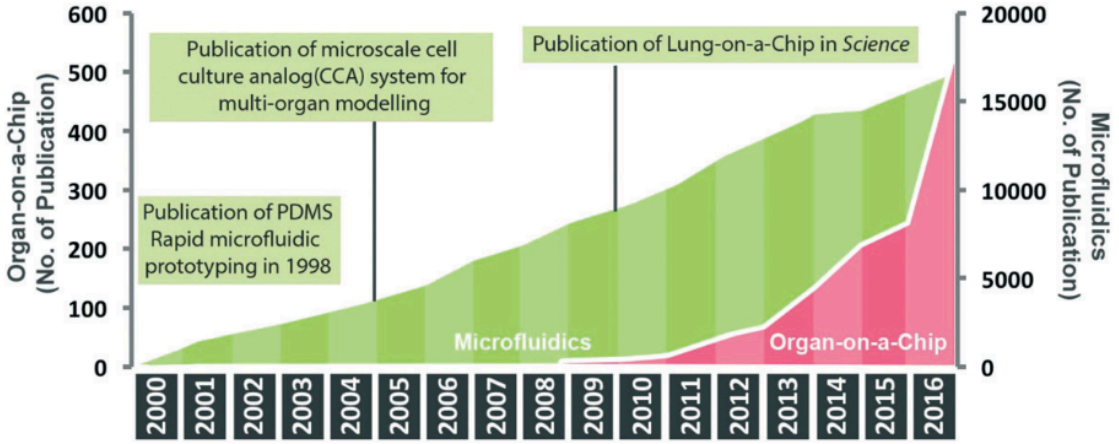

Figure 1.6 Rise in academic publishing in organ-on-a-chip space. The key word "Microfluidics" or "Organ-on-a-Chip" was searched on Google scholar [20].

1.5 Organization of This Thesis

This thesis is divided into 6 chapters. Chapter 1 provides background information on this multidisciplinary research area. In addition, it states and defines the problem that this thesis tries to solve. In chapter 2, we describe a liver-on-chip system for drug hepatotoxicity screening using primary human hepatocytes, and potentially extend to using human induced pluripotent stem cells for personalized medicine development. The liver-on-chip model is designed to better resemble the real liver sinusoid structure to deliver a closer functionality for drug metabolism. Our constructed liver-on-a-chip improved hepatocyte life span and function. We have also tested drug metabolism from the waste media with mass spectrometry.

In chapter 3 we describe a single-cell level co-culture platform for studies of dynamic cellular interactions. In this platform, heterotypical pairing in a single-cell

level is achieved through sequential cell trapping and dynamic variation of fluidic resistance. The device is capable of maintaining and tracking embryonic stem cell and fibroblast pairs for several generations. We observed the interaction between the single-cell pairs and found that heterotypic pairing led to distinct proliferation patterns from homotypic single-cell culture.

In chapter 4, we describe an isothermal single-cell miRNA quantification platform that reveals the heterogeneous miRNA regulation of cancer cells. We presente an N^2 amplification method that gives linear end-point fluorescent signals versus microRNA concentration. This method combining with a flow-cell based single-cell isolation, lyses, miRNA capture and amplification platform, gives more precise and high throughput single-cell miRNA quantification. We analyzed microRNAs expression in human breast cancer cell line MCF-7 and their change of distribution in doxorubicin-resistant cells and presented microRNA-dependent sub-populations dynamics.

In chapter 5, we describe the geometry-induced injection dispersion in electrophoretic cytometry. Injection, as one of the three major processes in microfluidic electrophoresis, has tremendous effect on peak dispersion. Specifically, injection curvature from various shapes of microwells affects band spreading. We used analytical simulation and experimental validation to study the controlling factors on injector shape dependent peak dispersion. We found that an increase in geometry of injectors or electric field enlarges the differences between various injector shapes, whereas in separations with smaller injectors and low electric fields, the shape of injector does not play a significant role in the final separation performance.

In chapter 6, we describe a single-cell PAGE device innovation using patterned polyacrylamide gels to control the performance of single-cell electrophoresis by tackling diffusion. We also designed a heat-minimized microfluidic PAGE configuration that does not cause temperature increase upon high voltage application, which prevents heat-induced peak dispersion. A 3-fold increase in protein resolution and a >2 fold increase in detection sensitivity was achieved in detecting trace amount of proteins in single-cells.

References

[1] Manz, A., Graber, N., Widmer, H. M., Sensors and Actuators B, 1990, 1, 244–248.
[2] Agresti, J. J., Proc. Natl Acad. Sci. USA 2010, 107, 4004–4009.
[3] Huh, D., Torisawa, Y.-S., Hamilton, G. A., Kim, H. J., Ingber, D. E., Lab on a Chip, 2012, 12, 2156–2164.
[4] Young, Edmond W. K., Beebe, D. J., Chemical Society Reviews, 2010, 39, 1036–1048.
[5] Burke, J. M., Smela, E., Biomicrofluidics, 2012, 6,16506–1650610.
[6] Whitesides, G. M., Nature, 2006, 442, 368–373.
[7] Moraes, C., Mehta, G., Lesher-Perez, S. C., Takayama, S., Annals of Biomedical Engineering, 2012, 40, 1211–1127.

[8] Yeo, L. Y., Chang, H. C., Chan, P. P. Y., Friend, J. R., Small, 2011, 7, 12-48.
[9] Altschuler, S. J., Wu, L. F., Cell, 2010, 141, 559–563.
[10] Hanahan, D., Weinberg, R. A., Cell, 2011, 144, 646
[11] Saper, C. B. J Comp Neurol, 2005, 493, 477-478.
[12] Maizel, J., Jacob, V., Trends in Biochemical Sciences, 2000, 25, 590-592.
[13] Vesterberg, O., Biochimica et Biophysica Acta (BBA) - Protein Structure, 1972, 257, 11-19.
[14] Queiroz, J. A., Tomaz, C. T., Cabral, J. M. S., Journal of Biotechnology, 2001, 87, 143-159.
[15] Bordier, C., Journal of Biological Chemistry, 1981, 256, 1604-1607.
[16] Duncombe, T. A., Herr, A. E., Analytical Chemistry, 2012, 84, 8740-47.
[17] Harrison, D. J., Manz, A., Fan, Z., Luedi, H., Widmer, H. M., Analytical Chemistry, 1992, 64, 1926-1932.
[18] Seidman, L. A., Moore, C. J., Basic Lab Methods for Biotechnology, Prentice Hall, New Jersey, 2009.
[19] Burnette, W. N., Analytical Biochemistry, 1981, 112,195–203.
[20] Zhang B. Y., Radisic, M., Lab on a Chip, 2017, 17, 2395-2420.
[21] Shuler, M. L., Annals of Biomedical Engineering, 2012, 40, 1399–1407.
[22] Huh, D., Geraldine A. H., and Donald E. I., Trends in Cell Biology, 2011, 21, 745-754.
[23] Anna, G., Alford, P. W., McCain, M. L., Parker. K. K., Lab on a Chip, 2011, 11, 4165–4173.
[24] Weinberg, E., Kaazempur-Mofrad, M., Borenstein, J., The International Journal of Artificial Organs, 2008, 31, 508–514.
[25] Kim, H-J., Huh, D., Hamilton, G., Ingber, D. E., Lab on a Chip, 2012, 12, 2165–2174.
[26] Huh, D., Matthews, B. D., Mammoto, A., Montoya-Zavala, M., Hsin, H. Y., Ingber, D. E., Science, 2010, 328, 1662–1668.
[27] Axel, G., Yasotharan, S., Vagaon, A., Lochovsky, C., Pinto, S., Yang, J. L., Lau, C., Voigtlaender-Bolz, J., Bolz., S. S., Lab on a Chip, 2010, 10, 2341–2349.

Chapter 2. Liver-on-chip for High Throughput Drug Hepatotoxicity Screening

2.1 Introduction

Drug development in pharmaceutical industry is a high-risk activity. In the initial phase of drug discovery, we narrow down thousands of compounds to a few hundred promising candidates for pre-clinical testing. In this stage, scientists conduct laboratory and animal studies to determine whether a compound is suitable for human testing. At the end of this process, approximately five compounds move to the next stage, clinical trials in humans [1]. These compounds will be sent to the stage of clinical trial. During this stage, a compound is tested in human volunteers. The clinical trials process occurs in several phases and takes on average six to seven years [2]. The increasing expense of drug development contributes to escalating healthcare costs [1]. The drug development expense has increased over the past 20 years, however, the number of drugs approved annually was declining [3, 4]. It usually takes nearly 2.5 billion dollars and 10–12 years on average to develop one clinically applicable drug [5]. Two thirds of the total drug development costs are spent in the clinical trial stage [6].

Furthermore, the current pre-clinical models are cell culture based and animal based. Studies [7] also revealed that small interspecies sequence differences at the genome level can lead to major physiological differences in drug specificity, activity and toxicity between species. Therefore, the traditional drug developmental models of single cell screening and animal testing often fail to predict drug effects observed at the human clinical trial stage [6, 7]. Drug candidates that may have significant effect on major disease challenges may have high risk of side effects [8-11]. Among the side effects that lead to drug failure, cardiac and liver toxicities are the main causes of post-approval drug withdrawals [12, 13].

Therefore, there is a clear need for improvement of the predictive power of preclinical studies through more accurate pre-clinical modeling of human physiology [14]. To meet this need, organ-on-a-chip technology [15-18] was developed with the collaboration of microfluidics and tissue engineering.

Organs-on-a-chip and human-on-a-chip technology -- built using microfluidic fabrication techniques – may make a positive impact here [19, 20]. We thus have the capability to build complex physical environments emulating the normal organ environment of the cells. Stem cell biology can provide easy access to patient-specific stem cells and tissues, making this technology more relevant to human and even patient-specific. Organ on a chip provides a 3D micro-environment of assembly of co-cultured tissues [21, 22], supplemented with topographical

structures [23], mechanical forces [24-26], biochemical gradient [27, 28] etc. that better represents the real tissue, on the structure as well as function level [29-33]. Unlike animal testing, in these miniaturized tissue models we can directly access cells within their tissue architecture to probe their functional change under drug stimulation in real time [34].

Scientists have built several tissue and organ types on chip in the recent years [35]. Lung-on- a-Chip platform that mimics the alveolar-capillary interface was built to study the progression of cystic fibrosis under various oxygen supply conditions [36]. Heart-on-a-chip was also developed that consists of a multi chamber array that replicates the tissue architecture in the heart [37]. By modelling the electric impulses controlling the heart rate, Grosberg et al. were able to investigate the biological structure-to-function relationship. Artery-on-a-chip developed by Guenther et al permits the on-chip fixation, long-term culture and automated acquisition of dose-response sequences of intact mouse artery segment [38]. Besides, nephron-on-chip [39], gut-on-a-chip [40], as well as liver-on-a-chip [68, 69] are also developed and showed competitive functional behavior as real tissue.

Liver metabolism plays a central role in the clearance, modification and incidental toxicity of most xenobiotics [42]. Consequently, drug induced liver toxicity and unpredicted drug metabolisms are major causes of drug withdrawal. About 30% of failed compounds are due to hepatotoxicity in human [41]. Fialuridine, a potential treatment for hepatitis B that failed clinical trials in the early 1990s because it was found to cause severe toxicity in humans — an effect that had not been predicted in animal studies [14]. Preclinical hepatotoxicity test usually uses either microscopic human cell lines, which are altered to live forever, or animal models, which are costly and often fail to predict human response. Therefore, primary human cells that are not genetically modified need to be used as test target. However, due to change of microenvironment, primary human cells often failed to maintain its functions in vitro or cannot give physiologically relevant result. Hepatocyte cells separated from the liver quickly decreases its function within 24 hours [42]. Moreover, these cells cannot proliferate in vitro, thus the resource of samples is limited. Microfluidics provides a possible route to use limited amounts of cells to build physiologically relevant human micro-tissues that is possible to resemble real organ function and response to test drugs.

With the discovery of patient-specific human induced pluripotent stem (hiPS) cells [43-45], one can generate disease/ individual-specific hiPS cells from fibroblasts and regenerate various tissue cell types that carry the genetic information of the disease or the individual. We are now in position to develop in vitro disease specific model tissues and organs to be used for high content drug screening and patient specific medicine. The cell source (human fibroblast) is largely available and hiPS cells have the ability to proliferate infinitely. Therefore hiPS differentiation provides unlimited source of different organ cell types. One can envision a bank of hiPS cells that represent the genetic information of a population, and candidate compounds from pharmaceutical research can be tested among these representatives for various organs' response, including

hepatotoxicity. In this way, the risk of clinical trials can be largely limited and the test pool with hiPS derived organs on chip can be much bigger than human volunteers. Ideally, the human liver-on-chip could have an enormous impact on the early screening of candidate drugs with low cost, short turn over time and better prediction of pharmacokinetics and pharmacodynamics [46].

By using microfluidic technique, we aim to create a liver sinusoid mimetic microstructure that can be constructed for liver cell culture with primary hepatocytes, and eventually with patient- specific iPS derived hepatocytes. This liver-on-chip model is expected to better resemble the real liver function and its response to test compounds. We expect that the liver-sinusoid mimetic high throughput platform can facilitate the cost and time efficient drug hepatotoxicity test for pharmaceutical drug screening before human tests.

2.2 Design Principles of Liver-on-chip Model

To attempt to delineate their functionality, Shuler et al. formulated the following basic tenets to modelling of living systems [47] by organ-on-a-chips:

1. The replication a physiologically realistic ratio of cell mass from one tissue to another.

2. The mimicking of the flow split of blood during recirculation of a blood surrogate.

3. The correct residence time of fluid in an organ/tissue compartment.

4. Shear stress flow rates that are maintained within a physiologic range.

5. A physiological ratio of free liquid to cells.

And as the final evaluation, the chip must emulate an authentic biological response of cells.

Liver sinusoid structures contain multiple layers of hepatocytes, along which are endothelial cell layers. Liver tissue contains very sufficient blood flows with hepatic portal vein and artery. The well-functioned hepatocytes are very compact, forming tight junctions and bile canaliculus. The design and optimization of microfluidic device needs to mimic key components of liver sinusoid structure:

1. Sufficient blood flow to ensure nutrient and oxygen exchange,

2. Endothelial cell barriers to reduce shear pressure on hepatocytes and

3. Compact connection of hepatocytes to form tight junctions.

Thus, we sought to deliver the above three key function-related-structure characterisitics with microfluidics. The microfluidic design shown in Figure 2.1 contains cell culture chambers separated by endothelial-like barriers from media flow channel. Hepatocytes can be loaded into culture chambers and form multiple layers of 3D structures. Design of the device geometry is informed by simulation of nutrients and the oxygen supply. The resulting device ensures

uniform nutrient supply from culture media and sufficient gas transfer from culture atmosphere.

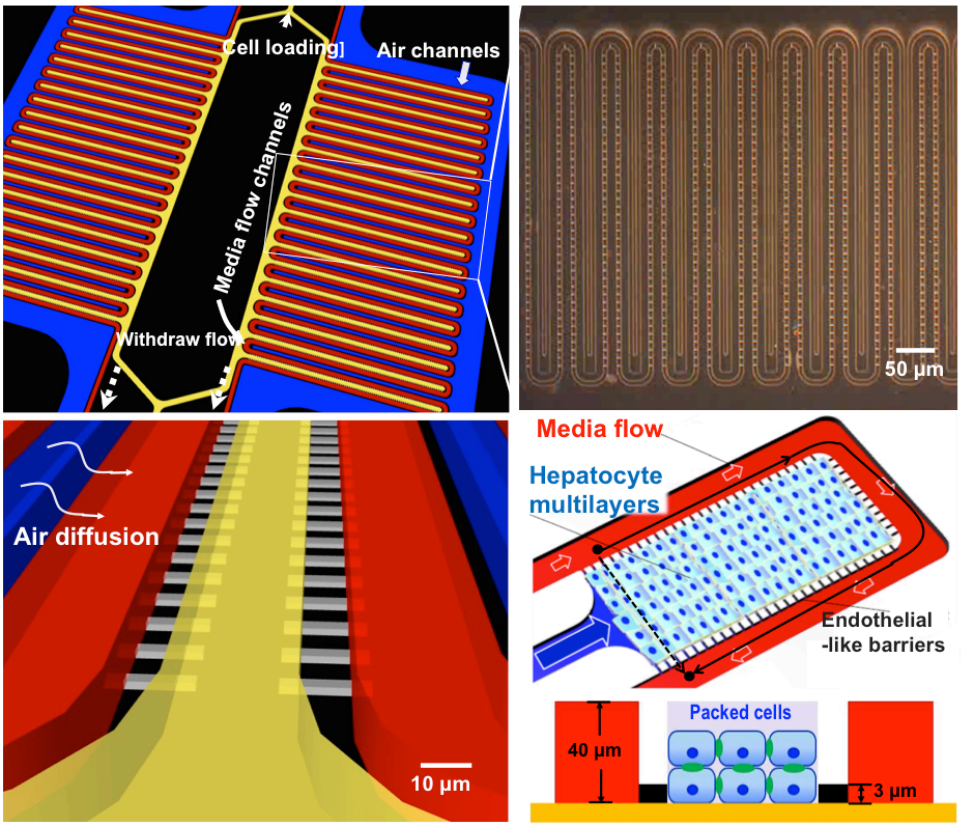

Figure 2.1 Liver-on-chip model design. Liver cell culture chambers are separated from media channels by endothelial-like barriers which have open slits of 8 μm width and 3 μm height. Due to this barrier, nutrient supply is mainly through passive diffusion. The device also contains air diffusion channels, which are 50 μm away from the cell culture chamber to ensure sufficient oxygen supply via diffusion through the porous material PDMS.

The liver-on-a-chip microstructure was made of PDMS attached to a functionalized glass slide. The backbone consists of three main channels: cell culture channels, media channel and air diffusion channels. The cell culture channel was designed to have an array of pockets (40 μm x 100 μm) that are surrounded by media channel (40 μm x 60 μm) and air diffusion pockets (40 μm x 120 μm), simulating the liver sinusoid structure. All the cell culture pockets were connected to a main cell-loading channel. The media and cell culture channels are connected with arrayed shallow slits (8 μm x 3 μm x 15 μm, 22 μm spacing) for media diffusion (Figure 2.1). The air diffusion channel is connected to atmosphere. There is a distance of 50 μm from media channel, allowing oxygen to diffuse through the porous PDMS material into culture media. During cell loading, hepatocytes are loaded at the inlet of the main cell-loading channel. And the media channel outlet was connected to syringe pump that withdraw media

from the cell loading channel through the shallow slits, thus creating a negative pressure causing cells loaded into pockets.

After cell loading, an optimized media flow speed (0.1 µL/min, 0.83 mm/ sec in main media channel) was applied by adjusting the liquid level of the two media inlets at the ends of media channel. This creates consistent gravity-driven flow to replenish media. Prior to cell seeding, the liver chip was sterilized by UV irradiation, and channels were coated with collagen gel (3 µg/mL).

The device is designed to enable single-cell-type culture (hepatocyte culture) or potentially cell co- cultures with endothelial cells and Kupffer cells to improve hepatocyte functions. The device will need to be tested for multiple cell type loading and culture protocols need to be optimized accordingly.

We sort to mimic the blood flow with the media supply around and into the liver sinusoid. Several choices of media supply mechanism are compared below [48]. We chose gravity driven flow due to its low pressure and consistency in flow supply for long periods of time of several days to weeks. Certainly, the media level needs to be adjusted on a daily basis to ensure flow rate.

System	Advantages	Disadvantages
Gravity Driven	Numerous solvents Consistent Flow	Non-Adjustable flow rates
Pressure Driven	Higher flow rates pressure	External pump required
Electrokinetic	Flat Velocity Profile	Limited to conductive solvents only Additional surface modification

Table 2.1 Comparison of various fluid driven methods in microfluidic cell culture.

To make sure that nutrient and oxygen is sufficiently supplied to cells, we have performed simulations on the device to model both the fluid (liquid) flow and the oxygen concentration (Figure 2.2). The media supply should suffice the minimum nutrient consumption rate of 10-40 fmol/ cell·day from the estimated 2000 cells per culture chamber. The simulation is based on a nutrient concentration of 25 mM in media supply and a media flow rate of 0.1 µL/ min (linear speed 0.83 mm/ sec). Steady state oxygen gradients can be established through the cultured liver structure by balancing the axial transport rate of dissolved oxygen and the cellular oxygen consumption rate (OCR). It is shown in Figure 2.2 B that the oxygen supply through 5 mm thick PDMS device layer will cause oxygen depletion at the bottom of cell culture. We designed an oxygen supply channel adjuncent to (50 µm) cell culture channel. Based on an oxygen consumption rate of 3.8×10^{-6} mol/ cell·day, this design provides near-physiological gradients of the dissolved oxygen concentration.

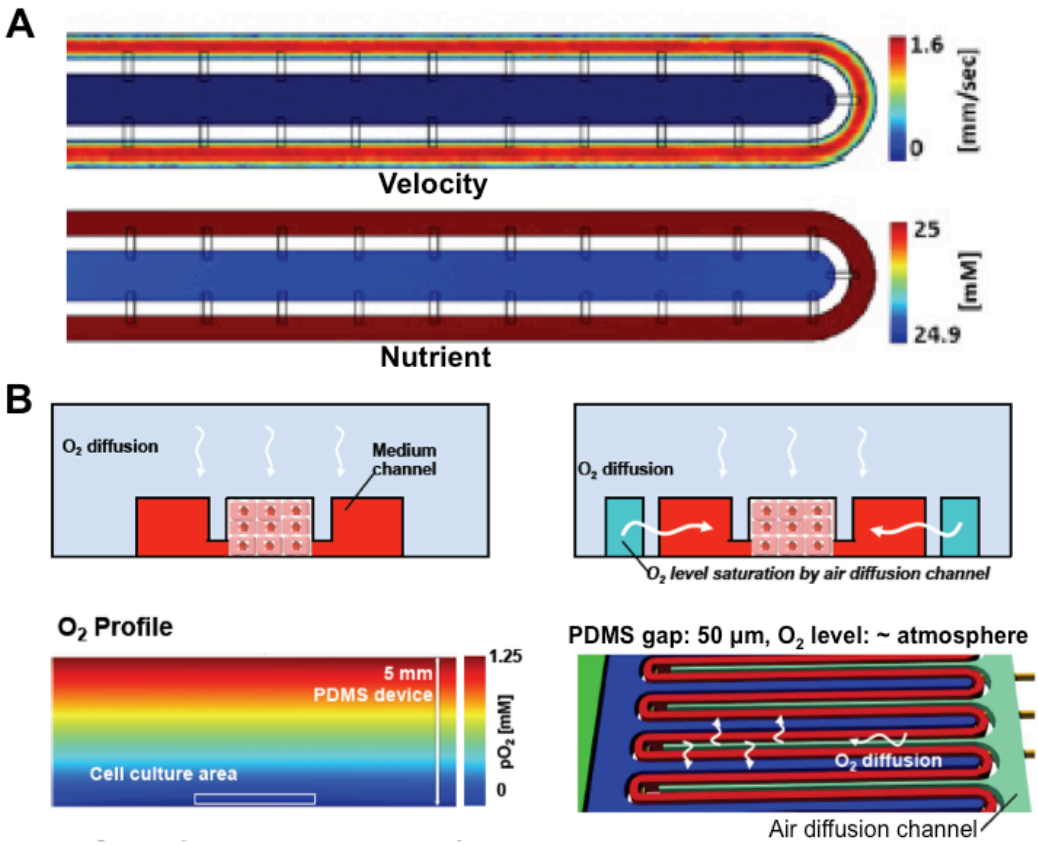

Figure 2.2 Simulation and rationale of the device design. (A) Nutrient supply simulation based on culture condition. While the velocity of flow is almost zero in culture chamber, passive diffusion ensures the nutrient supply is sufficient. (B) Oxygen supply simulation indicates a lack of oxygen through 5mm thick porous material PDMS. By creating air diffusion channel next to media channel (distance 50 μm), oxygen can be sufficiently supplied.

In many organisms, oxygen is the final electron acceptor during the process of cellular respiration and energy production in the mitochondria [49]. In cells and tissues, inadequate levels of oxygen result in physiological and metabolic changes. Therefore, adequate oxygen supply is an important factor to consider in choosing microfluidic device materials and design.

2.3 Experimental Materials and Workflow

Primary hepatocytes were iCell® Hepatocyte from Cellular Dynamics Inernational (Madison, WI) [50]. The hepatocytes are highly purified human hepatocytes derived from induced pluripotent stem cells. They are tested for AAT, Albumin, and ASGPR purity markers and demonstrate functional responses through transporter activity, intrinsic metabolism, Phase I and Phase II metabolism, and viral infectivity. The Pre-commercial iCell Hepatocytes are shipped as a live cell

product in an optimal medium for assays. It is important to note that the cells remain only for 5 days for viability and function.

Before experiments, newly arrived iCell hepatocytes are pelleted by centrifugation and resuspended in complete media prior to seeding. The resuspended cells were seeded into the cell pockets of the liver chip and allowed to attach to each other and the device surface for 2 hours under static conditions. Attached cells were then perfused with complete media by a syringe pump at a volumetric flow rate of 0.1 μL/min, at 37 ^{o}C and 5 % CO_2.

For in-vitro dish culture of hepatocytes, we applied the most commonly used sandwiched collagen culture protocol. Tissue culture dishes were coated with 0.5 mL of a mixed solution containing parts of rat-tail collagen (1.1 mg/mL in mM HCl) and 10 Dulbecco's modified Eagle Medium (DMEM) and incubated for 1 hour at 37 ^{o}C to form a collagen gel. After gelation, one million hepatocytes (12.5 × 103 cells/cm^2) were seeded in 2 mL hepatocyte culture medium and incubated in 90% air/10% CO_2 at 37 ^{o}C. To achieve uniform densities, the substrates were shaken every 15 minutes for the first hour after cell seeding. The following day, the culture medium was removed and a second collagen gel layer was overlaid on the hepatocytes and incubated for 1 hour at 37 ^{o}C. After gelation, 2 mL of hepatocyte culture medium was applied. The culture medium was changed daily. The hepatocyte culture medium consisted of DMEM supplemented with 10% fetal bovine serum (Life Technologies Inc., Gaithersburg, MD, USA), 7.5 g/mL hydrocortisone (Pharmacia Co., Kalamazoo, MI, USA), 0.5 U/mL insulin (Eli Lilly, Indianapolis, IN, USA), 20 ng/mL epidermal growth factor (Sigma Aldrich Co., St. Louis, MO, USA), 200 U/mL penicillin, and 200 g/mL streptomycin (Life Technologies Inc.).

To stain hepatocytes on chip, we replaced the culture media with primary antibody solutions diluted in PBS and perfuse through hepatocyte clusters in the device at 0.1 µL/ min for 30 mins, and fluorescent labeled secondary antibody was applied using the same way. Afterwards, the device was washed with PBS for 30 mins before imaging.

To harvest cells for RT-PCR gene expression measurement, we used RNeasy Mini Kit from Qiagen (Cat No. 74104). We used the Buffer RLT from the kit for on chip cell lyses and lysate harvest. Buffer RLT was perfused through the device using a speed of 0.5 µL/ min. The cells are disrupted and lysed inside the device and the resulted cell lysate was flowed into the outlet and was harvested for cDNA production and PCR.

To harvest media for drug metabolism measurement, depending on the frequency of measurement, either a 10 µL/ hour or a 100 µL/ day of media with constant concentration of drug phenacetin was added to the media supply inlet, while a 10 µL/ hour or a 100 µL/ day of waste media containing the drug metabolites are collected from the waste outlet. We tried to keep the media height difference comparatively constant to ensure stable flow, by supplying a consistent 300 µL media at the inlet and taking out the waste media with a

capillary guide. The collected waste media was immediately processed and subjected to LC/ MS for mapping.

2.4 Hepatocyte Function Characterization

Primary hepatocytes are reported to sustain in-vitro culture for different periods of time due to the culture methods. Hepatocytes cultured in suspension can last for 6 hours [51] for drug test, and 1-2 weeks in a sandwich culture format for simple function characterization such as urea secretion and albumin secreation [52, 53]. In other studies, hepatocytes are cultured as spheroids for 20 days, and exhibit function of albumin and urea secretion, as well as CYP enzyme function for 5 days [54]. Co-culturing hepatocytes with 3T3-J2 fibroblasts maintained viability for 2 weeks with several tests of drug metabolism with bile canaliculi and enzyme function [55, 56]. There has not been a record of primary hepatocyte culture on chip that maintained extensive period of functions, including drug metabolism.

The function of liver-on-chip constructed with primary hepatocytes can be tested and compared with the most popular sandwich culture on several aspects: albumin secretion, hepatocyte function gene marker expression, metabolism enzyme level and finally drug metabolism test [56]. Although the primary hepatocytes used in the preliminary experiment are tested to maintain its function for 5 days under optimal culture condition, the results on this microfluidic device indicated that hepatocytes cultured on chip have sustained their viability for up to 15 days. Figure 2.3 shows the Calcium AM stain of hepatocytes on chip (green) at 15 days. The PI stain (red) showed minimum cell death in this long term culture.

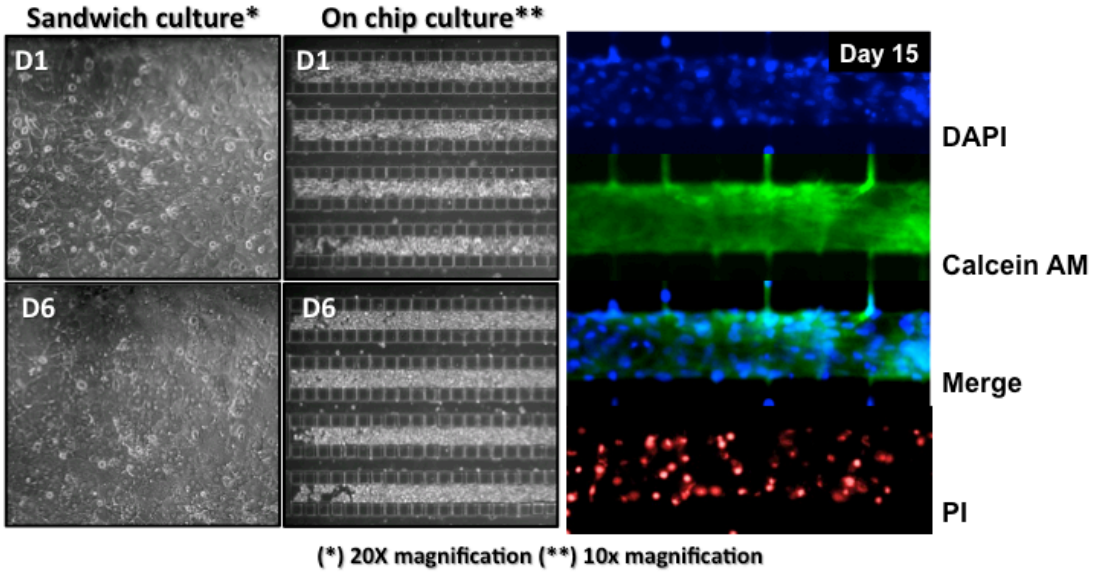

Figure 2.3 Primary hepatocyte on chip culture functions. At 15th day of culture, hepatocytes remain viable.

Besides, on chip cultured hepatocytes exhibit better performance on recovery of albumin secretion (Figure 2.4). It is shown that on chip cells secretes albumin more homogeneously and evenly, whereas in normal dish culture, albumin secretion only exist in few cells among the population. The amount of albumin secreted was also calculated depending on the seeding density. The albumin secretion was consistently high for up to 8 days on chip. At day 9, the albumin secretion function dropped drastically. The reason for this drop of albumin secretion needs further investigation.

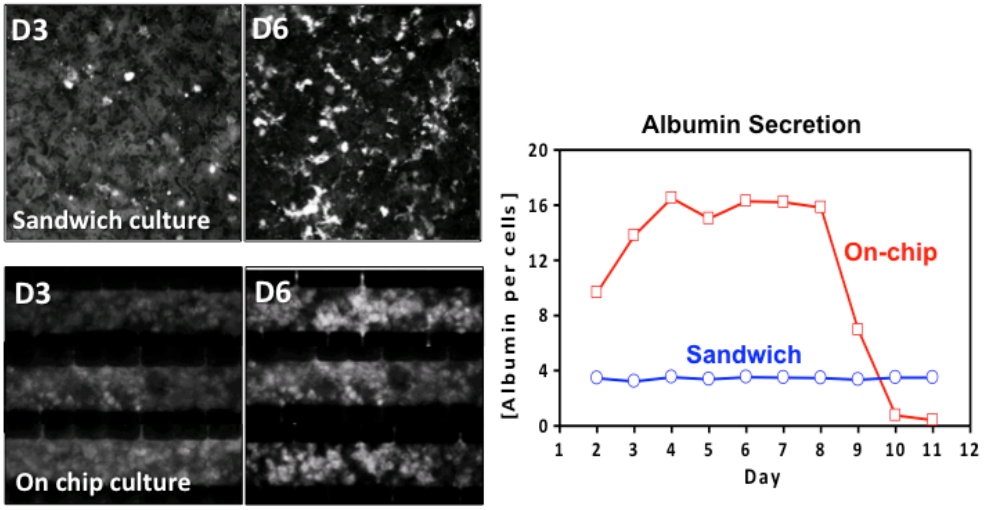

Figure 2.4 Primary hepatocytes cultured on chip rapidly increase albumin secretion and maintained a high level albumin for 8 days. At day 9, the albumin secretion function dropped drastically. The reason for this drop of albumin secretion needs further investigation. Sandwich culture remains a consistent low albumin secretion level.

Several structural and functional gene expressions are the common measures of hepatocyte functions. Among them, we have measured several structural proteins to examine the cell-cell interaction as tight connection (junction) between cells is an important indicator of liver sinusoid function. Occludin is an indicator of tight junction formation, as well as tight junction protein 1 (Tjp1). Microfluidic culture shows a quicker recovery of occluding and overall higher level of Tjp1 than conventional dish culture (Figure 2.5). Drug metabolism enzymes are key candidates of test in drug toxicity test on liver-on-a-chip. We have measured the Phase I enzymes multidrug resistance protein (MRP2) and cytochrome P450 1A2 (CYP 1A2) expression levels over 12 days of culture (Figure 2.4). It also showed that microfluidic cultured cells have higher level of these enzyme expression than dish culture. The above gene expression experiments are performed with RT-PCR after cells are harvested from device.

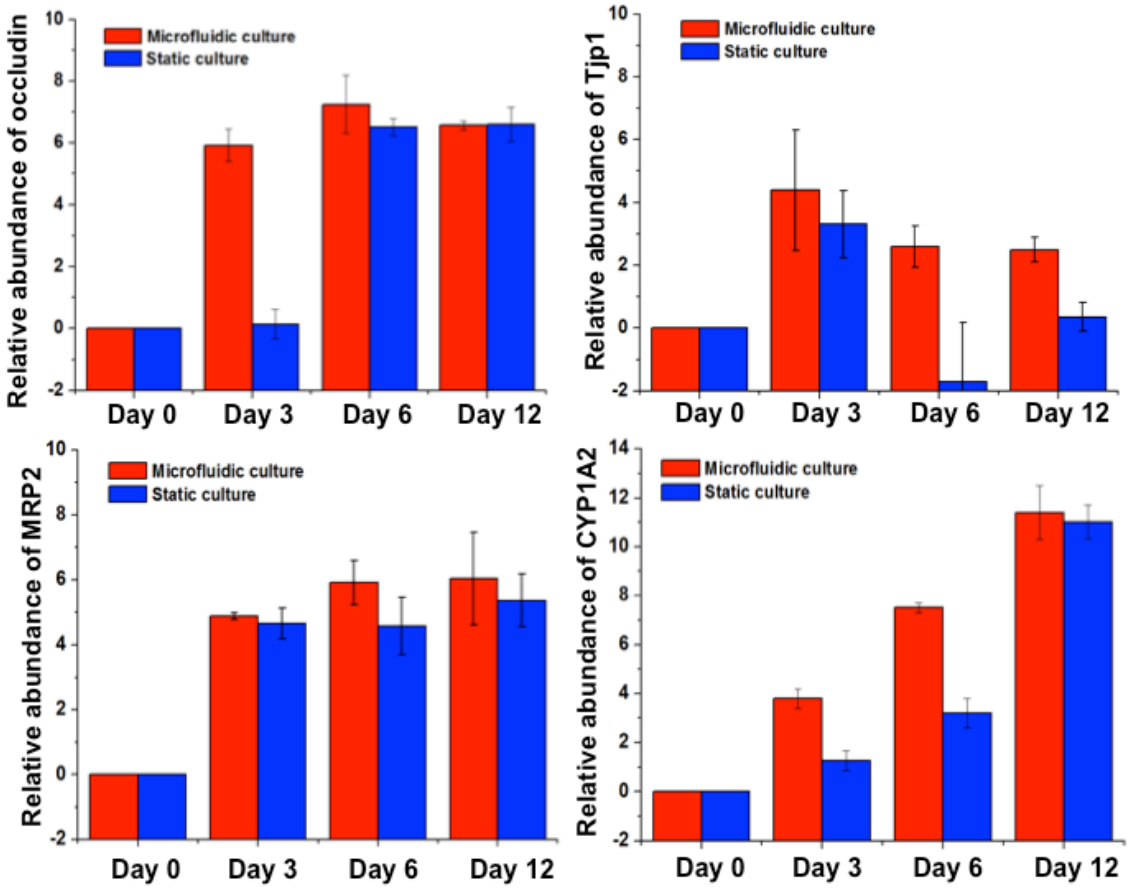

Figure 2.5 Gene expression levels measured by off-chip PCR indicate favorable functional gene expressions with on-chip culture over sandwich culture. The genes measured are: tight junction indicating genes occludin and tight junction protein 1 (Tjp1), as well as metabolism enzymes multidrug resistance protein 2 (MRP2) and cytochrome P 450 1A2 (CYP 1A2).

2.5 Drug metabolism study with liver-on-a-chip

Next, we compared the drug metabolites from liver-on-a-chip culture and dish sandwich culture. We chose a traditional analgesic drug phenacetin. Figure 2.6 shows the in vivo metabolism pathways of phenacetin. In vivo, the drug is extensively metabolized and less than 0.5% of a dose is recovered unchanged in the urine. The major metabolic route is through dealkylation to form acetaminophene (60-80%), and minor pathways include deacetylation and hydroxylation to form p-phenetidine, 2-hydroxyphenetidine, 2- and 3-hydroxyphenacetin and N-hydroxyphenacetin. These metabolites are excreted largely as conjugates in the urine [57-65]. In animals and in man the deacetylation of phenacetin is dose-dependent with a marked relative increase in the production of p-phenetidine and 2-hydroxyphenetidine at higher doses [61, 64]. The toxicity of phenacetin is related to its metabolism.

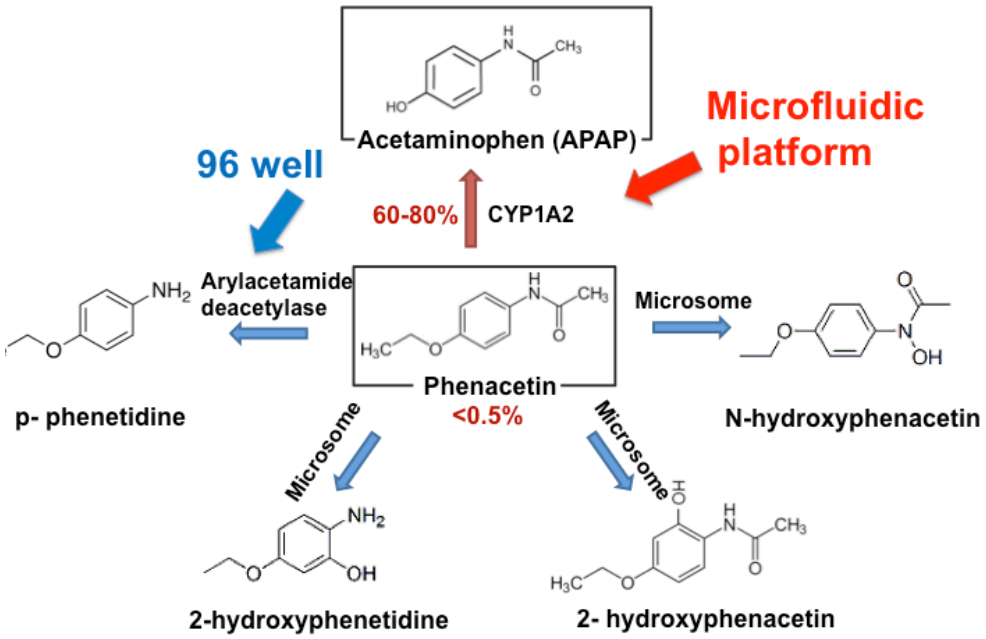

Figure 2.6 Phenacetin in vivo metabolism pathways. The main product of phenacetin in the liver is acetaminophen (APAP), which constitutes 60-80% of the total metabolites through the enzyme CYP1A2. Several other minor pathways for phenacetin include p-phenetidine through arylacetamide deacetylase, 2-hydroxyphenetidine, 2-hydroxyphenacetin and N-hydroxyphenacetin via microsome. The microfluidic liver-on-a-chip hepatocytes mainly produced APAP, while the sandwiched culture mainly produced the side product p-phenetidine.

Several approaches for liver drug metabolism function tests include:

1. Drug toxicity by mitochondria activity test TC50: MTT assay
2. Drug metabolism mapping: LC-MS for waste media
3. Drug interactions & enzyme activity induction: chemical induction and mitochondria activity test

Here, we have compared phenacetin metabolism on chip and in sandwich culture by mapping the metabolite in waste media by LC-MS (Figure 2.7). The results show dramatic decrease of phenacetin after 2 days of treatment on chip, however, phenacetin level increases in sandwich culture, indicating an accumulation of the non-metabolized drug components (Figure 2.8). We measured several metabolites from the waste media by mass spectrum. These measurements showed that on chip culture produces the normal metabolite APAP as the main metabolite while sandwich culture mostly produces p-phenetidine (Figure 2.9). Comparing the pathways, it is implied that on chip hepatocytes metabolites the drug phenacetin through the in-vivo pathway, whereas the sandwich culture failed to exhibit the in-vivo drug metabolism functions of liver sinusoid. Other drug metabolism function tests can be included for future studies, such as mitochondria activity test and enzyme activities after drug treatment.

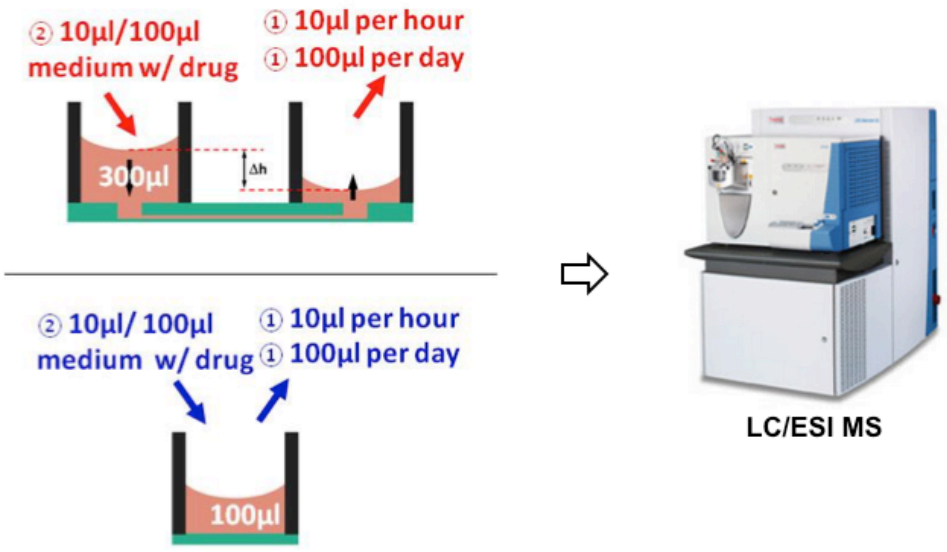

Figure 2.7 Operation procedure for drug phenacetin metabolism measurement with LC/ESI MS. Depending on the frequency of measurement, either a 10 µL/ hour or a 100 µL/ day of media with constant concentration of drug phenacetin was added to the media supply inlet, while a 10 µL/ hour or a 100 µL/ day of waste media containing the drug metabolites are collected from the waste outlet. The collected waste media was immediately processed and subjected to LC/ MS for mapping.

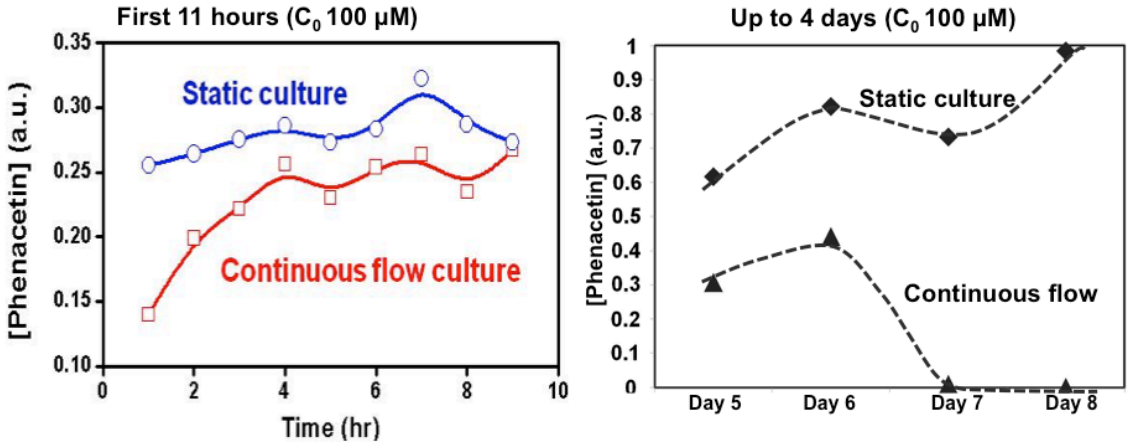

Figure 2.8 Phenacetin concentration at the waste media outlet during the first 11 hours of culture and up to 4 days. Liver-on-a-chip design exhibit decrease of the drug concentration over long period of time, indicating effective metabolism of the drug.

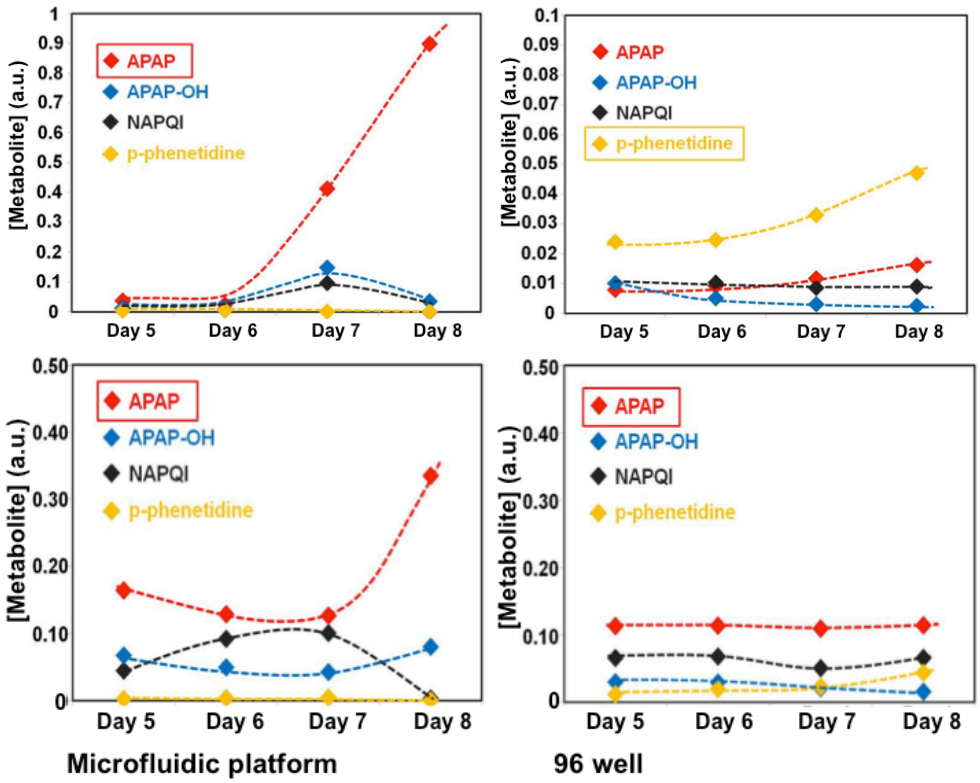

Figure 2.9 Comparison of phenacetin metabolism on chip and in sandwich culture indicates that on-chip culture results in the activation of *in-vivo*-like drug metabolism pathways and produce *in-vivo-like* drug metabolites, whereas sandwich culture activates liver-toxic metabolism pathways.

2.6 Conclusion

With liver-on-chip, we are able to improve hepatocyte life span and function. Signaling from other cell types co-exist with hepatocytes in vivo is important for hepatocyte function maintenance, such as kupffer cells and endothelial cells. Achieving co-culture within the device can be beneficial. Drug hepatotoxicity and its IC 50 correlation with in vivo were tested. More hepatocyte function related tests can be done with the current liver-on-chip construction. The assays include: hepatocyte viability test for cytotoxicity assessment; antioxidative enzyme activity measurement for oxidative stress assessment; bile fluorescent staining for cholestasis; GSH quantification for glutathione depletion and mitochondrial membrane potential assay for mitochondrial dysfunction.

The vision of constructing micro-tissue or organs on chip is to integrate different organs from one cell source into one connected platform to mimic human response of test compounds. hiPS cell of one individual can be differentiated to create necessary cell types. These cell types can be organized within microfluidic devices into mimetic structures that perform similar as in vivo. With physiological relevant distribution of flow within connected microchannels, drug metabolism and its effect on inter- connected organs can be comprehensively studied. This

could potentially eliminate large amount of animal testing and reduce the risk of human clinical trials.

References:

[1] Ingrid T., The Pharmaceutical Journal, 2015, 12.
[2] https://www.fda.gov “The drug development process”.
[3] Adams, C. P., Brantner, V. V., Health Econ., 2010, 19, 130–141.
[4] Kinch, M. S., Merkel, J., Drug Discovery Today, 2015, 20, 920–923.
[5] DiMasi, J. A., Grabowski, H. G., Hansen, R. W., J. Health. Econ., 2016, 47, 20–33.
[6] Paul, S. M., Nat. Rev. Drug Discovery, 2010, 9, 203–214.
[7] Mak, I., Evaniew, N., Ghert, M., Am. J. Transl. Res., 2014, 6, 114–118.
[8] Osherovich, L., Science- Business eXchange, 2013, 6, 1-2.
[9] Harrison, D. C., Winkle, R., Sami, M., Mason, J., Am. Heart J., 1980, 100, 1046–1054.
[10] Echt, D. S., N. Engl. J. Med., 1991, 324, 781–788.
[11] Manning, F. J., Swartz, M., Review of the fialuridine (FIAU) clinical trials, National Academies, 1995.
[12] Piccini, J. P., Am. Heart J., 2009, 158, 317–326.
[13] Graham, D. J., Lancet, 2005, 365, 475–481.
[14] Baker, M., Nature, 2011, 471, 661–665.
[15] Huh, D., Torisawa, Y.-S., Hamilton, G. A., Kim, H. J., Ingber, D. E., Lab Chip, 2012, 12, 2156–2164.
[16] El-Ali, J., Sorger, P. K., Jensen, K. F., Nature, 2006, 442, 403–411.
[17] Bhatia, S. N., Ingber, D. E., Nature, 2014, 201, 4.
[18] Esch, E. W., Bahinski, A., Huh, D., Nat. Rev. Drug Discovery, 2015, 14, 248–260.
[19] Yamanaka, S., Cell, 2009, 137, 13–17,
[20] Soldner, F., Jaenisch, R., Science, 2012, 338, 1155–1156.
[21] Huh, D., Science, 2010, 328, 1662–1668.
[22] Stevens, K., Nat. Commun., 2013, 4, 1847.
[23] Chiu, L. L., Montgomery, M., Liang, Y., Liu, H., Radisic, M., Proc. Natl. Acad. Sci. U. S. A., 2012, 109, E3414–E3423.
[24] Hirt, M. N., Basic Res. Cardiol., 2012, 107, 1–16.
[25] Fink, C., FASEB J., 2000, 14, 669–679.
[26] Zhang, B., Peticone, C., Murthy, S. K., Radisic, M., Biomicrofluidics, 2013, 7, 044125.
[27] Rodenhizer, D., Nat. Mater., 2016, 15, 227–234.
[28] Allen, J. W., Bhatia, S. N., Biotechnol. Bioeng., 2003, 82, 253–262.
[29] Capulli, A., Lab Chip, 2014, 14, 3181–3186.
[30] Hutson, M. S., Appl. In Vitro Toxicol., 2016, 2, 97–102.
[31] Wikswo, J. P., Exp. Biol. Med., 2014, 239, 1061–1072.
[32] Huh, D., Hamilton, G. A., Ingber, D. E., Trends Cell Biol., 2011, 21, 745–754.
[33] Zheng, F., Small, 2016, 2253–2282.
[34] Zhang, B. Y., Radisic, M., Lab on a chip, 2017, 17, 2395-2420.

[35] Huh, D., Geraldine A. H., Ingber, D. E., Trends in Cell Biology, 2011, 21, 745-754.
[36] Huh, D., Matthews, B. D., Mammoto, A., Montoya-Zavala, M., Hsin, H. Y., Ingber, D. E., Science, 2010, 328, 1662–1668.
[37] Anna, G., Alford, P. W., McCain, M. L., Parker, K. K., Lab on a Chip, 2011, 11, 4165–4173.
[38] Axel, G., Yasotharan, S., Vagaon, A., Lochovsky, C., Pinto, S., Yang, J. L., Lau, C., Voigtlaender-Bolz, J., Bolz, S-S., Lab on a Chip, 2010, 10, 2341–2349.
[39] Weinberg, E., Kaazempur-Mofrad, M., Borenstein, J., The International Journal of Artificial Organs, 2008, 31, 508–514.
[40] Kim, H. J., Huh, D., Hamilton, G., Ingber, D. E., Lab on a Chip, 2012, 12, 2165–2174.
[41] Senn, J., Drug Safety Evaluation, Millennium Pharmaceuticals, 2010.
[42] Kidambi, S., Nahmias, Y., PNAS, 2009, 105, 15714–15719.
[43] Takahashi, K., Yamanaka, S., Cell, 2007, 131, 861–872.
[44] Yu, J., Thomson, J. A., Science, 2007, 318, 1917-1920.
[45] Hannan, N. R. F., Nature Protocols, 2013, 8, 430-437.
[46] Huh, D., Ingber, D. E., Science, 2010, 328, 1662-1668.
[47] Shuler, M. L., Annals of Biomedical Engineering, 2012, 40, 1399–1407.
[49] Charis, E., Kiuru, M., Fernandez, M. J., Aaltonen, L. A., Nature Reviews Cancer 3, 2003, 193-202.
[50] Hannan, N. R. F., Nature Protocols, 2013, 8, 430-437.
[51] Obach, R. S., Drug Metab Dispos, 1997, 25, 1359-1369.
[52] Dunn, J.C., Yarmush, M. L., Koebe, H. G., Tompkins, R. G., FASEB J, 1989, 3, 174–177.
[53] Wu, F. J., Friend, J. R., Hsiao, C. C., Zilliox, M. J., Ko, W. J., Cerra, F. B., Hu, W. S., J Cell Biol, 1992, 116, 1043–1053.
[54] Binder, L., Frankfurter, A., Rebhun, L., J Cell Biol, 1985, 101, 914–923.
[55] Bhatia, S. N., Yarmush, M. L., Toner, M., J Biomed Mater Res, 1997, 34, 189–199.
[56] Khetani, S. R., Bhatia, S. N., Nat Biotechnol, 2008, 26, 120 – 126.
[57] Brodie, B. B., Axelrod, J., J Pharmacol Exp Ther. 1949, 97, 58-67.
[58] Jagenburg, O. R., Toczko, K., Biochem J. 1964, 92, 639-643.
[59] Buch, H., Pfleger, K., Rummel, W., Ullrich, V., Hey, D., Staudinger, H. J., Biocherm Pharmac., 1967, 16, 2247-2256.
[60] Prescott, L. F., Clinical Pharmacology & Therapeutics, 1969, 10, 383–394.
[61] Raaflaub, J., Dubach, U. C., Journal of Molecular Medicine, 1969, 47, 1286–1287.
[62] Nery, R., Biochem J., 1971, 122, 317-326.
[63] Uehleke, H., Hellmer, K. H., Tabarelli-Poplawski, S., Naunyn-Schmiedeberg's Archives of Pharmacology, 1973, 279, 39–52.
[64] Smith, R. L, Timbrell, J. A., Xenobiotica, 1974, 4, 503-508.
[65] Klutch, A., Levin, W., Chang, R. L., Vane, F., Conney, A. H., Clin Pharmacol Ther., 1978, 24, 287–293.

Chapter 3. Single-Cell Level Co-culture Platform for Intercellular Communication

Reproduced with permission from: Soongweon Hong*, Qiong Pan* & Luke P. Lee, “Single-cell level co-culture platform for intercellular communication”, Integrative Biology, 2012, 4, 374–380.

3.1 Introduction

Intercellular communication is central in determining cellular functions [1-3]. Intercellular signals enable cells to maintain homeostasis, develop into specific subtypes, respond to emergent situations, and more [Figure 3.1 A]. Understanding intercellular signaling processes is of the highest interest in cellular biology, especially in tissue engineering [4-6] cancer therapy [7-9] and stem cell regenerative medicine [5, 10-12]. Despite the recognition of its importance, cell signaling remains poorly understood due to its complexity.

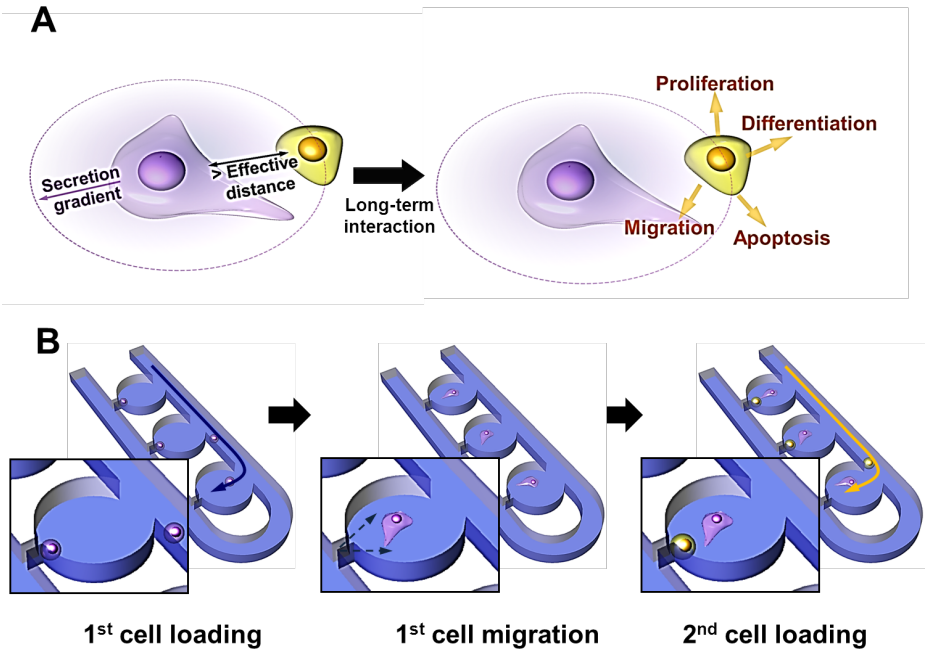

Figure 3.1 (A) Biological events in cell-cell interactions and (B) platform solution to address their one-to-one communication. Intercellular communication, based on the secretion and reception of molecular signals, influences a broad range of biological events, including proliferation, differentiation, cell death, and so on. However, the large number of cells involved in these events vastly increases the biological complexity of the system, preventing an in-depth understanding of *in vivo* cell-cell interactions.

Although conventional dish co-culture [13-17] and artificially manipulated cell patterns [18-22] have played major roles in intercellular signaling studies, these

can provide only collective [therefore, overly general] information due to mixtures of multiple, time-variable signals [23] Unraveling the molecular mechanisms underlying cell-cell communication may be eased by downsizing cell population to a single-cell level and tracking their cellular interaction for several generations. Also, in order to obtain a meaningful understanding of cellular heterogeneity [i.e. a variety of genotypic and phenotypic expression even within the same cell type], the ability to handle a large number of individual cells in a high-throughput manner is critical [24, 25].

Among previous cellular studies, microfluidic platforms have revealed advantages, such as precise controls of dynamic perfusion and physiologically relevant microenvironments [26-28], capacity to handle single cells [29-32], and high-throughput analysis under varied and repeatable conditions [33, 34]. Especially recent endeavors of using microfluidic platform enabled advanced understanding in cell-cell communication ranging in stem cells [35], immune cells [36], cancer cells [37, 38] to neurons [39] Various cellular manipulation methodologies using dynamic fluidic resistance [40-42], cellular-scale geometrical confinement [43-45], biochemical patterning [46, 47] or non-fluidic forces [48-52] have been reported. While these arising approaches have presented good examples of single cell capture and pairing, further efforts is required for efficient and flexible cell pairing, and tracking single-cell pairs for a long time period and enable cell proliferation and interaction in a physically less restrained manner.

In this respect, we have developed a single-cell level co-culture platform for intercellular interaction studies [Figure 3.1 B], which can satisfy: high efficiency in cell grouping; high-viability, long-term observation of isolated populations, and minimized physical restraints to cells for reliable observations. In this platform, we utilize self-variable fluidic resistance for high-efficiency single-cell trapping. While a cell solution is flowed through channels, single cells are directed to individual culture chambers, specifically to the small junctions [< 5 μm width] located on the bottom of chambers. Since a single cell trapped at the trapping junction changes fluidic flow, subsequent cell entry to the same chambers is prevented. After incubation time cells migrate away from the trapping junction in general, therefore reactivating the trapping junctions. Then, a second cell type is loaded to these trapping junctions by the same mechanism as before. Based on this simple successive process, a variety of cell-cell communication studies can be accomplished with various combinations of cell type. From a single operation of this microfluidic platform, the efficiency of heterotypic single-cell pairing was attained to be more than 150 cases, or about 50 % of the culture chambers. This platform's throughput not only is a higher number of cases than conventional dish co-culture [13] but is also easily expandable by increasing the number of culture chambers for a higher cell number requirement. Moreover, spacious size of culture chambers allow cell pairs to survive longer than 3~4 days without notable physical restrains for cellular proliferation.

To demonstrate the ability of this platform in facilitating understanding of cell-cell interaction, we performed single-cell level pairing of mouse embryonic fibroblasts

[MEF] and mouse embryonic stem cells (mESC). A long-term monitoring on cell pairs showed the distance-dependent migration and a dramatic change of proliferation rate compared to single-type cell cultures. These aspects of single-cell level interaction indicated biological clues of *in vivo* interaction of fibroblasts and stem cell.

3.2 Materials and Methods

Materials

All tissue culture media and the CellTracker probes were purchased from Gibco-Invitrogen Corporation (Carlsbad, CA, USA). The mouse embryonic stem cell line TNG-B was a generous gift from Prof. Ian Chambers, University of Edinburgh. Mouse embryonic fibroblasts were provided by Tissue Culture Facility, University of California Berkeley. All chemicals were purchased from Sigma–Aldrich Chemical Company, unless otherwise indicated. Mouse leukemia inhibitory factor (LIF) was purchased from Millipore Biomanufacturing and Life Science Research (Billerica, Massachusetts, USA).

Microfluidic Chip Fabrication

The fabrication of the chip follows a standard photolithography process. In brief, the negative photoresist SU8-3035 (Microchem, Newton, MA, USA) was deposited on a clean silicon wafer using a spin coater (Brewer Science Spinner, Rolla, MO, USA), resulting in a thickness of 35 μm photoresist layer. After soft baking, the wafer was exposed with the UV energy of 250 mJ/cm^2 using an OAI Hybralign Series 400 (Optical Associates, Inc., San Jose, CA, USA) mask aligner. The wafer was post-exposure baked and allowed to cool to room temperature and then developed in SU-8 Devloper (Microchem) developer. The microstructured wafer was then used as a molder of Polydimethylsiloxane (PDMS). The inlets and outlets on the PDMS chip were made using a 0.9mm gold tip puncher. The chip was permanently bonded facing down on a 25 mm× 70 mm × 1 mm (VWR International Inc., USA) microscope glass slide by exposing the PDMS and the glass to 15 seconds of Oxygen plasma with 0.12 Torr oxygen pressure and 0.28 power level (Plasmod, Tegal Corp., Novato, CA, USA).

Cell Culture

Mouse embryonic stem cells were cultured in high glucose Dulbecco's modified Eagle medium (DMEM) and F12 nutrition mix (1:1), supplemented with 10% (v/v) fetal bovine serum, 1% (v/v) penicillin, non-essential amino acid, sodium pyruvate, glutamax and 2-mercaptoethanol. To keep the pluripotent state of stem cells, the media was also supplemented with 1000 U/mL mouse leukemia inhibitory factor (LIF). Mouse embryonic fibroblast cells were maintained in high glucose DMEM supplemented with 10% (v/v) fetal bovine serum, 1% (v/v) glutamax and penicillin and streptavidin. Cells were cultured in 5% CO_2 humidified incubator at 37 °C. Cells were harvested using 0.05% (w/v) trypsin EDTA when 80% confluence was attained.

To prepare the cells for on-chip experiment, cells were first detached by trypsin incubation for 5 minutes, and then were 3x diluted with culture media to inactivate trypsin. Cell suspensions were passed through a cell strainer to yield single cells. Then the cells were counted and diluted to the required concentration for loading.

Cell Seeding on the Microfluidic Platform

After trypsinized cell solutions were diluted to the concentration of 0.2 million/ml with culture media, they were loaded into the inlets (*d1-8*) by suction applied at the outlet. Just after finishing single-cell trapping, residual cells were washed to the outlet with perfusion through a media inlet (*a1*), and then the microfluidic platform was incubated in a cell culture incubator for 4 hours. By following media perfusion, the time of 2^{nd} cell loading was determined based on cell distribution in individual culture chambers. The 2^{nd} cell loading was done in the same manner, but for a shorter loading time (< 5 min). Another 4-hour incubation in the incubator and media perfusion were followed.

Imaging

For fluorescent imaging of different cell types on chip, cells were stained with CellTracker of different colors. Mouse embryonic stem cell line TNG-B was stained with CellTracker Green with a concentration of 10 μM in DMEM for 10 minutes. Mouse embryonic fibroblast cells were stained with CellTracker Orange with a concentration of 5 μM in DMEM for 10 minutes. All cell types were washed with culture media three times after staining and were incubated for another 1hr before loading on chip. Single cell cultures and co-cultures were imaged using an inverted microscope (IX71, Olympus, Germany). The tracing of cells was documented by fluorescent microscopy (TE 2000-E, Nikon Instruments, USA).

Fluidic Simulation

Fluidic motion and particle movement were calculated using the multiphysics software, COMSOL 3.5. A unit of cell culture chamber array was 3-dimentionally modeled and applied with a negative pressure in the end of the channel. The fluid was assumed as an incompressible fluid; therefore, incompressible Navier-Stocks equations were calculated for fluidic velocity and streamline analysis. For cell movement, Khan and Richardson Force [62] was used with various particles having cellular diameter and mass.

3.3 Microfluidic Chip Design

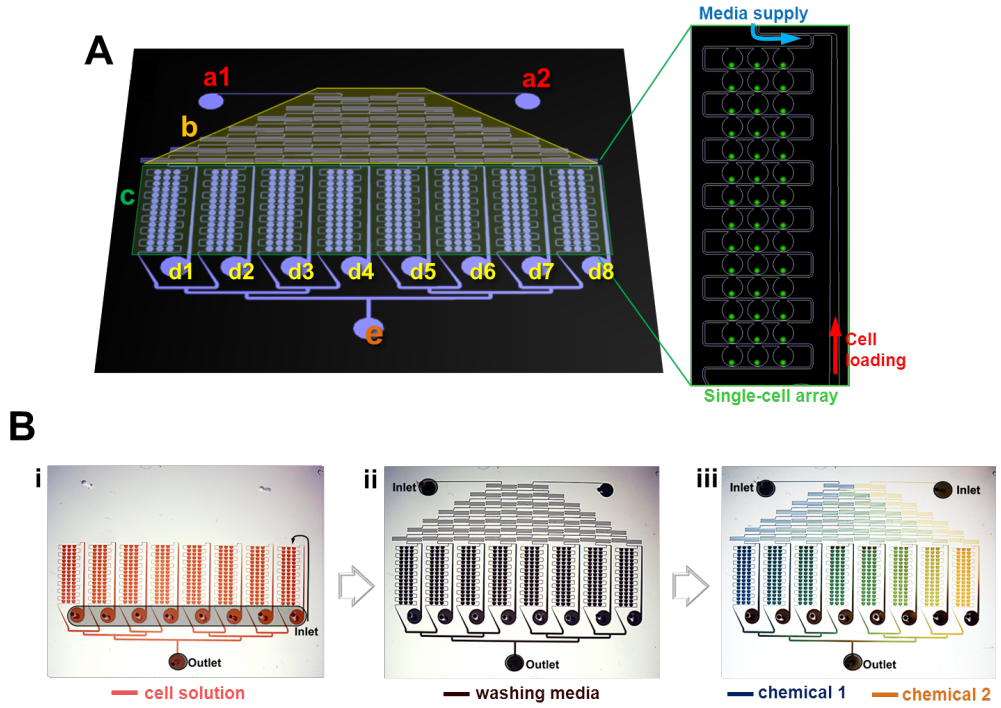

Figure 3.2 Microfluidic chip design and experimental procedures for single-cell pairing. (A) The device consists of media inlets (*a1 & a2*), a gradient generator (*b)*, culture chamber array (*c*), cell inlets (*d1 to d8*) and a waste outlet (*e*). 'C'-shaped culture chambers are designed to make semi-isolated, but media-diffusible geometries. The size of chambers is 400 μm in diameter, providing an ample space for multiple cellular divisions. The inlets and outlets are through-holes to apply external pressure or solution. Inset of A shows a single unit of trapping array linked by one wave-shaped channel. A schematic demonstration of single cells (green) trapped to the junction of each chamber. The self-variable microfluidic resistance can generate a uniform distribution of single cells. After loading, 42 cells can be trapped in each unit of the trapping array, which contains an identical chemical condition. (B) Experimental presentation with food dyes shows overall operation of the microfluidic platform from cell loading to culture. (i) For cell loading, the suspended single-cell solution is dropped on top of the 8 inlets [d1 to d8]. Negative pressure is applied to the outlet (c) in order to draw the cells into loading channels. (ii) Upon completion of cell trapping, extra cells in the chips are washed out by media flowing from one of media inlets. (iii) After 5-10 hours static incubation (depending on cell type), culture media are supplied at consistent speed through the two media inlets *a1 & a2* with a controlled negative pressure through the waste outlet. For sequential trapping of co-culture, step (i-ii) can be repeated before media supply. If necessary, the two media inlets can be applied with different chemical composition to make a linear gradient through the gradient generator.

The microfluidic chip is designed to have a large number of single-cell culture chambers, each of which is individually connected to media supply channels for continuous refreshment of its chemical environment (Figure 3.2). The chip is divided into 4 parts: a chemical gradient generator with media inlets (labeled '*a1* & a*2*' and '*b*' in Figure 3.2 A); cell loading inlets ('*d1-d8*'); cell culture chamber arrays with media-supply channels ('*c*'); and a waste outlet ('*e*'). The chip contains about 340 single-cell culture chambers. The 8 inlets (*d1-d8)* branches to

cell loading channels connected to individual arrays of culture chambers, which enable efficient cell loading procedures. The cell loading channels are gradually tapered to enhance single-cell separation along the loading channels.

For cell trapping without the use of complicated valve systems, the culture chambers have two connections with media loading channels. The upper, large opening connection is for cell entry and also diffusion-based infusion of media, while the bottom, narrow connection [or trapping junction] is for control of variable fluidic resistance before and after cell trapping. The trapping junction is optimized to be 3-μm width for stable single-cell trapping and for having less shear stress during the cell loading.

The cell culture chambers provide space enough for multiple cell divisions and a large range of migration. Also, the semi-closed environment and stable flow in the C-shaped culture chambers assure regulated diffusion between cells [therefore, regulated cell communication] with continuously refreshed media. Since the diameter of the culture chambers is 400 μm, the initial distance between paired cells can range from contact to hundreds of micrometers, as will be described later.

This fluidic chip operation is designed to minimize perturbation of fluid during cell loading, chip handling and media supply. Separation of media and cell inlets, thin PDMS strip as an inlet blocker, and withdraw-based cell and media loading are devised for this purpose. A gradient generator after the media inlets can increase flow stability into 8 units of culture chamber array and can be utilized to make chemical gradients to the units for a purpose (Figure 3.2). Cell loading procedures follows these step: (1) media is filled up with negative pressure driven flow [53], (2) 1st cell type is loaded by dropping cell solution into 8 inlets (*d1-8*) and withdrawing at outlet (*e*), (3) any residual cells not trapped in chambers or channels are washed to outlet by applying a flow at media inlet, and (4) after an incubation for 1st cell migration, 2nd cell type is loaded into chambers in the same way, and (5) after another incubation for 2nd cell adhesion, the cell inlets (*d1-8*) are blocked with a thin PDMS strip and media perfusion starts by applying a withdraw at the outlet (e). Each operation flow rate was determined not to cause shear stress of phenotype change by simulation.

3.4 Single-cell Proliferation on Chip

Sufficient nutrients and enough space need to be provided to observe a long-term cell interaction. Here, a manner of continuous media supplement is adopted for a refreshed nutritional environment. The culture chambers were also designed and optimized to meet the long-term culture criterion. On the other hand, fluidic shear stress on cells should be minimized to give reliable information on cell behavior. Through simulation and experimental verification, we have demonstrated the ability of this device for delicate cell culture and analysis without hammering their viability.

In order to establish comparable cell proliferation patterns, mammalian cell types were cultured and monitored for their proliferation. Under optimized culture

conditions, we cultured several cell types (including MEFs and mESCs), and observed multiple successive divisions over a period of at least 3 days (Appendix D). For MEF, their single-cell viability was high enough to show multiple generations from the majority of trapped cells (>95% among single-cell trapping), and the proliferation rate of both single and multiple cells was similar to dish culture results (20~25 hrs). On the other hand, mESCs did not show a clear viability as a single cell under MEF culture media supplement, as claimed before [54, 55], but only the stem cells that initially aggregated during the loading could proliferate at similar rates as dish culture's. Without further optimization of single-stem-cell culture (i.e. addition of growth factors), mESCs increased their viability in the presence of MEF in the same chambers, as will be discussed later.

3.5 Sequential Trapping Mechanism

To achieve a single-cell level co-culture with simple operation, we utilized self-variable fluidic resistance. Along the wave-shaped channels, single cells are captured into culture chambers at each trapping junction due to its variable fluidic resistance. Once the trapping junction is occupied with a cell, the fluidic resistance through the junction increases and subsequent cells are directed to other culture chambers. After the first trapped cell gets flattened and migrates from the physically restraining junction [56], the trapping junctions become open (or '*active*') and then next cell loading is accomplished by the same mechanism (Figure 3.3 A).

To optimize fluidic operation of cell loading in terms of shear stress and particle [cell] movement, a set of microfluidic simulations was executed. As an optimal case shown in Fig 3B, about 30% of flow in the loading channel is directed to the *active* trapping junction in the designed configuration, which can drive a single cell (10-μm diameter and 30-ng weight) to the junction under the flow rate of 0.125 μl/min. A cell positioned in the middle of the culture chamber after its migration undergoes shear stresses of less than 0.1 dyn/cm^2 during the 5 min of the second cell loading, which is below the shear stress previously demonstrated to induce phenotype change [57].

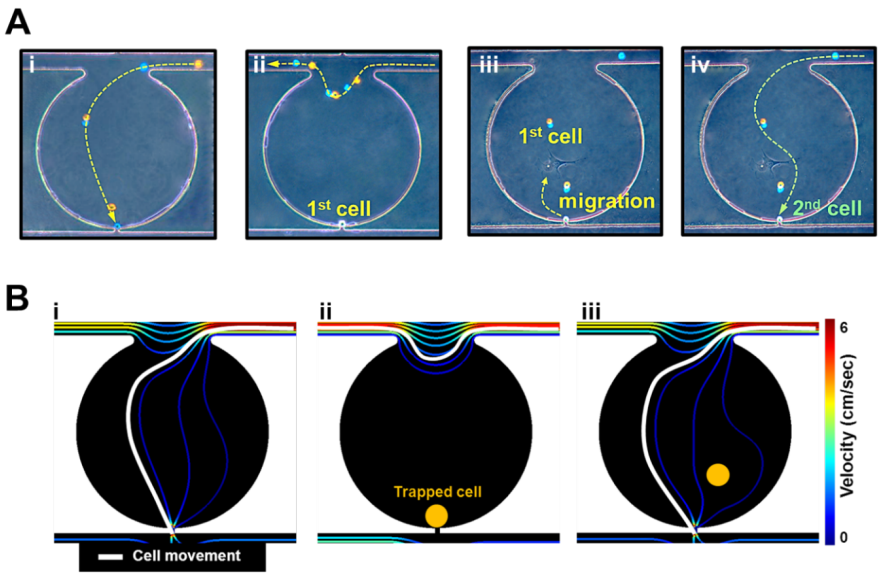

Figure 3.3 Mechanism of single-cell pairing. (A) Time-lapse images of single-cell pairing shows that [i] the first cell is trapped as a single cell at the trapping junction position in the bottom of culture chamber; [ii] following cells pass by the filled chamber due to self-variable fluidic resistance; [iii] the trapped cell migrates away from the trapping junction toward the middle of chamber; and [iv] another cell loading is enabled in the same chamber due to the reactivated trapping. (B) Fluidic calculation through a simulation was used to find the optimal design of the microfluidic chip. [i] In the optimized design, about 30% of the flow goes through the trapping junction when the junction is not occupied with cell. Under a flow rate of 0.125 μl/min along the wave-shaped channel, cells can be directed toward chambers by following a streamline instead of the inertial direction. [ii] After a single cell is trapped at the junction, almost all the flow goes through the wave-shaped channel, preventing multiple cell trapping. [iii] Since the first cell migrates and opens the trapping junction to activate it, loading of the second cell is possible. During the second loading, cells positioned in the middle of chambers are exposed to negligible fluidic shear stress due to the large size of the culture chamber. Based on simulation calculations, the shear stress on a cell of 10-μm diameter can be less than 0.1dyn/cm^2, which should not cause phenotype change.

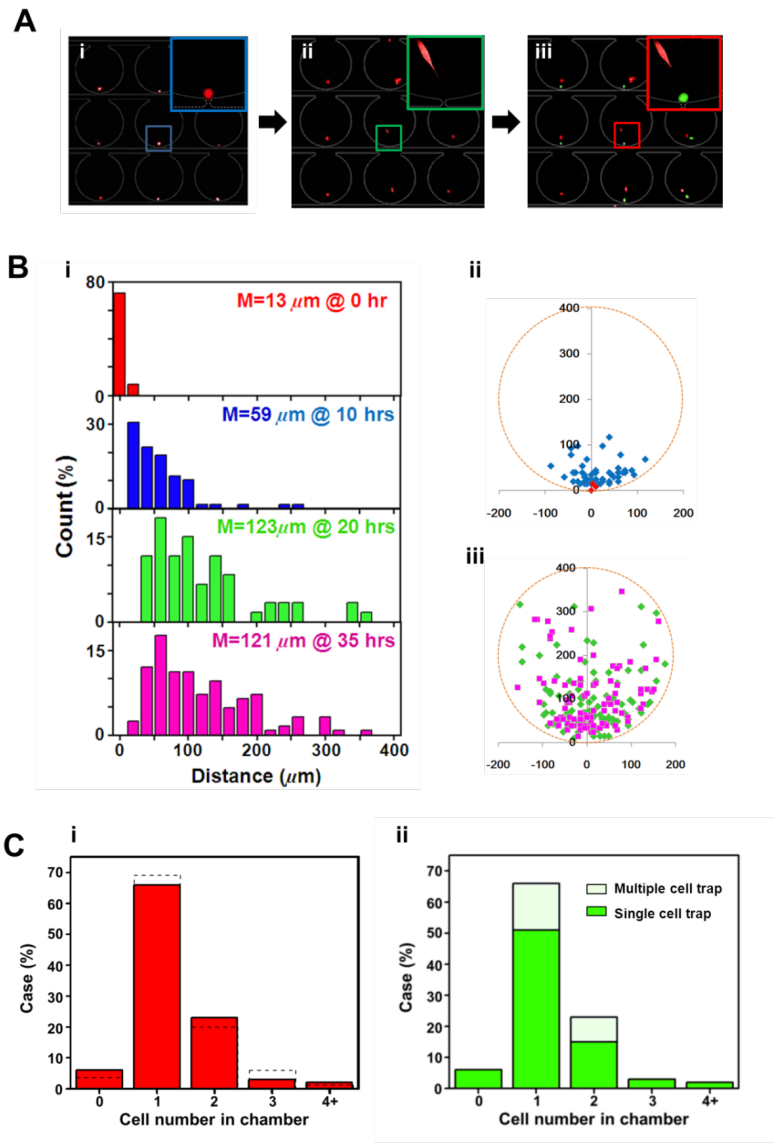

Figure 3.4 Sequential trapping of MEF and mESC. (A) Fluorescence images of first cell trapping, migration, and second cell trapping. High efficient single-cell pairing in the C-shaped chambers was achieved. MEF is stained with CellTracker Orange, and mESC is stained with CellTracker Green. i, MEFs are trapped at the junction gaps as single-cells. ii, after 10 hours static incubation, MEFs migrated away from the junction gaps. iii, mESCs were trapped to the junction gaps as single-cells in the same mechanism. (B) The trapped cells [here MEFs] migrated away from the trapping gaps during incubation time. For single-cell trapping cases, histogram of migration distance from the trapping gap and spatial distribution in the culture chamber are shown in four time points: 0, 10, 20, 35 hours. After 10-hour static culture, 0.02-μl/min flow of MEF culture media was applied. (C) High efficiency of single-cell pairing of MEF and mESC after the sequential trapping. i, the first loading of MEF resulted in a large number of single-cell case (about 70% of total chambers). Even after 10-hour incubation, most of MEFs trapped as a single cell remained in the same culture chambers due to geometric confinement of culture chamber (~65%). ii, the second loading of mESC also resulted in a similar rate (70%) of single cell loading to single-cell MEF chambers, therefore about 50% (70% × 70%) of total chambers being single-cell pairs.

Cell migration is an essential mechanism of trapping junction reactivation in this platform. Also, the distance between cells in the culture chambers is determined by cell migration, which can influence the extent of intercellular communication (Figure 3.4 A). The incubation time between the first and second cell loading can be assumed to determine the cellular migration amount.

To assess migration behavior of fibroblasts in the context of MEF-mESC pairing, we observed the migration of MEFs in both the first 10-hour static incubation and successive 40-hour perfusion culture. During the 10-hour static incubation, MEF attached to the surface, became flattened and migrated away from the junction. The migration distance was relatively small, at about 60 μm on average (Figure 3.4 B). When perfusion began, fibroblasts migrated further but were prevented from escaping by the chamber's geometric design. After incubation for 20 hours, the MEFs showed a wide distribution and random positioning within the chambers, which generates various cases of cell-to-cell distances after the second loading.

Different cell mass to volume ratio and surface adhesion capabilities correspond with different optimal fluidic operation (i.e. flow rate, cell density and loading period). In the case of MEF loading, a 1 μl/min flow rate for 5 minutes was applied by withdrawing at the waste outlet, and for the second loading of mESCs, a 0.8 μl/min flow rate for 3 minutes was applied. In this condition, 70% efficient single MEF trapping and 70% single-cell pairing among the single-cell trapped MEFs (therefore about 50% chambers being single-cell pairing, which is about 150 cases) was repeatedly achieved (Figure 3.4 C). Although this pairing efficiency was limited mainly due to cell aggregation, cellular debris, and cell size variation, which are difficult to avoid during cell preparation, the pairing case number in this chip can be enough to provide a level of statistical data for the single-cell communication study. Moreover, the other pairing cases (i.e. multiple-to-single and multiple-to-multiple), although not discussed here, would be able to provide information regarding other interesting aspects of cellular communication.

3.6 Interactions between Embryonic Fibroblast and Stem Cell

Fibroblasts are known to secrete essential materials for the proliferation of nearby cells. Especially in stem cell research, they are often used as a feeder layer for stem cell culture and maintenance of pluripotency. Under conventional culture conditions, several fibroblast-secreted factors, such as basic fibroblast growth factor (bFGF), vascular endothelial growth factor (VEGF), Leukemia inhibitory factor (LIF) and more have been shown to have positive effects on embryonic stem cell survival, growth, and migration [58-60]. On the other hand, previous studies suggest clues for stem cell induction on fibroblast proliferation, migration, and gene expression through paracrine secretions These studies indicated the possible responsiveness between fibroblast and stem cell. The paired MEF and mESC on the chip can provide more statistical evidences of their interaction for future study.

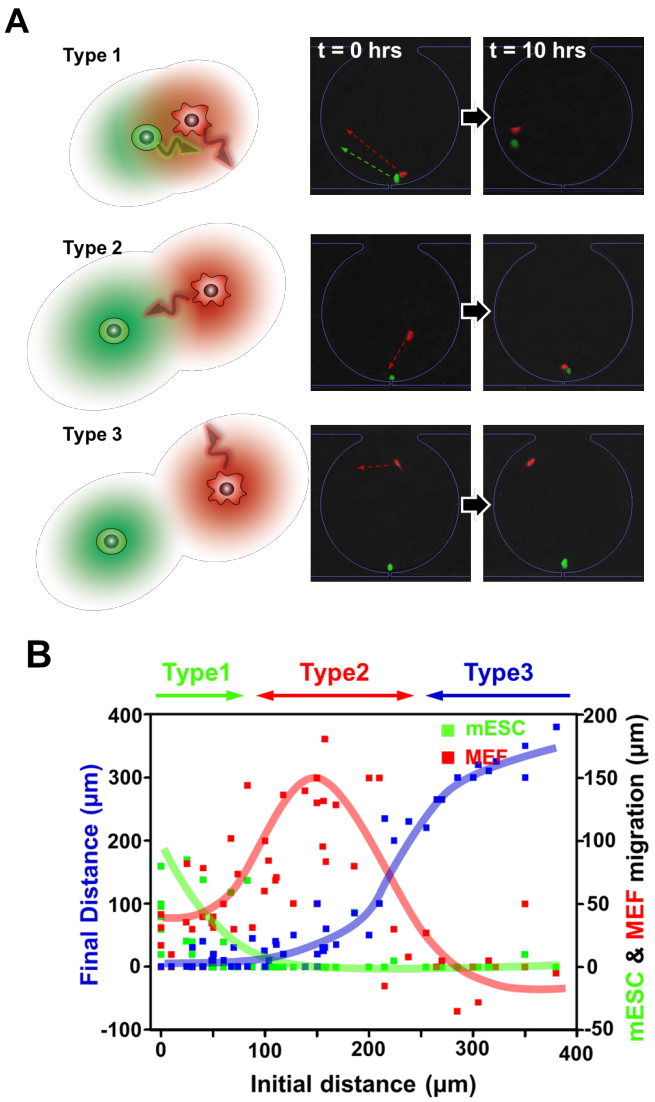

Figure 3.5 Migration behavior dependence to intercellular distance between MEF and mESC. (A) Correlated migration of MEF and mESC was observed when the initial distance was close (Type 1). If the distance is intermediate, MEF approached mESC which did not show any clear migration (Type 2). If the distance was far, MEF migration showed random migrations regardless of mESC position (Type 3). Fluorescence images show cell positions after trapping and 10-hour incubation. (B) Statistical data showed that degree of interaction can be distinguished based on the initial distance, the variety of which was created from random migration of MEF after MEF loading. We have collected 90 data points for this migration characterization from 3 independent experiments. For minimized photo-toxicity during fluorescence imaging, we only observed ~30 cases in each experiment. MEF migration (red points) and mESC migration (green points) is the relevant migration distance toward paired mESC.and MEF, respectively. The final distance is the distance between MEF and mESC after 10 hours of co-culture.

From single-cell pairs of MEF and mESC in the chip, we were able to observe two distinctive cellular behaviors in migration and proliferation. After pairing, all

cells were cultured under continuous media supply in the absence of LIF for at least 3 days, and observed on an inverted microscope over a 3- to 6-hour period. Within the first 10 hours after pairing, the migration shows a dependence on initial distance. Based on the relative movement of mESC to MEF, the mESCs that started close to MEFs (initial distance, ID < 80 μm) showed enhanced migration along with MEF movement, while the mESCs that started far from MEFs (ID >80 μm), showed relatively little or no movement that relates to MEF. MEFs, on the other hand, proclivity migrate toward mESCs within a range of distance (ID < 230 μm), based on the increased relative movement in the middle range of Fig 6B. But moved randomly regardless of mESCs when its distance is too far for intercellular communication (ID > 230 μm) (Figure 3.5).

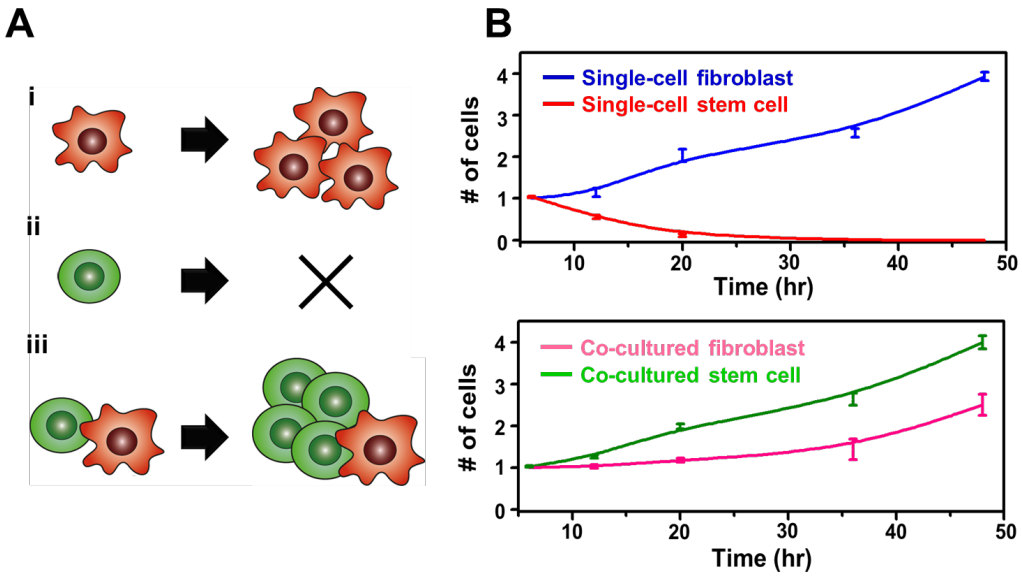

Figure 3.6 Distinctive proliferation difference between co-culture and homotypic culture. The average cell numbers in culture chambers were calculated from 89 cases of single-cell pairing. mESC cultured alone did not show a high viability (<5%), whereas co-culture with fibroblast in the same chamber increased mESC viability and demonstrated a similar doubling time to that found in dish culture. On the other hand, MEF, as a single cell, proliferated at a similar rate to dish culture, but co-cultured MEF showed a decreased proliferation rate, possibly due to nutrient competition with the stem cell.

Another interesting behavior from this single-cell co-culture was the change of proliferation rate (Figure 3.6). The feeder layer role of MEFs for embryonic stem cells is known to enhance stem cell proliferation. Single mESC cultured individually suffered from low viability and cell death due to lack of autocrine signaling from neighboring cells which are important for its survival. Co-culture of mESCs single cell with MEFs noticeably enhanced the stem cell viability and restored a proliferation rate comparable to dish culture (~20 hours) [61], which indicates the role of MEF secretion to supplement the autocrine signaling for mESCs growth from single cells. This enhanced proliferation rate was not clearly dependent on the initial distance between the pairs, which is understandable as enough diffusion of secretion molecule in the chambers in the time scale of proliferation (~10hrs). In contrast, MEFs showed a proliferation rate comparable

to dish culture when cultured without mESCs, while mESC-paired MEFs slowed their proliferation rate from 20 hours to more than 40 hours. The decreased proliferation rate of MEFs may be due to the nutrient competition with highly proliferative stem cells.

3.7 Conclusions

A broad range of *in vivo* events is influenced by cellular communication. These consist of various combinations of biomolecules and cell types, increasing the difficulty in understanding them. Herein, we have presented a high-throughput microfluidic platform for single-cell level co-culture. This platform provides a simplified solution to understand intercellular communication by minimizing the number of cells involved and maintaining controlled molecular diffusion patterns under continuous microfluidic perfusion. By providing all cells with a biochemically-defined environment with sufficient nutrient supply and space for proliferation and migration, this microfluidic co-culture platform can simply and quantitatively monitor decoded information behind complex intercellular interaction. As an example study, the co-culture of MEF and mESC in this platform demonstrated two distinctive behaviors: enhanced migration and varied proliferation compared to homotypic culture. This single-cell level co-culture platform will enhance our understanding of various biological events by providing researchers with well-controlled simplified physiologically relevant microenvironments in a dynamic perfusion way for the study of cell-cell communication and interactions.

References

[1] Alberts, B., Essential cell biology 3rd ed., Garland Science, New York, 2009.
[2] Trosko, J. E., Ruch, R. J., Front Biosci, 1998, 3, d208-d236.
[3] Waters, C. M., Bassler, B. L., Annu Rev Cell Dev Bio, 2005, 21, 319-346.
[4] Delcarpio, J. B., Claycomb, W. C., Ann Ny Acad Sci, 1995, 752, 267-285.
[5] Khademhosseini, A., Langer, R., Borenstein, J., Vacanti, J. P., Proc Natl Acad Sci U S A, 2006, 103, 2480-2487.
[6] Bhatia, S. N., Balis, U. J., Yarmush, M. L., Toner, M., FASEB J, 1999, 13, 1883-1900.
[7] Wendel, H. G., Stanchina, E. D., Fridman, J. S., Malina, A., Ray, S., Kogan, S., Cordon-Cardo, C., Pelletier, J., Lowe, S. W., Nature, 2004, 428, 332-337.
[8] Adjei, A. A., J Natl Cancer Inst, 2001, 93, 1062-1074.
[9] Hanahan, D., Weinberg, R. A., Cell, 2000, 100, 57-70.
[10] Behfar, A., Zingman, L. V., Hodgson, D. M., Rauzier, J. M., Kane, G. C., Terzic, A., Puceat, M., FASEB J, 2002, 16, 1558-1566.
[11] Xu, Y., Shi, Y., Ding, S., Nature, 2008, 453, 338-344.
[12] Nishikawa, S., Goldstein, R. A., Nierras, C. R., Nat Rev Mol Cell Biol, 2008, 9, 725-729.
[13] Burguera, E. F., Bitar, M., Bruinink, A., Eur Cell Mater, 2010, 19, 166-179.
[14] Smith, A. N., Willis, E., Chan, V. T., Muffley, L. A., Isik, F. F., Gibran, N. S., Hocking, A. M., Exp Cell Res, 2010, 316, 48-54.

[15] Holt, D. J., Chamberlain, L. M., Grainger, D. W., Biomaterials, 2010, 31, 9382-9394.
[16] Karnoub, A. E., Dash, A. B., Vo, A. P., Sullivan, A., Brooks, M. W., Bell, G. W., Richardson, A. L., Polyak, K., Tubo, R., Weinberg, R. A., Nature, 2007, 449, 557-564.
[17] Arnold, J. T., Kaufman, D. G., Seppala, M., Lessey, B. A., Hum Reprod, 2001, 16, 836-845.
[18] Folch, A., Toner, M., Annual Review of Biomedical Engineering, 2000, 2, 227.
[19] Bhatia, S. N., Yarmush, M. L., Toner, M., J Biomed Mater Res, 1997, 34, 189-199.
[20] Yousaf, M. N., Houseman, B. T., Mrksich, M., P Natl Acad Sci USA, 2001, 98, 5992-5996.
[21] Fukuda, J., Khademhosseini, A., Yeh, J., Eng, G., Cheng, J. J., Farokhzad, O. C., Langer, R., Biomaterials, 2006, 27, 1479-1486.
[22] Chung, S., Sudo, R., Mack, P. J., Wan, C. R., Vickerman, V., Kamm, R. D., Lab Chip, 2009, 9, 269-275.
[23] Breslauer, D. N., Lee, P. J., Lee, L. P., Mol Biosyst, 2006, 2, 97-112.
[24] Wang, D. J., Bodovitz, S., Trends Biotechnol, 2010, 28, 281-290.
[25] Arriaga, P. D. D. A. E. A., Single Cell Analysis: Technologies and Applications. Wiley-VCH Verlag GmbH & Co. KGaA: Weinheim, Germany, 2009.
[26] Lee, P. J., Hung, P. J., Lee, L. P., Biotechnol Bioeng, 2007, 97, 1340-1346.
[27] Hung, P. J., Lee, P. J., Sabounchi, P., Lin, R., Lee, L. P., Biotechnol Bioeng, 2005, 89, 1-8.
[28] Hung, P. J., Lee, P. J., Sabounchi, P., Aghdam, N., Lin, R., Lee, L. P., Lab Chip, 2005, 5, 44-48.
[29] Chronis, N., Lee, L. P., IEEE MEMS, 2004, 17-20.
[30] Di Carlo, D., Wu, L. Y., Lee, L. P., Lab Chip 2006, 6, 1445-1449.
[31] Khine, M., Lau, A., Ionescu-Zanetti, C., Seo, J., Lee, L. P., Lab Chip, 2005, 5, 38-43.
[32] Di Carlo, D., Lee, L. P., Anal Chem, 2006, 78, 7918-7925.
[33] Young, E. W., Beebe, D. J., Chem Soc Rev, 2010, 39, 1036-1048.
[34] Zare, R. N., Kim, S., Annu Rev Biomed Eng, 2010, 12, 187-201.
[35] Parekkadan, B., Berdichevsky, Y., Irimia, D., Leeder, A., Yarmush, G., Toner, M., Levine, J. B., Yarmush, M. L., Neurosci Lett, 2008, 438, 190-195.
[36] Varadarajan, N., Julg, B., Yamanaka, Y. J., Chen, H., Ogunniyi, A. O., McAndrew, E., Porter, L. C., Piechocka-Trocha, A., Hill, B. J., Douek, D. C., Pereyra, F., Walker, B. D., Love, J. C., J Clin Invest, 2011, 121, 4322-4331.
[37] Yin, Z. Z., Noren, D., Wang, C. J., Hang, R., Levchenko, A., Mol Syst Biol, 2008, 4.
[38] Frimat, J. P., Becker, M., Chiang, Y. Y., Marggraf, U., Janasek, D., Hengstler, J. G., Franzke, J., West, J., Lab Chip, 2011, 11, 231-237.
[39] Pirlo, R. K., Sweeney, A. J., Ringeisen, B. R., Kindy, M., Gao, B. Z., Biomicrofluidics, 2011, 5.

[40] Wheeler, A. R., Throndset, W. R., Whelan, R. J., Leach, A. M., Zare, R. N., Liao, Y. H., Farrell, K., Manger, I. D., Daridon, A., Anal Chem, 2003, 75, 3581-3586.
[41] Di Carlo, D., Wu, L. Y., Lee, L. P., Lab Chip, 2006, 6, 1445-1449.
[42] Tan, W. H., Takeuchi, S., Proc Natl Acad Sci U S A, 2007, 104, 1146-1151.
[43] You, A. J., Jackman, R. J., Whitesides, G. M., Schreiber, S. L., Chem Biol, 1997, 4, 969-975.
[44] Chin, V. I., Taupin, P., Sanga, S., Scheel, J., Gage, F. H., Bhatia, S. N., Biotechnol Bioeng, 2004, 88, 399-415.
[45] Love, J. C., Ronan, J. L., Grotenbreg, G. M., van der Veen, A. G., Ploegh, H. L., Nat Biotechnol, 2006, 24, 703-707.
[46] Hoover, D. K., Chan, E. W., Yousaf, M. N., J Am Chem Soc, 2008, 130, 3280-3281.
[47] Azioune, A., Storch, M., Bornens, M., Thery, M., Piel, M., Lab Chip, 2009, 9, 1640-1642.
[48] Ozkan, M., Wang, M., Ozkan, C., Flynn, R., Birkbeck, A., Esener, S., Biomed Microdevices, 2003, 5, 61-67.
[49] Ino, K., Okochi, M., Konishi, N., Nakatochi, M., Imai, R., Shikida, M., Ito, A., Honda, H., Lab Chip, 2008, 8, 134-142.
[50] Taff, B. M., Voldman, J., Anal Chem, 2005, 77, 7976-7983.
[51] Mittal, N., Rosenthal, A., Voldman, J., Lab Chip, 2007, 7, 1146-1153.
[52] Chiou, P. Y., Ohta, A. T., Wu, M. C., Nature, 2005, 436, 370-372.
[53] Hosokawa, K., Sato, K., Ichikawa, N., Maeda, M., Lab Chip, 2004, 4, 181-185.
[54] Khoury, M., Bransky, A., Korin, N., Konak, L. C., Enikolopov, G., Tzchori, I., Levenberg, S., Biomed Microdevices, 2010, 12, 1001-1008.
[55] Kim, L., Vahey, M. D., Lee, H. Y., Voldman, J., Lab Chip, 2006, 6, 394-406.
[56] Jiang, X., Bruzewicz, D. A., Wong, A. P., Piel, M., Whitesides, G. M., Proc Natl Acad Sci U S A, 2005, 102, 975-978.
[57] Toh, Y. C., Voldman, J., FASEB J, 2011, 25, 1208-1217.
[58] Eiselleova, L., Matulka, K., Kriz, V., Kunova, M., Schmidtova, Z., Neradil, J., Tichy, B., Dvorakova, D., Pospisilova, S., Hampl, A., Dvorak, P., Stem Cells, 2009, 27, 1847-1857.
[59] Brusselmans, K., Bono, F., Collen, D., Herbert, J. M., Carmeliet, P., Dewerchin, M., J Biol Chem, 2005, 280, 3493-3499.
[60] Gotoh, N., Curr Stem Cell Res Ther, 2009, 4, 9-15.
[61] Kapur, N., Mignery, G. A., Banach, K., Am J Physiol Cell Physiol, 2007, 292, C1510-c1518.

Chapter 4. Isothermal Single-cell miRNA Quantification Reveals Heterogeneous miRNA Regulation of Cancer Cells

4.1 Introduction

MicroRNAs (miRNAs) are a class of 17–25 nucleotides non-coding RNAs that have been shown to have critical functions in a wide variety of biological processes during development including cell cycle regulation, apoptosis, cell differentiation, maintenance of stemness and imprinting [1, 2]. Therefore, it is not surprising that miRNAs have already been know to associate with a number of diseases such as cancer [3–9], neurological diseases [10], viral diseases [11] and metabolic diseases [12]. In general, microRNAs function as post-transcriptional regulators of gene expression by either triggering mRNA cleavage or repressing translation [13]. Traditional gene expression experiments characterize averages of thousands to millions of cells from a particular tissue or cultured cell population. However, considering recent reports on the impact of cell-to-cell fluctuations in gene expression on phenotypic diversity, it is likely that looking at the average miRNA expression of cell populations could result in the loss of important information connecting miRNA expression and cell function. To investigate in a homogeneous cell population, it is necessary to apply sensitive and specific single cell isolation and analysis methods.

The very small size of miRNA has made it difficult to detect specifically and sensitively using standard molecular biological methods. Recently developed bead-based flow cytometric miRNA expression profiling method provides accurate and sensitive information of microRNA expression [14]. However, it requires isolation of total RNAs and the removal of genomic DNA, followed by recovery of small RNA fragments from this sample. Therefore, although the sensitivity of the method is high and requires only 5 ng of material, it is not amenable for analysis of single cells. Another method by Chen *et al*. [15] used a looped real-time PCR-based technique to detect expression of miRNAs. With this approach they can cover at least 7 log of expression range that is accurate and specific for mature miRNA. This method needs sequence specific reverse and forward primers and a probe, the amplification is performed after a separated RT process, a preferred pre-PCR step and a PCR amplification, which is not suitable for fast and high throughput process of single cells and automated cell-to-signal generation. Beckman Coulter has developed a tube-based kit for absolute quantification of microRNA copy number in single cells, involving multiple steps including desiccation of cells, first-strand cDNA synthesis and real time PCR, which is performed in separate reaction vials with manually transferred cDNA products. In-situ hybridization based miRNA quantification was also developed

[16], but it requires very delicate operations and a long time of procedure. However, there is still limitation to the throughput of analysis, and the methods usually required manual operation, micromanipulation and intensive human power.

Microwell based single-cell capture and cell content analysis has been the choice of many single-cell studies due to its ability to parallel analyze massive amount of single-cells and its ease of operation. The operation usually involves a single-cell capture step; a cell lyses step and a RNA amplification step with RT-PCR. In practice, real time signal monitoring is not as applicable with microwell array based single-cell detection as end-point signal measurement. End-point PCR has linear range and sensitivity limitations due to the usually observed signal saturation after certain cycles of amplification. The exponential range of a PCR ceases at the point when the product competes with primer binding severely. With the common concentration of primers of 150-300nM, at cycle number 10-15, the amount of product will be the same as the concentration of primers. The product renaturation will be very competitive to primer binding. At that point, the signal is only 6 orders amplified. For the sake of accuracy and precision, it is necessary to collect quantitative data at a point in which every sample is in the exponential phase of amplification (since it is only in this phase that amplification is extremely reproducible). Analysis of reactions during exponential phase at a given cycle number should theoretically provide several orders of magnitude of dynamic range. Rare targets will probably be below the limit of detection, while abundant targets will be past the exponential phase. In practice, a dynamic range of 2-3 logs can be quantitated during end-point relative RT-PCR. For targets that are beyond this range, dilution replicates may be needed for the specific target so that all of the samples can be analyzed in the exponential phase. However, in microwell based single-cell gene amplification, we expect the end-point detection to be accurate across the wide range of target concentration among single-cells. In the case of miRNA, the copy numbers of a miRNA can vary across 5-6 orders of magnitude among a population of single-cells. It is not accurate to quantify miRNA signal with end-point PCR.

Therefore, we have developed an N^2 amplification methodology for miRNA that can provide end-point signal that is linear to miRNA copy number over a wider dynamic range. In this method, the signal product does not participate in recycling amplification, thus has no/ minimum effect on competing with the main reaction. Although as the intermediate product becomes more as first cycling goes, there will be more demand of the second primers, and the reaction may be slowed down due to lack of primers. This problem could be easily solved by using higher concentration of primers, since primer could be easily designed to have the minimum primer-dimer binding. This reaction is proved to maintain quadratic amplification for extended time accomplishing high end-signals. Using this end signal detection scheme combining massive single-cell array, we can perform thousands of single-cell miRNA quantification within 1 hour operation and simple instrumentation. Table 1 shows the comparison with several other competing methods for single-cell miRNA detection (Tube-based PreAmp™ [17], AmpliGrid™ RT-PCR [18], Fluidigm™ RT-PCR [19]). For example, Multiplex

PreAmp TaqMan® microRNA assays from life technology uses 3 steps of multiplex RT, pre-amplification, and single-plex TaqMan PCR for single cell miRNA detection. The real-time PCR was performed on a sequence detection system and data analysis was done by averaging Ct of miRNA amplifications. The methods are compared according to their throughput, instrumentation, automation, amplification method, cost and ability of multiplexing. It can be seen that this new platform combined the benefit of high throughput from microwell array and the unique amplification method that does not require thermo-cycling and produce linear end-signal.

Tumor-associated, differentially expressed miRNAs have been found in many different cancers. Cancer-associated microRNAs show promise in both diagnostic and therapeutic applications. To demonstrate the use of this method, we quantified miRNA distributions of human breast cancer cell line MCF-7 and compared with that of the doxorubicin-resistant population. Several miRNAs showed distribution pattern and/or sub-population changes upon drug treatment, which is not shown in ensemble averages.

	Tube-based PreAmp™	AmpliGrid™ RT-PCR	Fluidigm™ RT-PCR	Our method (N^2 Amp.)
Number of cells/ device	1	48	96	>5000
Real-time data acquisition	Yes	Yes	Yes	No
Thermocycler	Yes	Yes	Yes	No
Fluorescent microscope	No	No	No	Yes
Amplification	RT-qPCR	RT-qPCR	RT-qPCR	n^2 Amp
Quantification method	Ct value	Ct value	Ct value	Snapshot value
Time required	4 hours	~ 2 hours	13 hours	1 hour
Cost	1.3 dollar/reaction	N/A	5.2 dollar/ reaction	0.6 cent/ reaction
miRNAs/ device	96	1	12	1

Table 4.1 Technique comparison of single-cell miRNA detection methods.

4.2 Materials and Methods

Microwell device fabrication

The microwell feature heights and diameters were 35 and 50 μm throughout the experiments. An SU-8 mold with micropillar structures was fabricated through standard photolithography. Briefly, the negative photoresist SU8-3035 (Microchem, Newton, MA, USA) was deposited on a clean silicon wafer using a spin coater (Brewer Science Spinner, Rolla, MO, USA), resulting in a thickness of 35 mm photoresist layer. After soft baking, the wafer was exposed with the UV energy of 250 mJ cm^{-2} using an OAI Hybralign Series 400 (Optical Associates,

Inc., San Jose, CA, USA) mask aligner. The wafer was post-exposure baked and allowed to cool to room temperature and then developed in SU-8 Developer (Microchem) developer. The microstructured wafer was then used as a mold of Polydimethylsiloxane (PDMS). To make the PDMS device, PDMS precursor was added on top of the silicon wafer, and the wafer was spinned at a speed of 500 rpm to create an even layer of thin (200 μm thickness) PDMS on top. The wafer was then placed in a 65 ^{o}C incubator to cure the PDMS for 30 mins. Afterwards, the PDMS sheet was peeled off from the wafer and cut into adequate sizes. The sheet was then placed on top of a clean glass slide with microwells facing up.

miRNA amplification method

RNase inhibitor and DEPC-treated water were obtained from Tiangen Biotechnology Co. Ltd. (Beijing, China; DEPC=diethylpyrocarbonate). Vent (exo^{-}) DNA polymerase and the nicking endonuclease Nt.BstNBI were purchased from New England Biolabs. SYBR Green I (20 x stock solution in dimethyl sulfoxide, 20 mg /mL) was purchased from Xiamen Bio-Vision Biotechnology (Xiamen, China). All solutions for the reaction were prepared in DEPC-treated deionized water. The reaction mixtures were prepared separately on ice as part A and part B. Part A consisted of Nt.BstNBI buffer, the amplification template, dNTPs, RNase inhibitor, and the miRNA target; part B consisted of ThermoPol buffer, the nicking endonuclease Nt.BstNBI, Vent (exo-) DNA polymerase, SYBR Green I, and DEPC-treated water [20]. Parts A and B were mixed immediately before loading onto the single-cell device or in tube. The reagent concentrations were: amplification template (0.1 mM), dNTPs (250 mM), Nt.BstNBI (0.4 U /mL), Vent (exo^{-}) DNA polymerase (0.05 U/ mL), RNase inhibitor (0.8 U /mL), SYBR Green I (0.4 mg /mL), 1 x ThermoPol buffer (20 mm Tris–HCl, pH 8.8, 10 mm KCl, 10 mm $(NH_4)_2SO_4$, 2 mm $MgSO_4$, 0.1% Triton X-100; Tris=2-amino-2-hydroxymethylpropane-1,3-diol), and 0.5x Nt.BstNBI buffer (25 mm Tris–HCl, pH 7.9, 50 mm NaCl, 5 mm $MgCl_2$, 0.5 mm dithiothreitol). The amplification was performed at 55 ^{o}C, and the real-time fluorescence intensity was monitored at intervals of 2 s.

Device operation and data acquisition

The purified miRNAs were purchased from Tiangen Biotechnology Co. Ltd, and were diluted with RNase-free water to a series of final concentrations. For single-cell experiments, cultured cells in flask were lifted off by trypsin incubation. Then the cell solution was centrifuged to remove trypsin and re-suspended in ice cold PBS to result a final concentration of 5.0 x 10^6 cells/mL. Then 200 μL cell solution was pipetted onto PDMS microwell slide and sit for 5-10 mins for single cells to gravity-settle into microwells. This was followed by three times of washing by PBS to remove excess cells off the surface. Then the slide was subjected to cell lyses and miRNA amplification.

The sides of PDMS microwell area were modified with strips of plastic spacer attached to the top of the glass slide. After cell loading and washing, a piece of cover slip was attached on top and secured by the plastic spacer. There is a thin layer of liquid in between the cover slip and top surface of PDMS. Reagents can

be loaded through capillary force onto the PDMS surface. To lyse the captured single-cells, lyses buffer was rapidly flowed through on top of PDMS surface, lyses and protein digestion was initiated by placing the device in a 37 ^{o}C incubator. Proteinase K is activated and cell membranes, as well as DNA/RNA-protein complexes are broken down. Proteinase K can also prohibit RNase to protect miRNA. After cell lyses, the target miRNAs are captured onto the magnetic microbeads. The debris and leftover reagents are washed out by washing buffer, while microbeads are pulled down by a magnet at the bottom of the device. After washing, miRNA amplification reagents are loaded, followed by mineral oil loading. The mineral oil replaces the liquid on top of PDMS, while creates reagent-filled microwell chambers for amplification. Afterwards, the device was placed in a 55 ^{o}C incubator for amplification.

Cell culture growth conditions

The MCF7 cell line were maintained as an attached monolayer culture in the commercially defined RPMI 1640 medium (HyClone, USA), supplemented with 10% (v/v) heat-inactivated fetal bovine serum (FBS) (HyClone, USA), 2 mM l-glutamine, 100 U/mL and 100 µg/mL penicillin–streptomycin (HyClone, USA). The cells were grown on either 25 or 75 cm^2 attached types, filter-cap culture flasks (NunClon, Denmark). The cells were then incubated at 37 °C in a 90% humidified atmosphere of 5% CO_2. Doxorubicin 2 mg/mL (Ebewe, Austria) was used to induce resistance in the MCF7 cells. To resistant cells were selected by stepwise selection method; initially the cells were grown in a cell culture media containing a doxorubicin concentration of 10 nM. When the cells were capable of growing and reaching appropriate confluency at a certain concentration, the cells were passaged and double the previous doxorubicin concentration was used for stepwise selection of resistant cells; a final concentration of 320 nM doxorubicin was applied. Before any further experiment, the doxorubicin resistant cells were maintained in doxorubicin free medium for at least 2 days [21].

4.3 MiRNA Amplification Method

Figure 4.1 compared the amplification signals from an exponential PCR reaction and our N^2 amplification. In PCR, after a short period of exponential signal increase, there is a plateau that brings the end signal to an non-distinguishable level. The plateaued PCR curve is due to the quick depletion of primers and decreased reaction rate of enzymes due to the fast amplification. However, it is essential that a linear response with miRNA concentration is present in order to give an accurate readout of the miRNA in a cell population. As shown in Figure 4.1, a non-linear relationship between signal and miRNA concentration will misrepresent the sub-population distribution. Therefore, the traditional exponential amplification method such as PCR is not suitable for end-point snapshot analysis of miRNA expression.

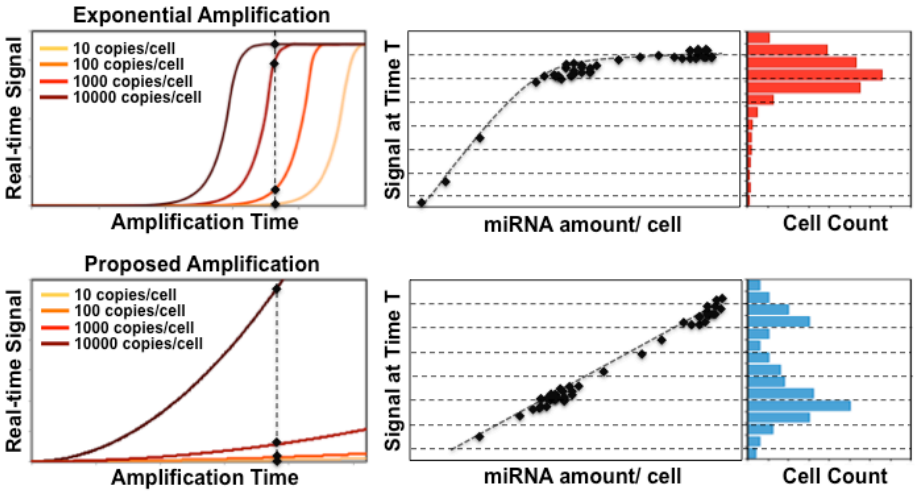

Figure 4.1 Importance of linear relationship between end-signal and miRNA content. Comparing with qPCR which gives non-linear end signal, this method can reflect the real distribution of single-cell miRNAs.

We developed a massive single-cell miRNA quantification method that analyzes the distribution of miRNA levels among 1000 single-cells per run. This method is based on an isothermal quadratic amplification that quantifies miRNA content based on fluorescent signals at the end of amplification instead of having to rely on real-time signal monitoring. A comparably constant enzyme reaction rate ensures steady signal increase in quadratic manor, therefore this method gives end fluorescence signals that are linear to miRNA concentrations across at least 3 orders of magnitude.

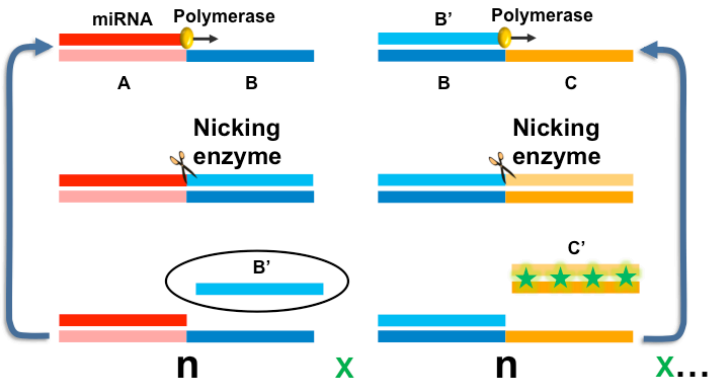

Figure 4.2 N^2 miRNA amplification mechanism. Two-step linear amplification of the initial miRNA results in a total N^2 amplification signal detected by intercalating dye SYBR Green II.

The amplification mechanism is as shown in Figure 4.2. MiRNA amplification starts with the hybridization of miRNA with complementary primer AB at the 3' terminus of the amplification template and then extend along the template in the presence of Vent (exo$^-$) DNA polymerase and deoxyribonucleotide triphosphates (dNTPs) to form double-stranded (ds) DNA. The sequence 3'-CTCAG-5' in the middle of the amplification template is the recognition site of the nicking

endonuclease Nt.BstNBI on the lower DNA strand. Therefore, the extension product contains the double-stranded nicking-enzyme recognition site in the middle of the dsDNA. The nicking enzyme recognizes the site and cleaves the upper DNA strand at a site four bases downstream. The cleaved DNA strand containing the recognition site will extend again, and the short single-stranded DNA B' will be displaced and released according to the strand-displacement activity of Vent DNA polymerase. Thus, extension, cleavage, and strand displacement can be repeated continuously and result in the linear amplification of the target miRNA. The sequence of the released short DNA strand B' is also complementary with the secondary primer BC from the 3' end. Therefore, the released DNA strand can go through the same type of linear amplification. The second amplification product, a short DNA sequence C' is captured by another complementary sequence C, and the chain-amplification is stopped at this level. Signal is generated by the intercarlation of SYBR Green II with the double stranded products. This two fold amplification resulted in an N^2 amplification rate.

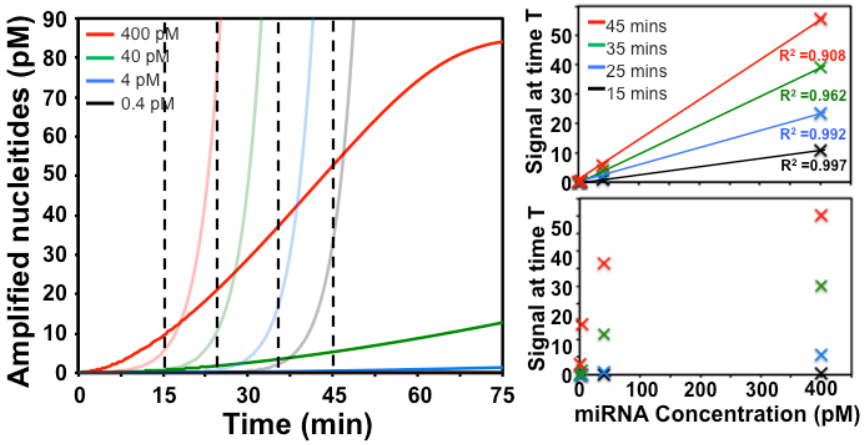

Figure 4.3 Analytical comparison of exponential and N^2 amplification for end-point data collection. The left panel depicts the amplification curves of exponential PCR (lighter curves) and N^2 amplification (brighter curves). N^2 amplification gives more linear end-point signal than exponential PCR.

Theoretically, we have analyzed the reaction rate of two hybridization steps, the polymerase elongation rate, as well as nicking enzyme reaction rate to predict the overall reaction rate to mimic the signal generation in the real reactions (Figure 4.3). In the N^2 amplification model, the signal increasing speed is slower but more static. More importantly, the signal for lower concentration of miRNA is distinguished clearly from the higher concentrations. In exponential amplification that reaches plateau, if we plot the end-signal at different time according to miRNA concentration, it is hardly linear. But for the N^2 amplification, the end-signal to miRNA concentration curve is linear.

Experimentally, we compared the signal amplification curves with our theoretical prediction, as shown in Figure 4.4. The theoretical prediction based on the above reaction rates, which took in consideration of reagent depletion fits better with the experimental curves at three different concentrations across 3 orders of

magnitude. These two curves show a slower signal increase at later stages comparing to the pure N^2 curve. But this amplification method still gives a much wider detection window for linear miRNA response comparing to PCR. Plotting end-point signal at 15 min, 25 min, 35 min and 45 min versus miRNA concentration, we get perfect linear fits ($R^2 > 0.997$) for all time points (Figure 4.4 C).

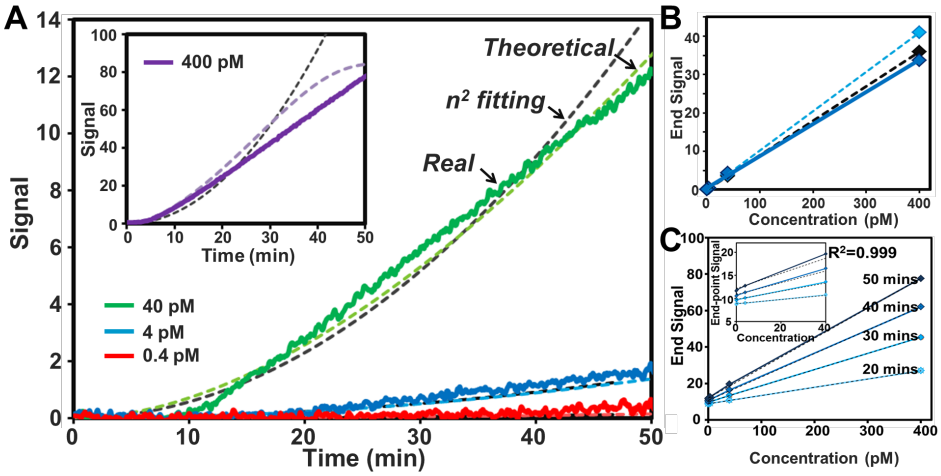

Figure 4.4 Quadratic curve fitting of real amplification curves across 3 orders of magnitude of concentrations (A). This method gives linear signal-miRNA relationships (B, C).

4.4 Microfluidic Single-cell MiRNA Detection

The single-cell miRNA detection procedure is shown in Figure 4.5, the miRNAs from single-cells are captured in pico-liter reaction wells onto magnetic microbeads. After removing cell debris, amplification reactions are initiated and fluorescent signals are generated within separated reactions wells that contain miRNAs from single-cells. The amplification takes place in a 55 ^{o}C oven for 45 mins. Fluorescent signals are captured at the end of amplification. The platform uses capillary force for sample loading and liquid exchanging. The whole process of sample preparation takes 5 drops of reagents onto the platform without using external power sources. It is easily adaptable in common laboratory environments.

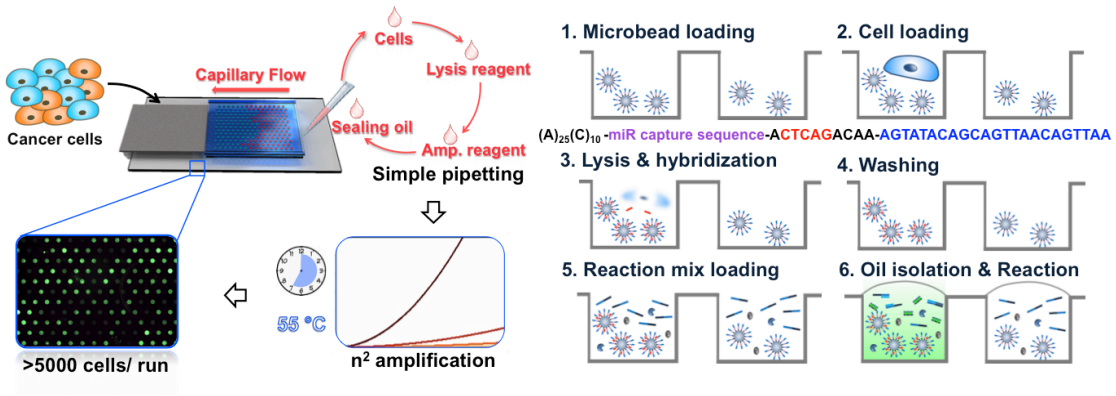

Figure 4.5 Single-cell miRNA quantification platform and operation procedures. Sample-loading by capillary flow enables easy operation; N^2 amplification enables precise end-point signal measurement from single-cells.

We have used synthetic miRNA of known concentrations to validate the experimental procedure for effectively generating linear amplification end-signal on chip. Amplification with synthetic miRNA samples also showed a linear signal to miRNA concentration relationship (Figure 4.6), which further confirmed the usability of this amplification method on microwell array chip based single-cell miRNA detection.

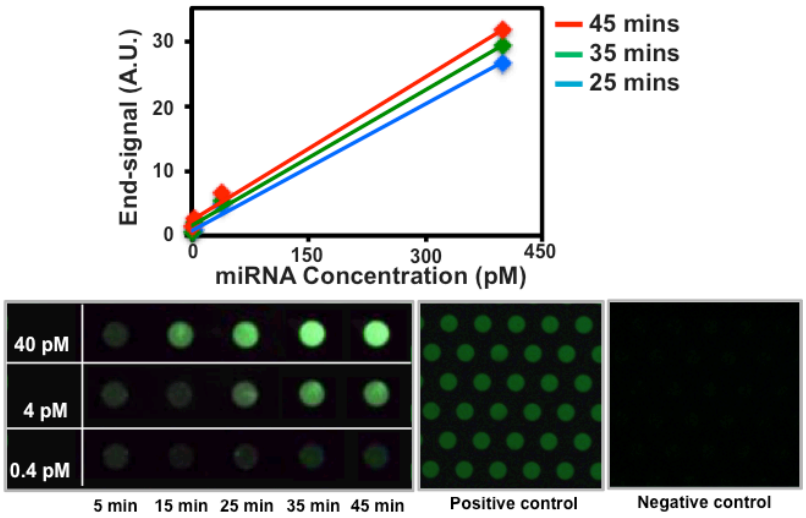

Figure 4.6 On-chip amplification signal follows linear response to concentration. Negative and positive control is implemented on chip for calibration.

Additionally, several control experiments are conducted to confirm different steps of the assay. First of all, we have confirmed that trapped bead signal does not interfere with the final fluorescent signal from miRNA amplification (Appendix E). Second, we validated that the signal we observed from microwells are indeed from miRNA amplification, instead of the fluorescence from nucleus. We observed the signal without washing off the nucleus materials (Figure 4.7). In comparison with the real signal generated from miRNA. The nucleus signal was concentrated as a bright dot inside of microwell, whereas the miRNA signal are

homogeneous in the microwell. On the other hand, if we omit the nicking enzymes in miRNA amplification, there is no amplification of miRNA signal, we can only see the concentrated bright dot from nucleus. These two aspects confirmed that the signal we observed inside of microwells is indeed from miRNA. This also emphasized the importance of washing off cell debris before performing amplification. Negative controls were also performed in without miRNA but with enzymes and primers. We did not observe fluorescent signal (Figure 4.7).

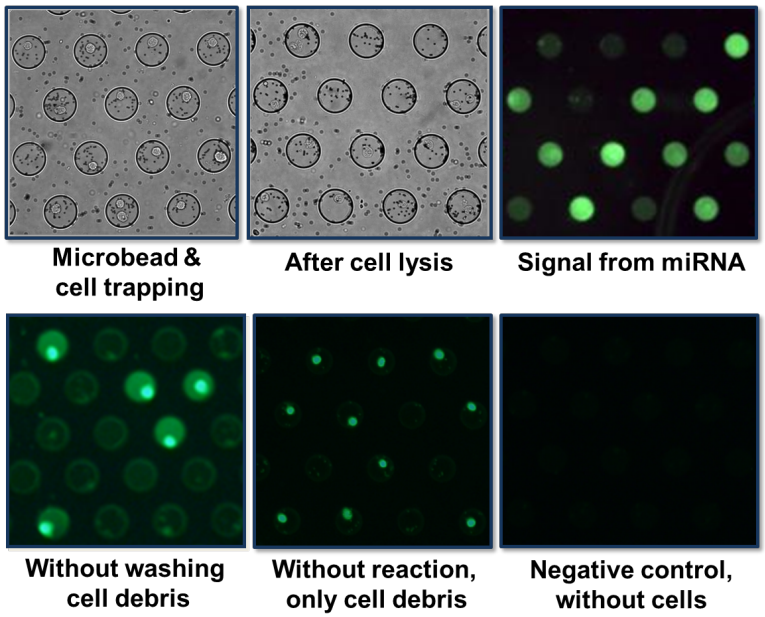

Figure 4.7 Images of mirobead and cell trapping, lysis and signal generation. Control experiments confirmed that the signals are from miRNA content of single-cells.

4.5 MiRNA Expression and Cancer Cell Drug Resistance

To demonstrate the use of this method, we quantified miRNA distributions of human breast cancer cell line MCF-7 and compared with that of the doxorubicin-resistant population. Several miRNAs showed distribution pattern and/or sub-population changes upon drug treatment, which is not shown in ensemble averages. For miR 200c, initially there is a single population with a higher expression level, whereas the drug resistant cells developed a lower expression level with a much more dispersed distribution pattern. For miRNA 21, the average amount of miRNAs increases. Originally there are two subpopulations with close miRNA expression level. After drug treatment, the lower expression cell population decreases. However, the higher expression population is shown to grow into majority and disperse into an even higher level. In the case of miR 145, we see uniform decrease after drug treatment.

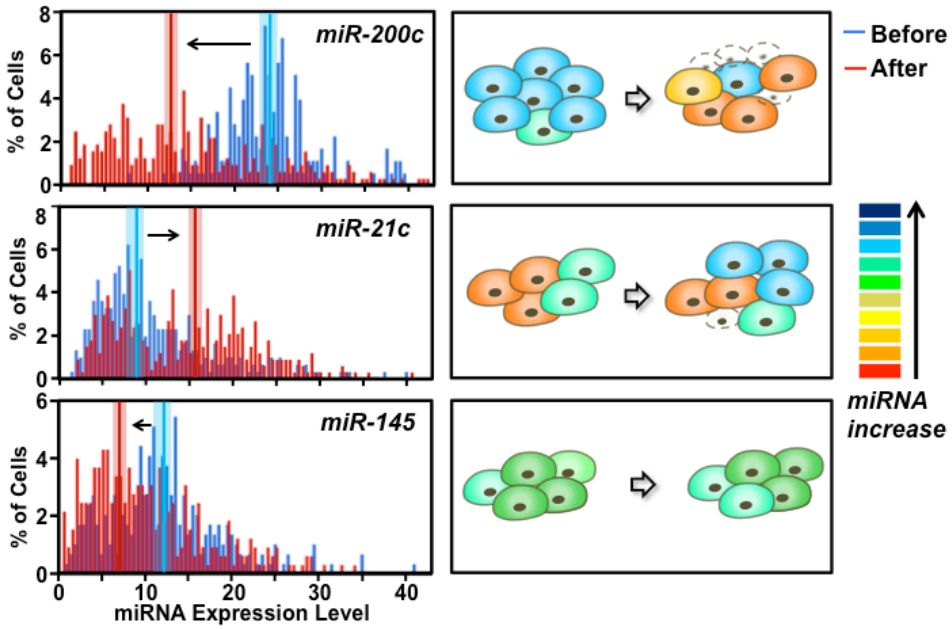

Figure 4.8 Single-cell miRNA distribution of MCF-7 cells and that of doxorubicin-resistant cells shows sup-population dynamics upon anti-cancer drug doxorubicin treatment.

4.6 Conclusion

In this chapter, we have developed a precise and massive single-cell miRNA quantification method for the study of miRNA heterogeneity in cell populations. This method is based on a unique isothermal amplification that gives end signals that are linear to miRNA content, which gives precise quantification of miRNA based on fluorescence images instead of real-time signal monitoring. The platform uses capillary force to load samples and reagents and uses mineral oil to separate single-cell reaction wells, which brings great simplicity and adaptability. We analyzed several microRNAs in human breast cancer cell line MCF-7 and their change of distribution in doxorubicin-resistant cells. We have shown for the first time the microRNA-dependent sub-populations, which respond differently to doxorubicin treatment, resulting in sub-population re-distribution in drug-resistant cells.

References

[1] Lu, J., Tsourkas, A., Nucleic Acids Res., 2009, 37, e100.
[2] Kim, V. N., Nat. Rev. Mol. Cell Biol., 2005, 6, 376-385.
[3] Couzin, J., Science, 2005, 310, 766-767.
[4] Chen, C. Z., N. Engl. J. Med., 2005, 353,1768-1771.
[5] Mendell, J. T., Cell Cycle, 2005, 4, 1179-1184.

[6] Lu, J., Getz, G., Miska, E. A., Alvarez-Saavedra, E., Lamb, J., Peck, D., Sweet-Cordero, A., Ebert, B. L., Mak, R. H., Ferrando, A. A., Nature, 2005, 435, 834-838.
[7] Calin, G. A., Sevignani, C., Dumitru, C. D., Hyslop, T., Noch, E., Yendamuri, S., Shimizu, M., Rattan, S., Bullrich, F., Negrini, M., Proc. Natl Acad. Sci. USA, 2004, 101, 2999-3004.
[8] He, L., Thomson, J. M., Hemann, M. T., Hernando-Monge, E., Mu, D., Goodson, S., Powers, S., Cordon-Cardo, C., Lowe, S. W., Hannon, G. J., Nature, 2005, 435, 828-833.
[9] He, H., Jazdzewski, K., Li, W., Liyanarachchi, S., Nagy, R., Volinia, S., Calin, G. A., Liu, C. G., Franssila, K., Suster, S., Proc. Natl Acad. Sci. USA, 2005,102,19075-19080.
[10] Dostie, J., Mourelatos, Z., Yang, M., Sharma, A., Dreyfuss, G., RNA 2003, 9, 180-186.
[11] Pfeffer, S., Zavolan, M., Grasser, F. A., Chien, M., Russo, J. J., Ju, J., John, B., Enright, A. J., Marks, D., Sander, C., Science, 2004, 304, 734-736.
[12] Poy, M. N., Eliasson, L., Krutzfeldt, J., Kuwajima, S., Ma, X., Macdonald, P. E., Pfeffer, S., Tuschl, T., Rajewsky, N., Rorsman, P., Nature, 2004, 432, 226-230.
[13] Bartel, D. P., Cell, 2004,116, 281-297.
[14] Gaarz, A., Debey-Pascher, S., Classen, S., Eggle, D., Gathof, B., Chen, J., Fan, J-B., Voss, T., Schultze, J. L., Staratschek-Jox, A., J Mol Diagn., 2010, 12, 335–344.
[15] Chen, C. F., Ridzon, D. A., Broomer, A. J., Zhou, Z. H., Lee, D. H., Nguyen, J. T., Barbisin, M., Xu, N. L., Mahuvakar, V. R., Andersen, M. R., Lao, K. Q., Livak, K. J., Guegler, K. J., Nucleic Acids Res., 2005, 33, e179.
[16] Lu, J., Tsourkas, A., Nucleic Acids Res., 2009, 37, e100.
[17] https://www.qiagen.com
[18] https://www.thermofisher.com
[19] https://www.fluidigm.com
[20] Jia, H. X., Li, Z. P., Liu, C. H., Cheng, Y. Q., Angew. Chem. Int. Ed., 2010, 49, 5498 –5501.
[21] Abu Hammad, S., Zihlif, M., Genomics, 2013, 101, 213-220.

Chapter 5. Geometry-induced Injection Dispersion in Electrophoretic Cytometry

5.1 Introduction

Microfluidic devices have found growing utility in the life sciences. Two canonical examples that derive performance enhancements from microfluidic implementations are high performance electrophoretic separations and, more recently, high throughput analyses of single cells. For electrophoresis, miniaturized chips provided approaches for controlling separation-degrading band broadening including through fine control of injected sample plugs (i.e., minimizing injection dispersion) and efficient dissipation of Joule heating during high applied electric field operation [1]. For cytometry, measurements have been buoyed by advances in design and dissemination of microfluidic tools. Both precise manipulation of single cells (and small fluid volumes) and the capacity for operating hundreds of manipulations in parallel provide key functions for single-cell analyses, including single-cell genomics and transcriptomics. Developing at the intersection of these two areas of inquiry are microdevices that are maturing the capabilities and performance of single-cell electrophoresis, an assay class that complements work horse immunoassays (i.e., flow cyomtery, mass cytometry, immunocytochemistry, ELISA) and the powerful approaches of mass spectrometry.

Although single-cell electrophoresis has been successfully performed in enclosed microdevices [19], so-called “open fluidic” devices afford assay throughput, multiplexing, and ease of use not readily accessible with microchannel or even capillary systems. Early single-cell gel electrophoresis assays isolated individual cells for electrophoretic analysis of DNA damage in a COMET assay [29-31]. Single-cell handing was achieved through control of cell suspension density, wherein sparse cell samples were embedded in layers of molten agarose. Once cooled and the cells lysed in-situ, the agarose acted as a sieving gel for DNA electrophoresis. Woods et al., performed COMET assays not in layered agarose but in agarose abutting cell-laden microwells stippled in the agarose layer. Inclusion of microwells allowed the researchers to precisely seat individual cells at specific locations on their chip prior to DNA electrophoresis [29].

Even prior to microwell-based single-cell COMET assays, arrays of microwells found use in myriad single cell analyses as the structures allow for effective cell capture, high density patterning, and compatibility with imaging [25-33]. Further, fabrication of microwells in hydrogels is rapid and straightforward to perform [26]. Circular microwells are widely used, as the shape matches the shape of single mammalian cells in suspension [32]. Matching the dimensions of the microwell to the suspended cells results in ready isolation of large numbers of individual cells,

even using gravity-based sedimentation as a seating mechanism [33, 34]. Rectangular microwells can be found in actively valved microfluidic chips [35], and microwells of different shapes are used in combination for identification of locations during microwell imaging [36].

Nevertheless, when developing high performance electrophoresis of any sample – single cells or otherwise – the downstream separation benefits from minimizing the dispersion (band broadening) imparted through the process of sample injection. In a microwell-based single-cell electrophoresis, achieving high performance analysis thus relies on understanding the interplay of microwell geometry with transport phenomena (diffusion, electromigration).

The important design question regarding injector geometry has been considered for electrophoresis in microchannels. For example, different versions of t-injectors were developed for control of the size and shape of electrophoretically injected sample plugs [19]. The geometries of the electrophoresis microchannel into which the sample plug is injected have also been considered. Peak skewing as separating species migrate along a serpentine capillary or microchannel are one set of examples [2-4]. In this case, molecular diffusion can counteract the convective peak dispersion caused by a "racetrack" effect. Jacobson *et al.* presented theoretical solutions and experimental results on peak dispersion in turn geometries. The authors linked peak dispersion to the angle of the turn and to the width of the separation channel [5]. Successive studies on the effect of symmetric and asymmetric turn geometries on separation resolution followed [6-12] with numerous design innovations in modifying the taper ratio, geometries, wall surface properties, and zeta potential [13-18].

The 'open fluidic' device designs under study have a throughput dictated by the density of single cell separations (i.e., microwell and abutting PAGE region) that can be packed into the foot print of a microscope slide. To analyze thousands of individual cells with one microdevice, the link between throughput and device separations density necessitates a millimeters-long PAGE separation axis adjacent to each microwell.

In the present study, we scrutinize the choice of microwell geometry and electrophoretic operating conditions for achieving high performance single-cell polyacrylamide gel electrophoresis (PAGE) for proteins. In particular, we assess the sensitivity of protein PAGE performance using as a sample injector one of three canonical microwell geometries: circular, rectangular, and triangular. We develop and validate a numerical model of band broadening (dispersion) using a well-characterized protein ladder and a range of operating conditions, captured through the Peclet number (*Pe*). We then apply the combined model and experimental system to assess critical separation metrics including separation resolution and assay throughput, thus guiding design of microwells for microwell-based, single-cell PAGE even for non-spherical suspended cells and adherent cells that are also non-spherical.

5.2 Materials and Methods

Chemicals. TurboGFP purified protein (tGFP, FP552, 26kDa) was purchased from Evrogen. Alexa Fluor 488-labeled purified Oval albumin (OVA, T23011, 20 kDa) was purchased from Life Technologies. Tetramethylethy- lenediamine (TEMED, T9281), ammonium persulfate (APS, A3678), β-mercaptoethanol (M3148), and 30%T, 2.7%C acrylamide/bis-acrylamide (37.5:1) (A3699) were purchased from Sigma-Aldrich. Triton X-100 (BP-151) was purchased from ThermoFisher Scientific. Premixed 10× Tris/glycine/SDS PAGE buffer (25 mM Tris, pH 8.3; 192 mM glycine; 0.1% SDS) was purchased from BioRad. Deionized water (18.2 MΩ) was obtained using an Ultrapure water system from Millipore. N-[3-[(3-Benzoylphenyl) formamido]propyl] meth- acrylamide (BPMAC) was custom synthesized by PharmAgra Laboratories.

Numerical analyses. Analytical estimates of peak dispersion during PAGE were performed based on the theoretical models discussed below. Developed to assess the impact of diffusion, our model included two assumptions. First, we assume that diffusion out of PA gel is negligible. Second, thermal effects were neglected, with temperature assumed constant and uniform. The run buffer (1× Tris-glycine) conductivity in aqueous solution was as described by Duncombe et al. [38], and estimated to be similar to that of a PA gel cast in enclosed glass microfluidic channels. The mobility and diffusivity of the model proteins, OVA and tGFP, were estimated based on Ferguson [39] and calculated per Herr and Singh [40] and Hughes et al. [27].

Fabrication of PA gel. The SU8 mold wafer and the open fluidic microdevice were fabricated as detailed previously [25]. The microwell height is 40 μm, with the length and width of the microwell varied depending on design and as described in the text. The PA gel layer on the open fluidic device was chemically polymerized using 0.08% APS and 0.08% TEMED.

Device assembly and PAGE operation. The well-characterized ladder proteins OVA and tGFP were diluted to a final concentration of 5 μM in running buffer (1× Tris-glycine). The protein solution was added on top of pre-made PA gel and was set at room temperature for 10 mins. Joule heating induced thermal effects can cause sample band broadening in PAGE by altering buffer viscosity on the basis of bulk temperature elevation [41,42]. Especially when higher voltage is applied, excessive Joule heating can be a differential factor for peak dispersion measurement [43]. Since it is important to examine the shape-dependent peak dispersion at both low and high electric field, effective control of Joule heating needs to be implemented for experimental data collection. Previously, the effects from Joule heating can be minimized by using various cooling modes or using extremely narrow-bore channels (i.e., ≤10-μm i.d.) and low-conductivity buffer systems [44]. In this study, we took a different approach and modified the PAGE system that has decreased joule heating rate [45] and better heat dissipation by using a thin microfluidic EP system. This system is proven to keep temperature increase within 3-5^{o}C under the highest electric field used in this study, 150V/cm (Appendix G). Briefly, after proteins are loaded onto gel surface, two adhesive

spacers were added on both edge of the gel area. A cover slip was placed onto the spacer, leaving a 300 μm height space between the cover slip and gel area. Afterwards, we loaded mineral oil in between of the cover slip and gel area to completely seal the gel area with protein solutions inside of microwells. Two pieces of electric wicks (0.8 cm X 1.2 cm) were placed on both ends. The electric wicks are wetted with running buffer. Then two graphite electrodes are placed on top of the electric wicks. Voltages were applied through the graphite electrodes. This design reduced the amount and height of high conductivity running buffer and reduced the distance between electrodes, therefore kept Joule heating at minimal rate. It is worth noting that we discounted the possible peak dispersion component that is caused by temperature profile across the thickness of gel [46]. This is because the temperature gradient is relatively small within the 100 μm thin gel due to efficient heat dissipation and limited temperature increase in the modified EP system.

Imaging and data collection. Fluorescence imaging was performed during PAGE with a time-lapse acquisition mode controlled by MetaMorph software (Molecular Devices) with 200 ms exposure time, 500 ms time intervals, at 1 × 1 pixel binning through a 4× magnification objective (Olympus UPlanFLN, NA 0.45) on an Olympus IX71 inverted fluorescence microscope equipped with an Andor iXon+ EMCCD camera, ASI motorized stage, and shuttered mercury lamp light source (X-cite, Lumen Dynamics). The fluorescence intensity value was background-subtracted and normalized to the value at the start of PAGE. All images were analyzed by ImageJ 1.46r (NIH). For post-simulation data analysis, we averaged the protein concentrations along the mid-line of separation path at various time points and generated analyte concentration profiles, which were then analyzed in OriginPro 8.0 to calculate peak variances.

5.3 Results and discussion

In this study, we investigate the hypothesis that microwell geometry will not affect single-cell PAGE performance (Figure 5.1). In particular, we scrutinize the planar, open fluidic devices typically utilized for electrophoretic cytometry with endpoint fluorescence readout by a 2D microarray scanner. We consider injection dispersion and total dispersion during protein PAGE performed after electrophoretic sample injection from a circular, rectangular, or triangular microwell geometry. We assume a homogeneous applied electric field and uniform pore-size throughout the PA molecular sieving matrix

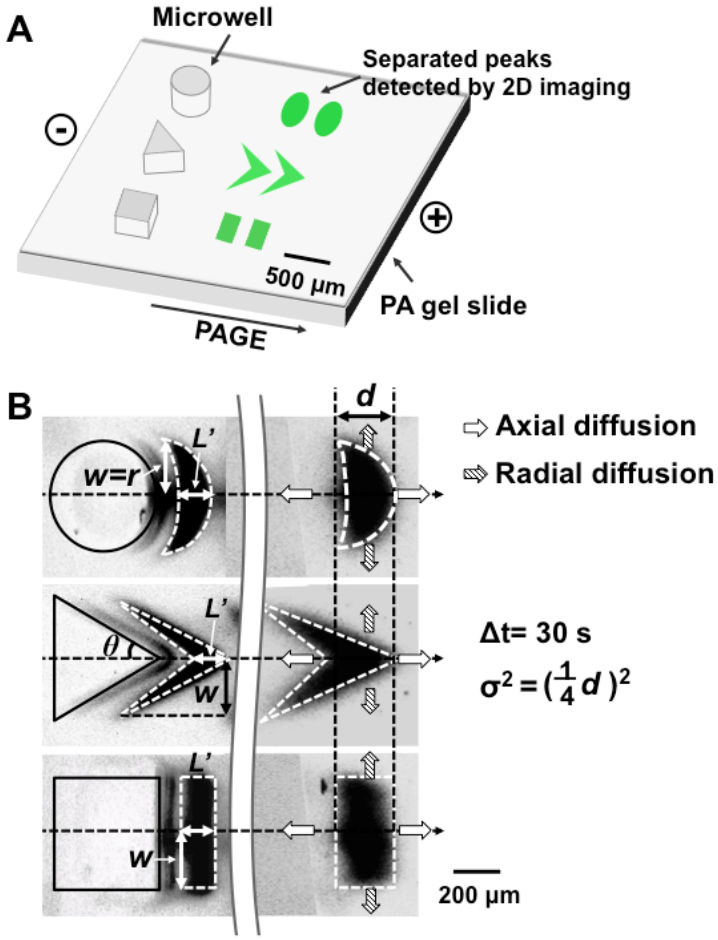

Figure *5.1* Electrophoretic cytometry in an 'open fluidic' device that comprises a thin-layer of PA gel stippled with microwells for cell isolation with a PAGE separation region abutting each microwell. (A) Schematic of an open fluidic PA gel device housing the three microwell geometries studied here and a contiguous PAGE region for each microwell. To complete single-cell PAGE, a single cell is settled into each microwell, lysed in-situ using a chemical lysis buffer, and then the single-cell lysate is electrophoretically injected through the microwell walls and into the proximal PA gel region where lysate is subjected to protein PAGE. (B) Inverted grayscale fluorescence micrographs illustrate injection of protein sample from microwell into proximal PA gel sieving matrix. The peak width is defined as the mid-line width of each peak, shown as d, and the peak variance is derived from d. Different shapes of microwells has the same characteristic length w, which is defined as shown. The injected band has a half width of w, and a mid-line length of L'. After injection, an interplay of the initial injected peak shape, axial diffusion, and radial diffusion determine the final peak shape and peak variance.

To compare PAGE performance among device designs and operating conditions, we define the ratio ($\frac{L'}{w}$), which is a comparison of the length and the width of each analyte peak immediately after analyte injection into the PA sieving gel. Here, *w* is the characteristic length of radial diffusion and *L'* is the characteristic length of axial diffusion. *L'* can be expressed as a dependent variable of *w* (Appendix H).

Further, we define a Peclet number (*Pe*) as the ratio of the characteristic time for diffusion and advection (Figure 5.1), where:

$$Pe = \frac{\Delta U w}{D_i} \quad (1)$$

Where, D_i is the diffusion coefficient of analyte in gel and ΔU is expressed as:

$$\Delta U = \frac{L'}{L} U \quad (2)$$

Where *L* is the separation length and *U* is the average velocity of analyte in the applied, uniform electric field. In summary, for each injected peak we can compare the time scale of diffusion ($t_{radial} = \frac{w^2}{D_i}$ and $t_{axial} = \frac{L'^2}{D_i}$) with the time scale of the electrophoretic separation ($tsep. = \frac{L}{U}$) to determine whether the shape of the injected peak or diffusion is dominant.

Considering the feasible operating conditions and microwell geometries of electrophoretic cytometry for analysis of single mammalian cells in the open fluidic devices, Figure 2A locates the regimes of operation and shows that *Pe* ranges from as high as ~55 down to 0.5. Floating mammalian single-cell diameters can range from 7~8 μm (e.g. red blood cell and sperm cell) to 120 μm (e.g. mature female egg cell). For effective single-cell trapping, the microwell diameter should range from ~25 μm to ~ 350 μm [25], which means a characteristic length *w* of 10 μm to 175 μm. On the other hand, the electrophoretic velocity of a target protein and its diffusion coefficient depends on the protein types interested. The sizes of protein targets can range from ~25 kDa (e.g. GFP 27 kDa) to ~300 kDa (e.g. mTOR 289 kDa) [26]. Their mobility in PA gel can be measured or predicted with the method presented by Guttman et al and Noolandi et al [51-54]. Additionally, diffusion coefficient D_i can be predicted [55] or measured. A typical range of protein diffusion coefficient in PA gel ranges from 10^{-6} cm^2/ s to 10^{-7} cm^2/ s. With the usually applied electric fields of 40 V/cm, *Pe* = 0.2~40.

Companion micrographs of the progression of PAGE from 5 s after sample injection until 35 s of elapsed PAGE separation time are shown in Figure 5.2B.

In considering electrophoretic injection of analytes from a microwell into a PA sieving gel, we expect to observe sample stacking of the injected protein peak. Molecules entering PA gel from the free solution in microwells will be stacked with a factor of $\frac{\mu g}{\mu f}$. μ_g is the electrophoretic mobility in gel, and μ_f is the electrophoretic mobility in microwell. Depending on the mobilities of different proteins, they will be stacked at different extent [56, 57]. This is beneficial for PAGE because it significantly lower the peak variance at the beginning of separation, and makes the design of microwell sizes less restricted. Depending on the shapes of microwell, *L'* can be expressed as a function of *w*. And the injected peak curvature can also be predicted considering the stacking effect (Appendix Figure A7). As evident from the data presented in both Figure 5.1B and Figure 5.2B, the stacking of sample during electrophoretic injection from the open microwell (i.e., microwell is devoid of PA gel) to the PA molecular sieving

gel, *L'* is usually smaller than *w* in circular microwells and square microwells. In triangular microwells, it is possible that *L'* is larger than *w* when an isosceles triangle with a very short base and small vertex angle is used.

The representative PAGE separations shown in Figure 5.2B illustrate the impact of *Pe* and microwell geometry on injected and subsequent peak shape. The characteristic length *w* remained constant for all three of the geometries studied, at each *Pe*. To isolate the effect of microwell shape and dimensions on separation performances, we held both the separation length L and electric field E as constant for all separations. Therefore, *Pe* is proportional to the product of *w* and *L'*. As *L'* is itself proportional to *w*, *Pe* is thus proportional to w^2. Increasing *w* will result in a rapid increase of *Pe*, causing the PAGE analyte peak to be dominated more by the initial injection dispersion than by diffusion.

The electrophoretic cytometry conditions studied here had a narrow range of (*L'/w*), but span a wide Pe range from 220 > Pe > 0.5. The devices and protein separations all falling into regimes of i, iii and v (Figure 5.2A). As mentioned, note that microwells with *L'* > *w* are rare in electrophoretic cytometry due to the stacking effect that occurs during electrophoretic analyte injection from the open microwell into the PA gel sieving matrix. The stacking notably narrows the *L'* dimension, as compared to the length of the microwell feature. Consequently, the experimental results all have a negative log (*L'/w*) value.

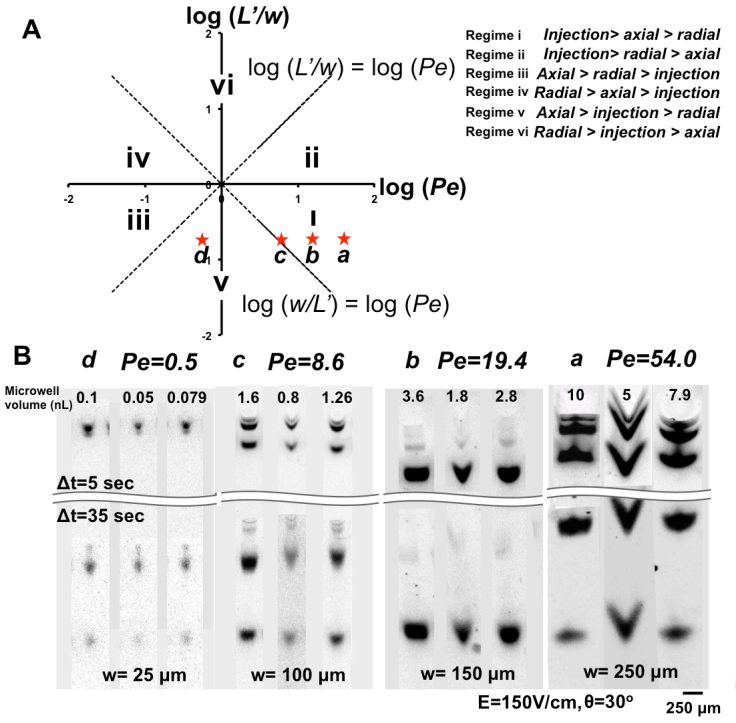

Figure 5.2 Typical dispersion regimes of electrophoretic cytometry. (A) Dispersion regions and conditions explored for electrophoretic cytometry (noted by red stars). (B) Inverted grayscale micrographs of representative PAGE from each dispersion regime starred in (A). PAGE of tGFP and OVA proteins at conditions E=150 V/cm with an elapsed PAGE time 35 s. Microwell characteristic lengths are 250 μm, 150 μm, 100 μm and 25 μm with θ=30˚ for all triangular microwells.

Among the same group of one characteristic length, the fluid volume contained in various shapes of microwells is different. As indicated in Figure 5.2, rectangular microwells contain the highest volume whereas triangular microwells the least. However, the differences in injected protein volume do not interfere with mid-line peak variance measurement, as long as the gel is not saturated. This is because we designed the microwells to have the same axial length at mid-line within the same characteristic length group. Between those groups, however, the axial length increases from left to right (Figure 5.2B). This is the cause of an overall higher peak width in high Pe conditions, unavoidably. However, the microwell shapes are more recognizable at high Pe conditions. Upon detailed analysis of peak variance progression (discussed below), we will see that the microwell shape on peak variance is more impactful at high *Pe* (i.e. larger characteristic length) regimes and plays a lesser role in low *Pe* (i.e. smaller characteristic length) regimes.

In considering the overall PAGE separation performance, we consider the total peak dispersion, as quantified by the variance σ^2 of the analyte peak. The total dispersion arises from sources including the injection itself, radial diffusion. and axial diffusion:

$$\sigma^2 = \sigma^2_{inj.} + \sigma^2_{radial} + \sigma^2_{axial} \quad (3)$$

The injection dispersion arises, in part, from the microwell geometry (Appendix H). After injection, the temporal and spatial development of the analyte band can be described by Taylor-Aris dispersion [47-50]. Based on Taylor-Aris equations, we can derive peak variances for each of the three microwell geometries considered here (Appendix H). For triangular microwells:

$$\sigma^2_{inj} = 0.25\left(\frac{\mu g}{\mu f}\right)^2 w^2 \cot^2\theta$$

$$\sigma^2_{radial} = 0.5\cot^2\theta \ \left(1-\frac{\mu g}{\mu f}\right)^2 Dit,\ \sigma^2_{radial} = [0,\ 0.25 w^2 \cot^2\theta \ \left(1-\frac{\mu g}{\mu f}\right)^2]$$

$$\sigma^2_{axial} = 2D_i t \quad (4)$$

Where μg and μf are the electrophoretic mobility of analyte molecules in gel and in the free solution-filled microwell, respectively; θ is half of the vertex angle in an isosceles triangle (Figure 5.1B), and *w* is half of the base length of the isosceles triangle.

For a circular microwell:

$$\sigma^2_{inj} = 0.25\left(\frac{\mu g}{\mu f}\right)^2 r^2$$

$$\sigma^2_{radial} = \frac{1}{X}\left(1-2\frac{\mu g}{\mu f}\right)\left(r-\sqrt{r^2-8D_i t}\right)^2,\ \sigma^2_{radial} = \left[0, \frac{1}{16}\left(1-2\frac{\mu g}{\mu f}\right) r^2\right]$$

$$\sigma^2_{axial} = 2D_i t \quad (5)$$

Where *r* is the radius of the circular microwell; *X* is a constant determined by the shape of the input response function (IRF) which creates the excess variance [48]. A Gaussian-shaped IRF has *X*=16. Jacobson *et al.* [5] used a plug-shaped IRF (*X*=12) to describe variance introduced by a bend in the separation axis.

Here, a Gaussian-shaped IRF is most appropriate for the microwell-based injection, thus we use X=16 at 4σ [6].

For rectangular microwells, the peak variance depends only on the initial injection and on the axial diffusion:

$$\sigma^2_{inj} = 0.25\left(\frac{\mu g}{\mu f}\right)^2 r^2$$

$$\sigma^2_{axial} = 2D_i t \qquad (6)$$

Analyte injected from a rectangular microwell is nominally uniform in concentration along the transverse direction, meaning that there is no radial concentration gradient. As such, the rectangular microwells exhibit an overall smaller peak variance than the circular and triangular geometries. Axial diffusion is universal across microwell geometries, whereas the impact of radial diffusion on mid-line peak variance is distinct to each microwell geometry.

We next sought to understand the contribution from each dispersion source, by using the analytical model developed above for peak variance σ^2 for the injection and PAGE processes and comparing to experimental findings. Figure 5.3 depicts the development of peak variance during the assay progression. Among the three microwell geometries, dispersion arising from the contribution of radial diffusion (red curves) is larger for triangular microwells than circular microwells, which results in an overall larger peak variance for the triangular microwells. This difference is tightly related to the initial injection shape. For triangular and circular shaped microwells, the initial "skew" of peak shape caused the concentration gradient on the radial direction, which in turn, caused the presence of radial diffusion. During PAGE from the circular and triangular microwell geometries, the transverse analyte concentration becomes uniform homogeneous at some time point during the separation. In Figure 5.3, the beginning of the plateau indicates this critical time point.

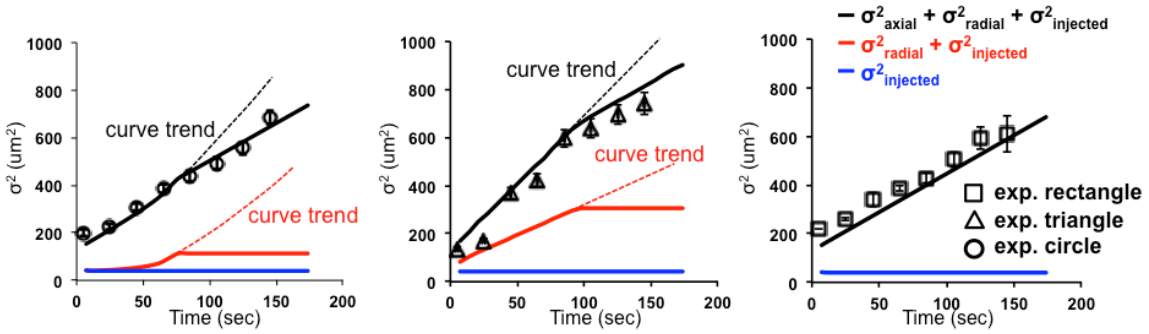

Figure 5.3 Numerical and experimental model of dispersion during PAGE conducted in the open fluidic microdevice used for electrophoretic cytometry. Comparison of experimental data from OVA separation (symbols). Error bars from 3 independent experiments indicate standard deviation. analytical model (solid lines), and trend progression after the transverse concentration of analyte becomes uniform (dashed line). Enhanced radial diffusion reaches a plateau when the transverse concentration gradient in analyte molecules becomes zero. Conditions are w=125 μm, E=40V/cm with θ=30˚ for triangular microwells. Pe=19.4

We next considered the impact of microwell geometry and the *Pe* regime on PAGE separation performance. We developed and then validated a numerical model of the peak variance during PAGE separations against PAGE experiments on two well-characterized protein ladder species (OVA, 45 kDa and tGFP, 27 kDa). As shown in Figure 5.4A, when the characteristic length *w* of a microwell decreases from 250 μm to 25 μm, the differences in peak variance are less distinguishable among the three microwell geometries. Reducing *w* also causes the analyte peak to more quickly reach uniform analyte concentration across the transverse dimension of the separation region. Especially, when characteristic length *w* is large, for triangular shaped microwells, radial diffusion caused peak variance reaches the plateau at a much later time. Therefore, the additional diffusion caused peak variance by radial diffusion has a long lasting impact on triangular shaped microwells at larger *w*. This further enlarges the differences of peak variance between triangular microwells and other shapes (Appendix Figure A8). For triangular microwells, the vertex angle affects progression of the band broadening (Appendix Figure A8). Conversely, a larger microwell brings the PAGE separation into a higher *Pe* regime, where the dominant dispersion arises from the shape of the injected analyte peak. In triangular microwells, a larger vertex angle also results in the injection dispersion being dominant (Appendix Figure A8). Keeping $\frac{L\prime}{w}$ constant, increasing *E* increases the *Pe*, bringing PAGE from diffusion dominant to operating in a regime dominated by injection dispersion (Appendix Figure A9). When considering the separation resolution (SR) of PAGE (Figure 5.4B), at higher *Pe* the triangular microwells are less favorable than the circular and rectangular microwell geometries. With the smallest microwell geometries (*Pe*=0.5), shape does not markedly affect SR.

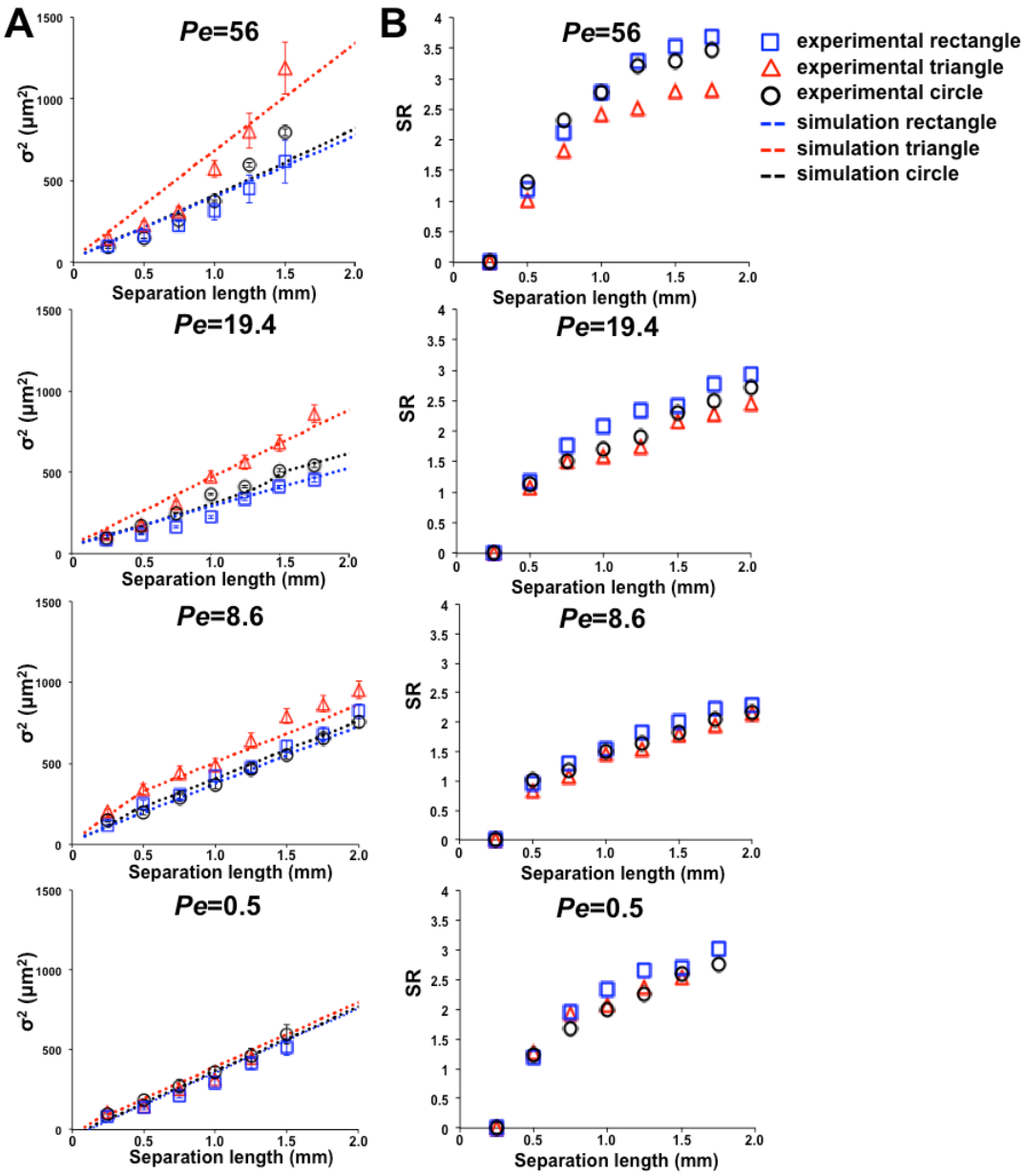

Figure 5.4 Impact of microwell geometry and operation conditions on peak dispersion and separation resolution during PAGE. (A) Progression of peak variance (s^2) for two model proteins (OVA, 35 kDa; tGFP, 27 kDa) over a PAGE separation length of 2 mm, abutting each microwell geometry. Conditions: *E*=150V/cm with characteristic lengths at *Pe* = 56 has *w* = 250 μm, *Pe* = 19.4 has *w* = 150 μm, *Pe* = 8.6 has *w* = 100 μm, and *Pe* = 0.5 has *w* = 25 μm. Analytical predictions re dotted lines with data indicated by symbols. Error bars from 3 independent experiments indicate standard deviation. Lower *Pe* exhibit less influence on peak variance from shape of the microwell. (B) Progression of PAGE separation resolution, indicating the influence of microwell shape on performance decreases with *Pe*.

Lastly, to assess the impact of microwell geometry and operating conditions on the final separation performance of the PAGE assay, we considered the elapsed

PAGE separation time at which the two ladder proteins baseline resolved from each other (*SR* > 1.5) for the three microwell geometries and across a range of *Pe* conditions relevant to electrophoretic cytometry (Figure 5.5). Our study suggests that for 19.4 > *Pe* > 0.5 and typical applied electric field strengths (*E* = 40 V/cm), PAGE separation performance was not notably impacted by microwell geometry, thus supporting our initial null hypothesis that microwell geometry does not affect single-cell PAGE performance. We did observe, however, that at the highest *Pe* studied (*Pe* = 56) under typical operating conditions the rectangular and circular microwell geometries reached baseline separation of protein species considerably faster than did the PAGE analysis from a triangular microwell. Taking a closer look, at *Pe* =14.4 when *E*=40V/cm and *w*=250 *μ*m, and at *Pe*= 19.4 when *E*=150V/cm and *w*=150 *μ*m, we still distinguish separation performances between different shapes of microwells; whereas when *Pe*=5.2 when *E*=40 V/cm and *w*=150 *μ*m, and at *Pe*=8.6 when *E*=150 V/cm and *w*=100 *μ*m, the differences between shapes are hardly noticeable. This means that *Pe,* which combines both the impact of microwell sizes and electric field, is a better and consistent indicator of the impact of injected sample shape on separation performance. This is consistent with our analysis in Figure 5.4. A higher *Pe* brings the separation into injection dispersion dominant regime, which means that the microwell shape caused injection differences will play a major role. We posit that PAGE after injection from a triangular microwell performs more poorly than the other two microwell-geometries because of a more significant contribution of radial diffusion on peak variance. At the highest *Pe* conditions where diffusion is the least contributing factor, we observe the fastest time to baseline separation in the rectangular geometry (zero skew at injection), then the circular geometry, and finally the longest time to baseline resolution with the triangular geometry. These results imply that the PAGE separation performance is insensitive to microwell geometry at low *Pe* (i.e., at lower electric field strength or smaller microwells). When *Pe* number is large, the microwell geometry should be taken into consideration in electrophoretic cytometry, especially for microwell geometries that produce “skewed” analyte peaks such as triangular microwells.

Specifically for our single-cell application, analyzing cells of a diameter that are larger than 100 μm (which means a microwell of *w*>150 μm) at an *E* of 150 V/cm, can achieve a *Pe* of 26 for a large protein. This means that microwell shapes will need to be considered in order to achieve optimal separation. Whereas analyzing cells of a diameter smaller than 50 μm (which means a microwell of *w*<100 μm), the design of microwell shapes is less important. The electrophoretic mobility (μ_g) and diffusivity (D_i) of a protein also needs to be considered in determining *Pe*. Because *Pe* is proportionally related to μ_g and inversely related to D_i, and a larger protein usually has both a smaller μ_g and D_i, the effect of both on *Pe* can be partially counteracted. While their influence on *Pe* comparing to *w* and *E* is trivial, a large protein of ~300 kDa can have a *Pe* of two times higher than a smaller protein of 25 kDa, based on analytical prediction.

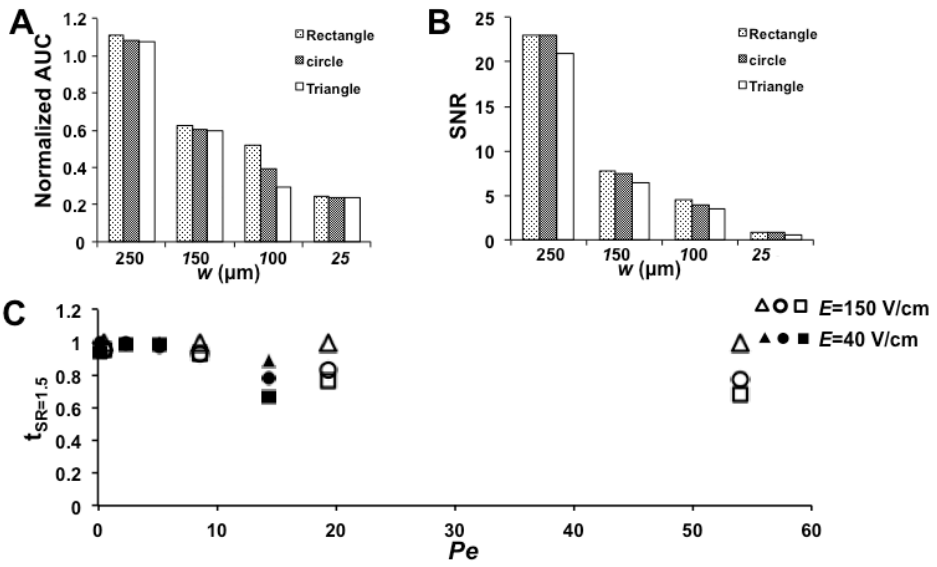

Figure 5.5 Analysis of separation performance at different *Pe*. (A) Area under curve of the peak profile at the mid-line across four w with various microwell shapes. (B) Signal-to-noise ratio of the peak profile at the mid-line across four w with various microwell shapes. (C) Elapsed PAGE separation time required exceeding baseline resolution with protein ladder. Across a range of microwell geometries the PAGE performance is not impacted by microwell geometry when the electrophoretic cytometry device is operated at E = 40 V/cm. At higher operating field strengths (E = 150 V/cm), the separation performance notably varies with *Pe* and microwell geometry. Geometrical factors w of each plot from *Pe* (high) to *Pe* (low) are: w=250 μm, w=150 μm, w=100 μm, w=25 μm. FITC-OVA and tGFP each at 100 nM; 7%T PA gel.

5.4 Conclusions

To add to the repertoire of PAGE formats (e.g., slab-gel, microchannel), we consider the electrophoretic injection of protein sample from a microwell at the head of the PAGE separation axis. Our particular interest centers on "open fluidic' devices designs developed so as to perform an array of PAGE separations, with each separation analyzing the contents of a single cell and each separation axis allowing the array to fit in the foot print of standard microscope slide. To understand the impact of operating conditions and sample injector geometry (i.e., microwell geometry) on subsequent PAGE performance, we a numerical model of key sources of band broadening (dispersion), validated the model experimentally, and applied the model to ascertaining conditions under which PAGE separation performance is affected by microwell geometry.

We examined three microwell geometries and a range of *Pe* conditions (56 > *Pe* > 0.5) and evaluated separation performance through scrutinizing band broadening and separation resolution. The combined numerical and experimental analysis suggests that microwell geometry has negligible impact on PAGE separation resolution at low-to-intermediate *Pe* (19.6 > *Pe* > 0.5), as originally hypothesized. In this open fluidic device, increasing the size of the microwells and/or the electric field strength will increase *Pe*, which in turn shifts the source

of band broadening from being dominated by axial diffusion to being dominated by either injection dispersion (and microwell geometry) or radial diffusion.

Increasing the *Pe* notably sensitizes the PAGE separation performance to the initial injection dispersion and, hence, to the microwell geometry. The accessible operating conditions also imply that – by modulating electric field strength and the geometry of microwell – one can shift the separation between operating regimes. Nevertheless, as is of central interest to this study, we observe that the separation performance of electrophoretic cytometry for analysis of single mammalian cells would be insensitive to the microwell geometry. As discussed before, in extreme cases where the largest mammalian cells are analyzed, the *Pe* can be well above the limit for microwell shape to count for separation performance. However, at the most common geometries of mammalian cells, which is below 20 μm, *Pe* is usually small enough to discount the microwell shape effect.

It is worth noting that some larger cell types do have non-spherical shapes, for example, muscle fiber cells that merge together to form syncytia [58] and neuron cells [26]. In other cases, adherent cells of various shapes may need to be analyzed [59]. In these cases, a careful scrutinize of *Pe* can be beneficial to designing microwells that brings the best separation performance.

References

[1] Gas, B., Stedry, M., Kenndler, E., Electrophoresis 1997, 18, 2123-2133.
[2] Kasicka V., Prusik Z., Gas B., Stedry M., Electrophoresis 1995, 16, 2034-2038.
[3] Srichaiyo T., Hjerten S., J Chromatography 1992, 604, 85-89.
[4] Wicar S., Vilenchik M., Belenkii A., Cohen A. S, Karger B. L., J. Microcolumn Sep. 1992, 4, 339-348.
[5] Jacobson, S. C., Hergenroden, R., Anal. Chem. 1994, 66, 1107-1113.
[6] Culbertson, C. T., Jacobson, S. C., Anal. Chem. 1998, 70, 3781-3789.
[7] Herr, A. E., Molho, J. G., Santiago, J. G., Mungal, M. G., Kenny, T. W., Garguilo, M. G., Anal. Chem. 2000, 72, 1053–1057.
[8] Paegel, B. M., Emrich, C. A., Weyemayer, G. J., Scherer, J. R., Mathies, R. A., Proc. Natl. Acad. Sci. USA 2002, 99, 574–579.
[9] Griffiths, S. K., Nilson, R. H., Anal. Chem. 2001, 73, 272–278.
[10] Dolník V, Liu S, Jovanovich S, Electrophoresis 2000, 21:41-54.
[11] Fu L. M., Yang R. J., Lee G. B., Electrophoresis 2002, 23, 602-612.
[12] Jacobson S. C., Ramsey J. R., Electrophoresis 1995, 16, 481-486.
[13] Paegel, B. M., Hutt, L. D., Simpson, P. C., Mathies, R. A., Anal. Chem. 2000, 72, 3030-3037.
[14] Molho, J. I., Herr, A. E., Mosier, B. P., Stantiago, J. G., Kenny, T. W., Anal. Chem. 2001, 73, 1350-1360.
[15] Johnson, T. J., Ross, D., Caitan, M., Locascio, L. E., Anal. Chem. 2001, 73, 3656–3661.
[16] Lee, C. Y., Lin, C. H., Fu, L. M., Analyst 2004, 129, 931–937.

[17] Lee, G. B., Fu, L. M., Lin, C. H., Lee, C. Y., Yang, R. J., Electrophoresis 2004, 25, 1879–1887.
[18] Zhuang, Z. X., Mitra, I., Hussein, A., Novotny, M. V., Mechref, Y., Jacobson, S. C., Electrophoresis 2011, 32, 246–253.
[19] Bharadwaj, R., Santiago, J. G., Mohammadi, B., Electrophoresis 2002, 23, 2729-2744.
[20] Woolley A. T., Mathies R. A., Anal. Chem. 1995, 67, 3676-3680.
[21] Zheng J. J., Odake T., Kitamori T., Sawada T., Anal. Chem. 1999, 71, 5003-5008.
[22] Demianova Z., Shimmo M., Poysa E., Franssila S., Baumann M., Electrophoresis 2007, 28, 422-428.
[23] Zhang H., Yeung E. S., Electrophoresis 2006, 27, 3609-3618.
[24] Sluszny C., Yeung E. S., Anal. Chem. 2004, 76, 1359-1365.
[25] Kang, C. C., Lin, J. M. G., Xu, Z. C., Kumar, S., Herr, A. E., Anal. Chem. 2014, 86, 10429−10436.
[26] Hughes, A. J., Spelke, D. P., Xu, Z. C., Kang, C. C., Schaffer, D. V., Herr, A. E., Nature Methods 2014, 11, 749-755.
[27] Hughes, A. J., Herr, A. E., Proc. Natl. Acad. Sci. USA 2012, 109, 21450-21455.
[28] Hughes, A. J., Lin, R. K. C., Peehl, D. M., Herr, A. E., Proc. Natl. Acad. Sci. USA 2012, 109, 5972-5977.
[29] Wood, D. K., Weingeist, D. M., Bhatiaa, S. N., Engelward, B. P., Proc. Natl. Acad. Sci. USA 2010, 107, 10008-10013.
[30] Weingeist, D. M., Ge, J., Wood, D. K., Mutamba, J. K., Huang, Q. Y., Rowland, E. A., Yaffe, M. B., Floyd, S., Engelward, B. P., Cell Cycle 2013, 12, 907-915.
[31] Olive, P. L., Banath, J. P., Nature Protocols 2006, 1, 23-29.
[32] Chen, Q. S., Wu, J., Zhang, Y. D., Lin, Z., Lin, J. M., Lab on a Chip 2012, 12, 5180-5185 .
[33] Yuan, J. Z., Sims, P. A., Scientific Reports, 2016, 6, 33883-33842.
[34] Kang, C. C., Yamauchi, K. A., Vlassakis, J., Sinkala, E., Duncombe, T. A., Herr, A. E., Nature Protocols 2016, 11, 1508-1530.
[35] Moonsamy, P.V., Williams T., Bonella P., Holcomb C. L., Hoglund B. N., Hillman G., Goodridge D., Turenchalk G. S., Blake L. A., Daigle D. A., Simen B. B., Hamilton A., May A. P., Erlich H. A., Tissue Antigens 2013, 81, 141-149.
[36] Torres, A.J., Contento, R.L., Gordo, S., Wucherpfennig, K.W., Love, J.C., Lab on a Chip 2013, 13, 90-99.
[37] Huang, X. H., Coleman, W. F., Zare, R. N., Journal of Chromatography 1989, 480, 95-110.
[38] Duncombe, T. A., Herr, A. E., Anal. Chem. 2012, 84, 8740− 8747.
[39] Ferguson, K. A., Metabolism 1964, 13, 985-1002.
[40] Herr, A. E., Singh, A. K., Anal. Chem. 2004, 76, 4727−4733.
[41] Christopher J. Evenhuis, Paul R. Haddad, Electrophoresis 2009, 30, 897–909
[42] Knox, J. H., McCormack, K. A., Chromatographia 1994, 38, 215–221.

[43] Xuan, X. C., ELECTROPHORESIS 2008, 298, 33–43.
[44] Petersen J. R., Mohammad A. A, Clinical and Forensic Applications of Capillary Electrophoresis, Humana Press Inc., Totowa, NJ; Basic Principles and Modes of Capillary Electrophoresis, Harry Whatley
[45] Petersen, N. J., Nikolajsen, R. P. H., Mogensen, K. B., Kutter, J. P., Electrophoresis 2004, 25, 253–269.
[46] Tang, G. Y., Yan, D. G., Yang, C., Gong, H. Q., Chai, J. C., Lam, Y. C., Electrophoresis 2006, 27, 628–639.
[47] Probstein, R. F., Physicochemical Hydrodynamics: An Introduction, 2nd ed., John Wiley & Sons, New York, 82-96.
[48] Sternberg, J. C. In Advances in Chromatography; Giddings, J. C., Keller, R. A., Eds.; Marcel-Dekker: New York, 1966; Vol. 2, pp 205-270.
[49] Taylor, G. I., Proc. R. Soc. London, Ser. A 1953, 219, 186-203.
[50] Aris, R., Proc. R. Soc. London. Ser. A 1956, 235, 67-77.
[51] Ogston, A. G., Trans. Faraday Soc. 1958, 54, 1754.
[52] Chung M. S., Kim, D. H., Herr, A. E., Analyst 2014, 139, 5635-5654.
[53] Guttman, A., Electrophoresis 1996, 17, 1333–1341.
[54] Noolandi, J., Annu. Rev. Phys. Chem. 1992, 43, 225-237.
[55] Young, M. E., Carroad, P. A., Bell, R. L., Biotechnology and Bioengineering 1980, 22, 947-955.
[56] Herr, A. E., Throckmorton, D. J., Davenport, A. A., Singh, A. K., Anal. Chem. 2005, 77, 585–590.
[57] Yang, S., Liu, J. K., Lee, C. S., Devoe, D. L., Lab Chip 2009, 9, 592–599.
[58] Murgia, M., Nagaraj, N., Deshmukh, A. S., Zeiler, M., Cancellara, P., Moretti, I., Reggiani, C., Schiaffino, S., Mann, M., EMBO Rep. 2015, 16, 387–395.
[59] Park, J. Y., Morgan, M., Sachs, A. N., Samorezov, J., Teller, R., Shen, Y., Pienta, K. J., Takayama, S., Microfluid Nanofluidics. 2010, 8, 263–268.

Chapter 6. Patterning polyacrylamide gels controls performance of single-cell electrophoresis

6.1 Introduction

Cell-to-cell variation in response of environmental or epigenetic clues is a hallmark of various biological processes [1]. Single-cell resolution genomic and transcriptomic measurements are advancing rapidly due to the high specific recognition by complementary nucleic acid binding and the versatile signal amplification methodologies. However, direct measurement of proteins in single cells is more challenging [2, 3]. In contemporary cellular protein measurements, a population of cells is needed to obtain sufficient signal for detection. This type of measurement reflect the collective responses but obscures the individual cell behavior. Therefore, single-cell resolution proteomic tools are desired. The commonly used approaches are immunoassay-based measurements (e.g., immunohistochemistry/ immunocytochemistry [4], flow cytometry [5, 6] and various immunosorbent assays [7] that highly depend on the suboptimal specificity of antibodies. Comparing to this strategy, a combination of electrophoretic protein separation with the antibody recognition power can provide higher specificity and resolution for wider range of protein targets, especially protein isoforms [8, 9]. This approach stresses on the separation power of electrophoresis.

The conventional combinatorial method known as western blot electrophoretically separates proteins from cell lysate by denaturing polyacrylamide gel electrophoresis (PAGE), and the protein spots are transferred to a membrane for immuno-probing [10-15]. Although it effectively uses the separation power provided by PAGE, it needs thousands of cells for each measurement, and requires labor intensive and time-consuming processes. A protein separation and probing method that provides single-cell resolution and sensitivity, as well as efficiency in analyzing large amount of single-cells is desired.

Recently, we have introduced arrayed PAGE for simultaneous analysis of hundreds-to-thousands of single-cell lysates [16]. This methodology, combined with subsequent in-gel protein capture and immuno-probing [17], is a powerful tool in advancing single-cell protein measurement in an accurate, high throughput and time-efficient manor. This arrayed PAGE method employs a microscope slide coated with a thin photoactive polyacrylamide (PA) gel, which is micropatterned with an array of microwells. Single-cells are captured and lysed inside the microwells, and the released denatured proteins are sieved through PA gel by electrophoresis. The resulted gel slide can be subjected to in-gel protein capture and immuno-probing. Although powerful in accessing single-cell

protein information in integrated manor, it requires continued innovation to improve detection sensitivity and separation resolution to meet the demand for multiplexed, trace amount of protein detection in single-cells. In the current design of single-cell PAGE, several material losses exist during the cell lyses and protein separation process. In this paper, we address these challenges by innovating device design to tackle convective and diffusive loss and Joule heating during lysis and single-cell electrophoresis steps (Figure 6.1A).

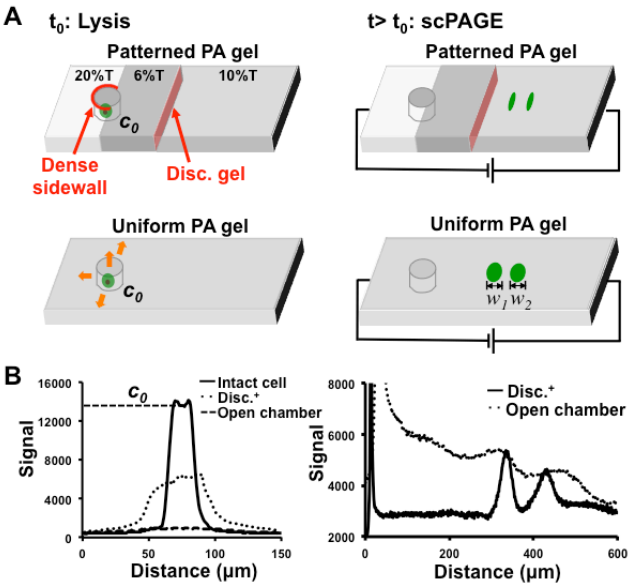

Figure 6.1 Open fluidic single-cell PAGE benefits from patterned PA gels designed to reduce analyte dispersion during cell lysis, sample injection, and electrophoresis. (A) Schematic of the *scPAGE* device, with three regions of interest (*i*) a high-density PA gel ringing the microwell to define a lower gel density sample injector region at the head of the separation axis; (*ii*) a stacking gel defined by a step change in gel density along the separation axis to reduce sample injection dispersion during *scPAGE*; and (*iii*) an agarose lid to mitigate analyte losses out of the open device. (B) Representative concentration profiles at initiation of cell lysis (t_o) and during *scPAGE* ($t > t_o$), where c_o is the concentration of analyte in the intact cell. The Disc. $^+$ condition is combining patterned PA gel with dense sidewalls and stacking region, as well as the enclosed PAGE system. The Open chamber condition is uniform gel with the open chamber PAGE system.

Firstly, in the previous single-cell PAGE, lyse of cells was realized by pouring of lyses buffer onto the device in an electrophoresis chamber. Cell membrane can be disrupted within 10 seconds of lyses [18]. Bulk buffer velocity during pouring of lyses buffer into electrophoresis chamber causes vortex in the microwell. A moderate 40.2% ± 3.6% loss of protein was observed due to diffusion of cell contents during lysis buffer introduction [18] This is particularly significant for smaller proteins because of their higher diffusion coefficient [19]. In one instance, GFP fluorescence signal was below 50% of the initial signal after 3 seconds of lysis after pouring heated lyses buffer.

Several approaches exist to prevent diffusional loss during cell lyses. For example, droplet-based microfluidics for single-cell encapsulation and detection can provide limited diffusion loss of materials from single-cell [20]. However, it does not provide separation power by interfacing electrophoresis. On the other hand, microchip capillaries are used for cell lysis and electrophoretic separation. They usually use a pulse of high voltage to break down the cell membrane, and immediately apply voltage for injection to prevent cell lysate diffusion loss [21]. Other mechanical cell lyses methods using flow shear [22], laser [23] also provide ultra fast cell membrane breaking and releasing of cytoplasma content. However, the PAGE based protein measurement and immuno-probing requires thorough lyses, denaturing, solubilization and even reduction of protein content in cells to yield quality separation. Mechanical lyses can hardly provide this level of lyses. Chemical lysis assisted with elevated temperature is by far the state of art for PAGE sample preparation. A lyses time of >25 sec is also often necessary.

To prevent dispersion loss of lysate using chemical lyses, scientists have developed enclosed, microfabricated chambers and valves [24-27] for single-cell trapping, lyses and subsequent cell content analysis on chip. These methods demonstrated robust cell and reagent handling and reproducible results. However, they depend on valve based fluidic handling for reagent exchange and delivery, which often requires sophisticated designing and fabrication, as well as external control systems.

To build on this integrated and stand-alone single-cell capture, lysis and electrophoresis open microarray with a diffusion limited design, we constructed a selective permeable ultra thin (100-200 μm) agarose layer on top of PA gel to enclose microwells after cells are captured. This agarose lid allows ions and surfactants in the lyses buffer to penetrate through and lyse the cells, whereas proteins can hardly escape through this layer due to the sieving effect. We also designed a high density gel area at the head of injection zone surrounding the microwell to prevent diffusion on the planar directions during lysis. The protein retaining rate during lyses was improved from 10% previously to 30% (Figure 6.1B).

The second protein loss is the diffusional loss out of the sieving matrix during separation. To facilitate rapid material (i.e. antibody) transport during immuno-probing, the PA gel was designed to have a thickness of only 40 μm. However, this thin geometry also provides the possibility for the target protein to be diffused out of gel. Furthermore, diffusion caused peak broadening becomes a more significant challenge in this ultra-short separation scheme. The injected protein peaks become dispersed over time due to molecular diffusion. These two aspects of diffusion caused separation deficiencies are accelerated by the severe (20~30 ^{o}C) temperature increase during separation due to Joule heating [27-31]. Joule heating in conjunction with the geometry of the liquid conduit and the material properties of the surrounding bulk materials causes a radial temperature profile to be established [37]. This radial temperature profile can contribute to band broadening by introducing a parabolic flow component. More importantly, the diffusion coefficient of proteins is also dependent on temperature. A higher

temperature results in more dispersed peaks. Controlling heating can be an effective approach to minimize the diffusion loss out of PA gel and the peak dispersion during separation.

In previous studies, several approaches were introduced to limit the effect of Joule heating. Scientists have modified the content of separation buffer to lower heating and eliminate counterflows [32-34]. However, our buffer composition is constrained by the need for effective cell lysis, protein denature, solubilization and charging. Therefore it cannot have extremely low conductivity. Others have sort to adjust the separation platform design and material to decrease bulk-heating amount and improve heat dissipation [35, 36]. It is widely accepted that using smaller capillary diameters can limit temperature increase during capillary electrophoresis. Thermostats are also used for better heat dissipation [37]. It is also tested that using thermal conductivity to dissipate heat is efficient in conventional capillaries and microfabricated devices [38]. The heat dissipation from a nonthermostatically controlled glass microdevice was found to be comparable to that from a liquid-cooled-fused silica capillary [37]. This is mainly due to the better heat dissipation in those devices because of a larger thermal mass and a better surface-to-volume ratio, and the devices themselves may also work as heat sinks if the separation were operated within short period of time.

Therefore, we have miniaturized the lyses and electrophoresis setting to completely change from buffer pouring and large open chamber based electrophoresis, to an gel-encapsulated, enclosed microchip electrophoresis. The new device drastically reduced the thickness of heat generating buffer layer and the distance between electrodes, and increased thermal mass with glass slides. These improvements reduced the voltage and current that is applied to the device while generating the same amount of electric field. The higher surface-to-volume ratio also improved heat dissipation. Temperature in the device was kept constant during the whole electrophoresis comparing to the significant temperature increase of 0.65^{o}/ sec in the open chamber device. As a consequence, the diffusion loss of various proteins during electrophoresis was significantly lowered from 70% to 30%~60% depending on protein size.

Finally, to further reduce peak dispersion during protein injection, we have implemented a photo-patterned discontinuous gel region to create pore-size induced protein stacking at the early stage of separation. The diffusion caused band broadening during injection was counteracted by immediate stacking following injection. By carefully rationalizing the length of stacking region with analytical prediction, we have achieved an even narrower injection band than the initial injection after stacking, and the separation resolution was improved from the previous SR=0.5 to SR=1.5 for model protein mix BSA (65 kDa) and OVA (45 kDa).

Overall, with the above three-fold advances to progress the detection sensitivity and separation performance of single-cell PAGE, we have achieved a signal-to-noise ratio of 2 times higher than the previous open chamber device. The heat dissipation was effective to the point that the temperature was maintained at room temperature during the whole electrophoresis process. Molecular diffusion

was significantly reduced. We also applied a photo-patterned PA gel to create protein-stacking effect to reduce injection dispersion. As a result, the protein retaining rate improved 2~4 times and the separation resolution increased 3 times (Figure 6.1B).

6.2 Materials and Methods

Chemicals

1% (w/v) VA-086 (photoinitiator) was purchased from Waco Chemical. Tetramethylethy- lenediamine (TEMED, T9281), ammonium persulfate (APS, A3678), β-mercaptoethanol (M3148), and 30%T, 2.7%C acrylamide/bis-acrylamide (37.5:1) (A3699) were purchased from Sigma-Aldrich. Triton X-100 (BP-151) was purchased from ThermoFisher Scientific. Premixed 10× Tris/glycine/SDS electrophoresis buffer (25 mM Tris, pH 8.3; 192 mM glycine; 0.1% SDS) was purchased from BioRad. Deionized water (18.2 MΩ) was obtained using an Ultrapure water system from Millipore. The cell lyses and electrophoresis buffer contains 0.5% SDS, 0.1% v/v Triton X-100, 0.25% sodium deoxycholate (D6750, Sigma- Aldrich) in 12.5 mM Tris, 96 mM glycine, pH 8.3, (0.5× from a 10× stock, 161-0734, Bio-Rad)

Cell Lines

U251-GFP human glioblastoma cells stably transduced with GFP by lentiviral infection (multiplicity of infection = 10) were kindly provided by Dr. Ching-Wei Chang in Prof. S. Kumar's Laboratory and maintained in high glucose DMEM (11965, Life Technologies) supplemented with 1 mM sodium pyruvate (11360-070, Life Technologies), 1× MEM nonessential amino acids (11140050, Life Tech- nologies), 1% penicillin/streptomycin (15140122, Invitrogen), and 10% of calf serum (JR Scientific) and maintained in a humidified 37 °C incubator with 5% CO_2.

SU8 wafer and gel slides fabrication

The microwell feature heights and diameters were 40 and 50 μm throughout the experiments. The chemically polymerized PA gel for control experiments was made using photo-initiators 0.08% APS and 0.08% TEMED. For photo-polymerized gradient gels, the precursor solution contains 1% (w/v) 2,2-azobis[2-methyl- N-(2-hydroxyethyl) propionamide] (VA-086) photo-initiator and acrylamide monomer concentrations of 20% (w/v). The precursor was degassed under house vacuum and sonication for 3 min immediately before polymerization. The grayscale of the mask was designed with AutoCAD. The mask was further fabricated on soda lime glass by Front Range Photomask, LLC. (Palmer Lake, CO, USA) which was able to fabricate masks with tens of millions of features. Before UV-activated photopolymerization, the glass-SU8 mold and the grayscale chrome mask were aligned under an OAI Hybralign Series 400 (Optical Associates, Inc., San Jose, CA, USA) mask aligner. The setup on the aligner and UV exposer in the order of the light path was: grayscale chrome mask, methacrylate- functionalized glass slide (functional group facing down), gel

precursor solution and glass-SU8 mold. After alignment, the setup was exposed to UV (19mW/cm^2) for 25 sec to polymerize PA gel. After polymerization, the gels were carefully removed from the mold using a razor blade.

Allylamine gel density imaging

To enable direct imaging of PAG density gradient, allylamine was added to the gel precursor solution at a 1:100 molar ratio with acrylamide [39,40]. The allyl group incorporates directly into the acrylamide fibers during free-radical polymerization. UV exposure time was increased by ~33% as the allyl group slows polymerization [41]. The resulting allylamine gels were soaked in 0.1 mg mL-1 fluorescein isothiocyanate (FITC, Isomer-I, Invitrogen) in DI water overnight. The primary amine has a positive charge in water and reacts with the negatively charged carboxyl group on the FITC molecule. Excess FITC is washed away in water for a minimum of 2 hours. The allylamine incorporated gradient gels were then imaged under an epi-fluorescence microscope.

Sample loading on PA gel slides

For purified protein experiments, Alexa Fluor 488-labeled purified bovine serum albumin (BSA, A13100) and Alexa Fluor 488-labeled purified ovalbumin (OVA, O34781) were purchased from Thermo Fisher Scientific. Turbo-GFP (GFP, FP552) was purchased from Evrogen. The purified proteins were diluted to a final concentration of 1 µM in lyses buffer. We incubated the purified protein with different %T of PA gel for 15 min and then performed PAGE. For single-cell experiments, cultured cells in flask were lifted off by trypsin incubation. Then the cell solution was centrifuged to remove trypsin and re-suspended in ice cold PBS to result a final concentration of 5.0 x 10^6 cells/mL. Then 200 µL cell solution was pipetted onto PA gel slide and sit for 5-10 mins for single cells to gravity-settle into microwells. This was followed by three times of washing by PBS to remove excess cells off the surface. Then the slide was subjected to cell lyses and PAGE as described below.

PAGE on open chamber device

The open chamber device was made of acrylonitrile butadiene styrene by in house 3D printing. The chamber has a dimension of 3 cm (width) x 8cm (length) x 3cm (height). Platinum wires (0.5-mm diameter, 267228, Sigma-Aldrich) were placed along the long edge of the chamber and interfaced with alligator clips to a standard electrophoresis power supply (Model 250/2.5, Bio-Rad). After sample (purified protein or cell) loading, the PA gel slide was placed on the bottom of the open chamber and the whole device was mounted on the stage of fluorescence microscope for real-time imaging. Afterwards, 10 mL lyses buffer was poured into the chamber and was sit still for 35 sec. For gel slides with cells, this process enables cell lyses. In order to be consistent, gel slides with purified protein also was subjected to 35 sec incubation with lyses buffer. Then electric field was applied to the chamber to allow injection and electrophoresis of the target proteins. We kept a consistent electric field of 50V/ cm for both open chamber and enclosed device. Due to the wider width (3cm) of open chamber device, 150V total voltage was applied.

PAGE on enclosed device

The cross section of the enclosed device setting was shown in Figure 6.1. The PA gel slide was modified with two strips of plastic spacer attached to the two sides of the gel where there will not be electrodes. After sample loading (i.e. purified protein incubation or cell settling and washing), 0.5mL pre-dissolved and cooled 1% agarose precursor solution was added on top of the PA gel. The precursor was made with PBS to prevent cell rapture. Immediately, a glass slide was placed on top of the agarose gel solution and gently pressed down onto the spacers. Agarose gel rapidly at lowered temperature and form a thin layer encapsulating microwells. Then the glass slide was slide off the gel to reveal a smooth surface of agarose layer. Afterwards, two strips of electric wicks was placed on the open sides (the other two sides without spacers) of the gel, and was connected to graphite electrodes. 200 µL of lyses buffer was pipetted on top of the agarose gel layer and the device was sit still for 45 sec for buffer diffusion and cell lyses. Again, purified protein samples were also subjected to this incubation for consistent condition. Immediately after, 50V/cm electric field was applied for electrophoresis. Due to the smaller distance (1cm) between electrodes in this setting, 50V of voltage was applied to generate the same amount of electric field as for the open chamber device.

Fluorescence Imaging

Real-time cell lysis and electrophoresis was imaged using a time-lapse acquisition mode controlled by MetaMorph software (Molecular Devices) with 200 ms exposure times, 1s time intervals, at 1 × 1 pixel binning through a 10× magnification objective (Olympus UPlanFLN, NA 0.45) on an Olympus IX71 inverted fluorescence microscope equipped with an Andor iXon+ EMCCD camera, ASI motorized stage, and shuttered mercury lamp light source (X-cite, Lumen Dynam- ics). Fluorescence signal from a region of interest (ROI) was integrated at intervals during lysis and electrophoresis. Fluorescence signal from an adjacent area was assigned as the background signal. Each integrated intensity value was background- subtracted. All images were analyzed by ImageJ 1.46r (NIH). Besides, quantification of protein PAGE used in-house scripts. Bands widths, heights and locations were characterized by Gaussian curve fitting in MATLAB (R2013b, Curve Fitting Toolbox).

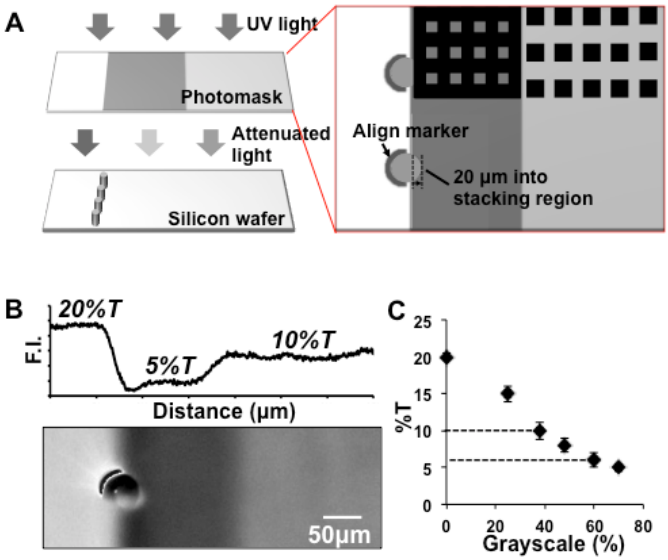

Figure 6.2 Grayscale photopatterning technique for creating patterened PA gels aligned to microwells. (A) Schematic of grayscale photopatterning technique used to create and align high density PA gel to the microwell. (B) Step change in PA gel density (stacking gel) along the separation axis measured by FITC fluorescence incorporated into the gel scaffold. (C) Calibration of grayscale with the resulted gel density. For patterning a 6%T stacking gel and a 10%T separation gel, 60% and 40% grayscale was used respectively.

6.3 Photo-patterned Discontinuous PA Gel

Previously, we have developed a fabrication approach combining grayscale photolithography and SU-8 mold patterning to create pore-gradient PA gels. Central to this technique is a chrome grayscale mask, which spatially attenuates UV intensity [23], thus locally altering the rate of free-radical production and polymerization [24]. If polymerization is halted prior to completion, the grayscale mask opacity determines the local effective gel density. Here, we have employed this technique to fabricate discontinuous pore-size gel that has distinctive gel boundaries of various densities. Figure 6.2A depicts the UV exposure setting and a small portion of the grayscale mask design in the stacking gel and separation gel region. The grayscale was created by arrays of opaque squares of 5-30 μm sizes patterned at different densities [23]. The grayscale level was calculated as the percentage of areas covered with opaque squares. For example, a grayscale of 60% means that 60% of the area is opaque and 40% is transparent. Two distinct grayscale areas are placed next to each other, with the surrounding area 100% transparent. We intend to create: a very high gel density of ~20% T surrounding the head part of microwells to prevent planar diffusion loss during cell lyses; a low density (~6%T) region at the injection portion next to microwells to allow quick injection of proteins and subsequent stacking; a medium density (~10%T) separation gel following the second region to allow pore-size stacking and separation.

It is essential to align the injection edge of the microwells at the 20%T and 6%T boundary to ensure that the 20%T region does not block the injection outlet of

the microwell so that no de-stacking exists. We used alignment markers (Figure 6.2A) on the photomask to perfectly align microwells consistently. We also used a standard photolithography OAI aligner (OAI Hybralign Series 400) with microscope and projection to ensure alignment quality. The aligner ensures that microwell features on the SU-8 mold sit approximately 20 μm into the injection region (Figure 6.2A). The gel precursor was exposed to UV to activate the azo-initiator for an optimized period of time to result in desired density patterns.

To visualize the resultant photo-patterned PA gel, we incorporated allylamine in the gel precursor solution (1:100 molar ratio with acrylamide), then labeled the primary amine with fluorescein isothiocyanate (FITC). FITC fluorescence intensity reflects acrylamide density [19]. By imaging FITC, we can visualize the patterned gel (Figure 6.2B). It is seen that the fluorescent intensity corresponds to the desired density level in each region. To more precisely assess the gel density, we assayed a model GFP electrophoresis mobility across different grayscales of patterned gel, and calibrated the local GFP mobility to the mobilities measured in chemically polymerized uniform pore-size gels (Figure 6.2C). To prevent Joule heating effect on this mobility measurement, the temperature-controlled enclosed device was used (discussed below), and a short separation time was applied. According to the calibration plot, we finalized the grayscales of 0%, 40% and 60% to be used to yield a 20%T-6%T-10%T stepwise pattern.

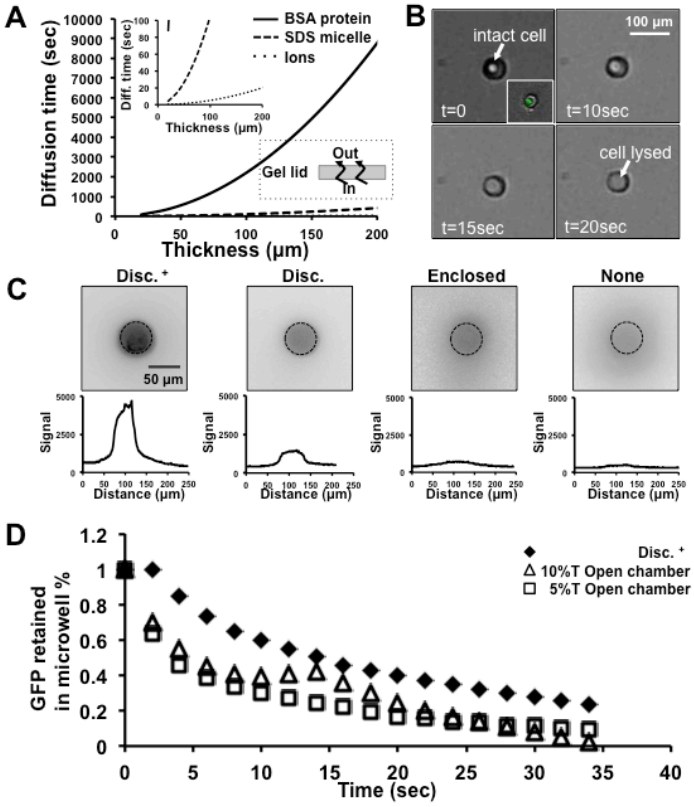

Figure 6.3 Open fluidic electrophoretic cytometry incorporating density-patterned PA gels designed to reduce analyte dispersion during cell lysis, sample injection, and

electrophoresis. (A) Time takes for molecules to diffuse through a certain thickness of agarose lid. The agarose lid allows penetration of lyses buffer content (small ions and SDS micelle) and prevents diffusive escape of proteins. (B) Single U251-GFP cells maintain viability when enclosed under agarose lid, and can be lysed after 30 s of lyses buffer application. (C) Representative epifluorescence micrographs and accompanying concentration profiles for *in-situ* single-cell lysis for four conditions: the open microwell, agarose lid on microwell, high-density PA gel sidewalls at microwell, and the combined lid and high-density PA gel sidewall conditions (microwell edges highlighted for clarity). Analyte distribution shown for an elapsed cell lysis time of 30 s. (D) ~30% of proteins are retained with patterned gel and agarose lid, after 30 s of U251-GFP cell lyses with GFP as the model protein, comparing to ~10% with uniform gel open chamber design.

6.4 Reduce Protein Losses during Lyses

Not only have we created a 20%T region in the photo-patterned gel to prevent planar protein loss during lyses, we have also implemented an ultra-thin agarose layer on top of PA gel to encapsulate captured single-cells in microwells (Appendix J). The agarose layer serves as a selective filter, allowing small ions and SDS micelle to diffuse through for cell lyses, while preventing proteins to diffuse out. Calculations of the diffuse time of the above molecules through 2% agarose is shown in Figure 6.3A [42, 43]. Cells are intact with agarose application under bright-field examination and calcium AM staining (Figure 6.3A). After applying 200 µL lyses buffer on top of agarose layer, we observed that cells are lysed in the microwells and proteins are released.

The planar diffusion loss as well as vertical loss out of microwell is severe with the uniform gel and open chamber configuration, especially for smaller proteins. We observed GFP diffusion after 30 s of lyses of U251-GFP cells at four conditions: using open microwell with 8% uniform gel, using agarose lid on microwell with 8% uniform gel, using open microwell with high-density PA gel sidewalls, and the combined lid and high-density PA gel sidewall condition (Figure 6.3B). With open microwell and uniform gel condition, a 90% loss can be observed with GFP as model protein. However, with patterned gel only, the loss can be reduced to 70%. Combining the high-density sidewalls and the agarose lid, protein loss was more reduced. We have also imaged GFP fluorescence over the course of lyses of 30 sec (Figure 6.3C), and compared the total fluorescence in microwell with controls. The controls were conducted with homogeneous 5%T and 10%T gels without agarose layer. Lyses buffer was poured into a lyses chamber, where the open microwell patterned PA gel was placed on the bottom. It is shown that >30% of total GFP fluorescence was retained after 30 sec of lyses compared with the 10-15% with the homogeneous gels in open chamber format. It is worth noting that there is still a very thin layer of liquid (25~40 µm, unpublished data) in between the PA gel and the agarose layer. The agarose layer cannot completely seal the device to 100% prevent diffusive loss of proteins. However, this layer has reduced diffusive loss and prevented convective loss during pouring of lyses buffer.

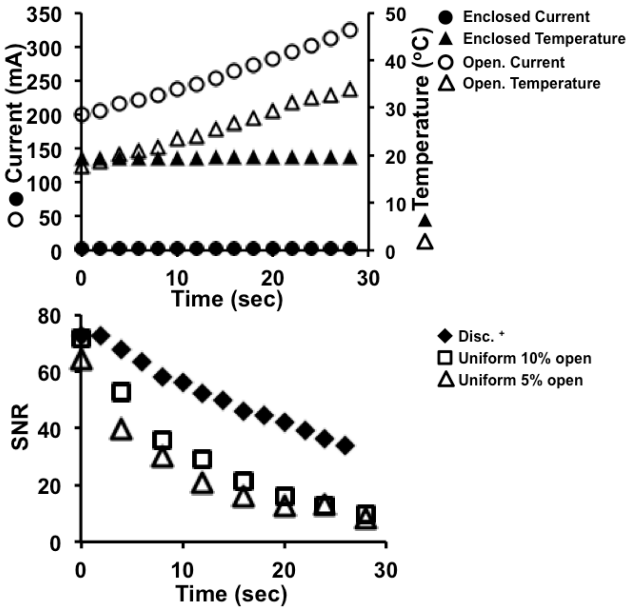

Figure 6.4 Altering the geometry of the open fluidic system reduces Joule heating during *scPAGE*. (A) Measured local temperature and electrical current during *sc*PAGE in an open and enclosed cytometry device (t_{PAGE}=35 s, E=50 V/cm). (B) SNR measured for PAGE of OVA in an open chamber and the Disc.$^{+}$ format (c_{OVA}=*0.5* μM*,* E=50 V/cm).

6.5 Enclosed Electrophoresis Device Reduces Joule Heating

During separation following cell lyses, protein spots experience diffusion both on the planar directions and the vertical direction. The planar diffusion causes peak broadening, which detriments separation resolution and the detection sensitivity. The vertical diffusion brings protein material out of the thin PA gel into the surrounding buffer, which severs the sensitivity even more. The fundamental approach to improve performance is to constrain Joule heating [44-47]. Analyzing Joule heating generation equations and heat dissipation equations, we have concluded three aspects of approaches to reduce temperature elevation during electrophoresis (Appendix K):

1. Limiting mass heat generation by reducing device cross sectional area and allow lower voltage application to generate the same amount of electric field. 45 times smaller cross sectional area was accomplished with enclosed device setting, and a 3 times lower voltage is needed to generate the same amount of electric field. Over all, a 112 times reduction of Joule heating amount was achieved (Appendix K).

2. Using favorable heat dissipation geometry by decreasing the heat dissipation distance (thickness of device) and increasing surface-to-volume ratio. ~2.6 times smaller thermal resistivity was achieved with enclosed device (Appendix K).

3. Applying thermal effective material to act as heat sink. In enclosed device, > 90% of the volume is thermal conductive glass slide and only <10% is hydrogel that participate in electrophoretical heat generation.

To validate the temperature controlling property of the enclosed device comparing to the open chamber device, we measured the temperature in the system using an IR sensor above the electrophoresis chamber (Figure 6.4A). We observed a linear increase over a 35 s electrophoresis (50 V/cm) with a slope of 0.418 ± 0.016 °C/s (n=3) for open chamber device and a 0.01 ± 0.0002 °C/s (n=3) for enclosed device. On the other hand, the conductivity of buffer will also increase due to temperature increase (conductivity is expected to increase by 1.9% per degree of increase in the buffer temperature, operating around room temperature) This was seen in the open chamber device as shown in Figure 6.4A, whereas the conductivity was kept low and constant in the enclosed device. It should be noted that the temperature measurement using IR sensor was targeting the surface temperature of both devices, not necessarily the local temperature in the gel. A more localized indicator of the temperature effect is the protein diffusivity and mobility. In our previous studies [19, 20], an increase of protein electrophoretic mobility was observed with a homogenous PA gel instead of a constant mobility based on theory. We attribute this to the temperature increase due to severe Joule heating during electrophoresis. Joule heating raises the local temperature, lowering the local viscosity [48, 49] and, thus, increasing the apparent electrophoretic mobility of all proteins [50]. This is also observed here with the open chamber device for the proteins tested (Appendix Figure A14).

The immediate advantage of having a low heating device is that it improved the detection sensitivity by reducing protein loss out of gel and limiting peak dispersion. Analyzing the signal-to-noise ratio (SNR) of OVA in enclosed and open chamber devices (Figure 6.4B), we see that SNR decreases in all conditions over the separation period. However, SNR of the enclosed device shows a slower decrease comparing to the open chamber device. This results in ~3 times higher SNR at the end of a 30 sec separation period. Potentially, this can improve the detectability of low abundance proteins from single-cells.

Another benefit of controlling Joule heating is that higher voltage/ electric field can be used without causing temperature increase. Appendix Figure A14 demonstrates the possibility of using very high electric field in the enclosed device without causing obvious temperature increase, comparing with the open chamber device. A higher electric field can bring a separation from heavily diffusion-controlled regime to less diffusion controlled or convective/ other mechanism controlled. This can free us from diffusion and give us more leverage on improving other device design parameters to influence separation.

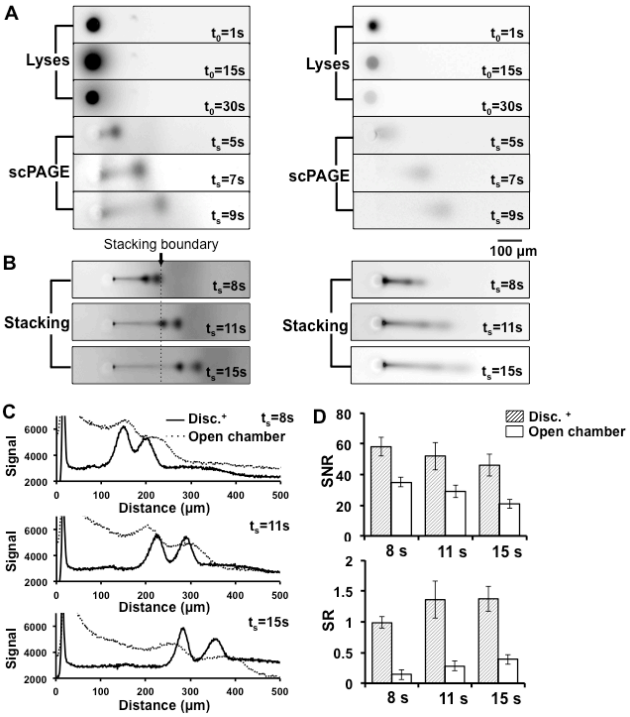

Figure 6.5 Dispersion control improves separation resolution and detection sensitivity of *sc*PAGE. (A) Inverted grayscale epifluorescence micrographs of in-situ U251-GFP cell lysis and subsequent electrophoresis of GFP in a dispersion-control device and an open fluidic device. (B) Inverted grayscale epifluorescence micrographs of the stacking process of BSA and OVA in the Disc.$^+$ device, comparing with them in uniform 10%T gel in open chambers (*E*=50 V/cm). (C) Representative graphs of fluorescence intensity along separation path of (B) with dispersion-controlled Disc.$^+$ device and open chamber device compared. (D) SNR and SR of the separation performed in (B) compared.

6.6 Advanced Separation Performance with Disc.$^+$

From the reduced Joule heating-caused temperature increase and photopatterned discontinuous PA gel, we can achieve higher signal, less diffusion both during cell lyses and protein separation. Figure 6.5A shows the time-lapse images of a GFP labeled U251 cell in microwell during lyses and PAGE. The GFP fluorescence is greatly retained during the 30 s of lyses, and the GFP peak is more clearly seen, less dispersed during separation.

To visualize the separation process, especially the stacking phenomenon, we used two fluorescent-tagged proteins BSA and OVA (Figure 6.5B) for separation. It is clearly seen that the peak dispersion is severe in open chamber device due to elevated temperature and no-stacking design, whereas clean, separated peaks are observed with enclosed device and discontinuous gel (Disc.$^+$). Figure 6.5C also depicts the fluorescence plot of BSA and OVA separation under two conditions at three time points approaching, during and after stacking. We can see that the Disc.$^+$ setting resulted in clear baseline separation whereas the open chamber device appears to have severe peak overlap and peak tailing due to

poor injection.

One fundamental indicator of the dispersion reduction because of the stacking gel is the change in protein diffusion coefficient in the course of separation. We extracted the apparent diffusion coefficient (D_i') from OVA electrophoresis. It is called the apparent coefficient because it is calculated based on the apparent peak variance without accounting for other forces that affect peak dispersion, such as the peak stacking effect with photo-patterned gel. We observed a maintained diffusion rate in enclosed device due to constant temperature and an increased diffusion in open chamber device. We can also pinpoint the stacking gel boundary from the initial decrease and the negative value of D_i' at the boundary (Appendix Figure A14). We also plotted the peak variance progression over the separation time (Appendix Figure A15). The peak variances of OVA in enclosed device decreases at the stacking gel region. This resulted in even narrower peaks than the initial injection at the end of stacking. This helps to counteract the injection dispersion.

Figure 6.5D shows two aspects of separation performance: separation resolution (SR) and detection sensitivity (SNR). We can achieve a 2~3 fold improvement in separation resolution with Disc.$^{+}$ device comparing with open chamber setting and a 2 fold increase in signal-to-noise ratio. The open chamber device causes ~70% protein loss during 30 sec electrophoresis due to Joule heating temperature increase, whereas the enclosed device only caused 30%~ 60% protein loss depending on the protein size. Overall, we have achieved better separation performances in enclosed device than in the open chamber device, evaluated by both separation resolution and detection sensitivity.

6.7 Conclusions

Here we have described three aspects of innovation to improve the separation resolution and detection sensitivity of single-cell PAGE (scPAGE) by tackling diffusion. We photo-patterned PA gels of discontinuous pore sizes. The PA gel consists of microwells with high gel-density sidewalls and a low gel-density protein-stacking region. We also applied a selective permeable thin agarose gel layer on the top of cell-trapped separation gel. This hydrogel lid allows chemical lyses via reagent diffusion as well as prevents protein loss. We have also designed a heat-minimized microfluidic scPAGE configuration. This device minimized temperature increase during high voltage application, which prevents heat-induced peak dispersion.

As a result, we have improved the protein retaining rate for 3-fold during cell lyses. On the other hand, the diffusion loss of various proteins during electrophoresis was significantly lowered from 70% to 30%~60% as well. The final signal-to-noise ratio was 2 fold higher than the original configuration. With the stacking gel, we have achieved an even narrower injection band than the initial injection after stacking, and the separation resolution was improved from the previous SR=0.5 to SR=1.5. This scPAGE configuration can drastically improve the specificity of

protein measurement and expand our reach to low abundance proteins in single-cells.

References

[1] Hanahan, D., Weinberg, R. A., Cell, 2011, 144, 646-674.
[2] Wei, W., Shin, Y. S., Ma, C., Wang, J., Elitas, M., Fan, R., Heath, J. R. Genome Med., 2013, 5, 75-88.
[3] Schulz, K.R., Danna, E.A., Krutzik, P.O., Nolan, G.P., Curr. Protoc. Immunol., 2012, 96, 8.17.1-8.17.20.
[4] Stack, E. C., Wang, C., Roman, K. A., Hoyt, C. C., Methods, 2014, 70, 46-58.
[5] Perfetto, S. P., Chattopadhyay, P. K., Roederer, M., Nat. Rev. Immunol., 2004, 4, 648-655.
[6] Bandura, D. R., Baranov, V. I., Ornatsky, O. I., Antonov, A., Kinach, R., Lou, X., Pavlov, S., Vorobiev, S., Dick, J. E., Tanner, S. D., Anal. Chem., 2009, 81, 6813-6822.
[7] Mellors, J. S., Jorabchi, K., Smith, L. M., Ramsey, J. M., Anal. Chem., 2010, 82, 967-973.
[8] Stadler, C., Rexhepaj, E., Singan, V. R., Murphy, R. F., Pepperkok, R., Uhlen, M., Simpson, J. C., Lundberg, E., Nat. Methods, 2013, 10, 315-323.
[9] Maecker, H. T., Trotter, J., Cytometry Part A, 2006, 69A, 1037-1042.
[10] Laemmli, U. K., Nature, 1970, 227, 680–685.
[11] Towbin, H., Staehelin, T., Gordon, J., Proc Natl Acad Sci USA, 1979, 76, 4350–4354.
[12] Kurien, B. T., Scofield, R. H. Protein Blotting and Detection: Methods and Protocols, Springer: New York, 2009.
[13] Burnette, W. N., Anal. Biochem., 1981, 112, 195-203.
[14] Jin, S., Anderson, G. J., Kennedy, R. T., Anal. Chem., 2013, 85, 6073-6079.
[15] Hughes, A. J., Lin, R. K., Peehl, D. M., Herr, A. E., Proc. Natl. Acad. Sci. U.S.A., 2012, 109, 5972−5977.
[16] Hughes, A. J., Herr, A. E., Proc. Natl. Acad. Sci. U.S.A., 2012, 109, 21450-21455.
[17] Hughes, A. J., Spelke, D. P., Xu, Z., Kang, C. C., Schaffer, D. V., Herr, A. E., Nat. Methods, 2014, 11, 749−755.
[18] Duncombe, T. A., Kang, C. C., Maity, S., Ward, T. M., Pegram, M. D., Murthy, N., Herr, A. E., Adv. Mater., 2016, 28, 327-334.
[19] Kang, C. C., Lin, J. M. G., Xu, Z. C., Kumar, S., Herr, A. E., Anal. Chem., 2014, 86, 10429−10436.
[20] Shahi, P., Kim, S. C., Haliburton, J. R., Gartner, Z. J., Abate, A. R., Scientific Reports, 2017, 7, 44447.
[21] Li, X. T., Zhao, S. L., Hu, H. K., Liu, Y. M., Journal of Chromatography A, 2016, 1451, 156-163.
[22] Carlo, D. D., Jeong, K., Lee, L. P., Lab on a Chip, 2003, 3, 287-291.
[23] Lai, H. H., Quinto-Su, P. A., Sims, C. E., Bachman, M., Li, G. P., Venugopalan, V., Allbritton, N. L., J R Soc Interface, 2008, 5, S113–S121.

[24] Shi, Q. H., Qin, L. D., Wei W., Geng, F., Fan, R., Shin, Y. S., Guo, D. L., Hood, L., Mischel, P. S., Heath, J. R., Proc. Natl. Acad. Sci. U.S.A., 2012, 109, 419–424.
[25] Hargis, A. D., Alarie, J. P., Ramsey, J. M., Electrophoresis, 2011, 32, 3172–3179.
[26] Ma, C., Fan, R., Ahmad, H., Shi, Q., Comin-Anduix, B., Chodon, T., Koya, R. C., Liu, C. C., Kwong, G. A., Radu, C. G., Ribas, A., Heath, J. R., Nat. Med., 2011, 17, 738–743.
[27] Plenert, M. L., Shear, J. B., Proc. Natl. Acad. Sci. U.S.A., 2003, 100, 3853–3857.
[28] Serwer, P., Electrophoresis, 1983, 4, 375–382.
[29] Brody, J. R., Kern, S. E., Anal. Biochem., 2004, 333, 1–13.
[30] Stellwagen, N. C., Electrophoresis, 2009, 30, S188–195.
[31] Kozulić, B., Anal. Biochem., 1994, 216, 253–261.
[32] Clifton, M. J., Electrophoresis, 1993, 14, 1284-1291.
[33] Dobry, R., Finn, R. K., Science, 1958, 127, 697-698.
[34] Probstein, R., Physicochemical Hydrodynamics: An Introduction, Wiley: New York, 1991.
[35] Zarei, M., Goharshadi, E. K., Ahmadzadeh H., Samiee, S., RSC Adv., 2015, 5, 88655–88665.
[36] Rosenfeld, T., Bercovici, M., Lab on a Chip, 2014, 14, 4465–4474.
[37] Nickolaj J. P., Rikke P. H. N., Mogensen, K. B., Kutter, J. P., Electrophoresis, 2004, 25, 253–269.
[38] Nelson, R. J., Paulus, A., Cohen, A. S., Guttman, A., Karger, B. L., J. Chromatogr., 1989, 480, 111–127.
[39] Wang, W., Zhang, M. J., Xie, R., Ju, X. J., Yang, C., Mou, C. L., Weitz, D. A., Chu, L. Y., Angew. Chem. Int. Ed., 2013, 52, 8084-8087.
[40] Buxboim, A., Rajagopal, K., Brown, A. E., Discher, D. E., J. Phys.-Condens. Mat., 2010, 22, 194116.
[41] Gelfi, C., Alloni, A., De Besi, P., Righetti. P. G., J. Chromatogr. A, 1992, 608, 343-348.
[42] Musnicki, W. J., Lloyd, N. W., Phillips, R. J., Dungan, S. R., Journal of Colloid and Interface Science, 2011, 356, 165–175.
[43] Tong, J., Anderson, J. L., Biophysical Journal, 1996, 70, 1505-1513.
[44] Jansson, M., Emmer, A., Roeraade, J., HRC J. High Resolut. Chromatogr., 1989, 12, 797–807.
[45] Ermakov, S. V., Jacobson, S. C., Ramsey, J. M., Anal. Chem., 1998, 70, 4494–4504.
[46] Swinney, K., Bornhop, D. J., Electrophoresis, 2002, 23, 613– 620.
[47] Erickson, D., Sinton, D., Li, D., Lab on a Chip, 2003, 3, 141–149.
[48] Knox, J. H., McCormack, K. A., Chromatographia, 1994, 38, 207–214.
[49] Weast, R., CRC Handbook of Chemistry and Physics, Student Edition, CRC Press: Boca Raton, 1987.
[50] Knox, J. H., Grant, I. H., Chromatographia, 1987, 24, 135-143.

Appendix

A. High Resolution Photolithography for Single-cell Co-culture Device (Chapter 3)

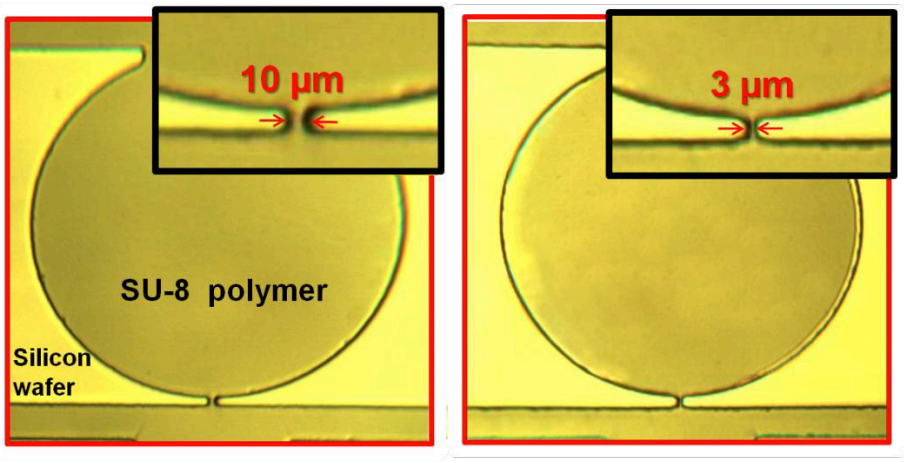

Figure A1. Obtain Smaller Microstructure with Oxygen Plasma. A thin layer of SU-8 photoresist was spin-coated on silicon wafer. Then the wafer was put under UV light exposure with Mylar mask on top. SU-8 of the circle area, including the trapping junction polymerized. After developing, a 10um wide junction structure was made (left picture, "Before" oxygen plasma). The wafer was subjected to oxygen plasma to further etch the edge of the SU-8 structure, creating a 3 um wide junction as a result (right picture, "After" oxygen plasma).

High resolution photolithography is required to achieve the 3 μm trapping gap, which usually demands for more sophisticated masks such as Chrome mask. Here we have developed a cost effective way to reach lower dimension with only Mylar mask using oxygen plasma etching. After photolithography, the width of gap was 10 μm as provided with the Mylar mask. Then the wafer was exposed to oxygen plasma for 3 mins at 0.12 Torr oxygen pressure and 120 Walt power level followed by 5 mins at 0.5 Torr oxygen pressure and 40 Walt power level, repeating twice. The chemical reactions between reactive oxygen and SU-8 polymer generated decomposed versatile species from surface. Then, the versatile species could be taken away from the surface by vacuuming. The repeated different plasma energy level was used in order to achieve fine trimmed edges: higher energy level effectively etched the surface and lower energy level gave even, smoother edge. In this way, 3 μm gap structures were made.

B. Single-cell Co-culture Chip Preparation and Cell Trapping (Chapter 3)

Before use, the microfluidic chip was autoclaved for 25 mins. Then, the chip was placed in vacuum chamber for 15 mins and the culture media was immediately

dropped on top of the inlets in order to fill the chip. The chip was incubated in cell culture incubator for 3 hours before cell loading to prepare a protein absorbed surface to help cell attachment. To avoid possible debris from culture media and cell suspension that would be trapped at the gap, the media was filtered with 0.45 μm Nylon membrane every time before use; the prepared cell suspension was stood in culture incubator for 5 mins to precipitate debris before loading.

A PDMS gasket with a length of 2.5 cm, a width of 4 mm and a height of 5 mm was manually cut to fit the 8 cell loading inlets area, and was attached to the top of the chip. The microfluidic chip was perfused with culture media for at least 10 mins at a withdrawing flow speed of 5 μL /min before cell loading. Then cells were dropped into the gasket and were uniformly distributed by gentle pippeting Fluid was driven by withdrawing through the outlet c, at a constant speed with a syringe pump (PHD 2000, Harvard Apparatus) interfaced to the Luer ports via Tygon tubing (ID 1.3 mm) . During cell loading, the chip was observed under the microscope, and was placed on a hot plate with a temperature of 37 °C. After loading, gasket was removed from the top and the chip surface was cleaned with media. The residue cells in the loading channels were washed away by pumping media through perfusion inlet a1 and a2 at the speed of 2 μL/min for less than 5 mins. The whole process of loading was done within 5 mins.

After the first cell type was trapped as single cell, the chip was placed in cell culture incubator for 5 hours before the second cell type trapping. After second cell trapping, the chip was put into incubator for static culture for 4 hours. Then inlets b1-b8 were blocked by attaching a thin layer of PDMS membrane on top. Media was loaded from inlets a1 and a2 through the gradient generator, by withdrawing through outlet c with a constant speed.

C. Single-cell Pairs Trapping Parameter Optimization (Chapter 3)

The efficient cell trapping requires the balance of several key parameters, such as cell density, flow speed and loading time. High cell density enables shorter time of trapping, which might be beneficial for the cells to experience less time of stress, yet could also cause clogging of cells or multiple cell trapping. After optimization, a density of 2.0 ×105 cells/mL was used to achieve the highest single cell trapping efficiency and prevent clogging of multiple cells. Higher speed of loading results in faster trapping, yet the viability of trapped cells could be severely damaged due to the shear stress. Lower loading speed results in higher trapping efficiency, yet the clogging and attachment of cells could cause extra cell trapping and the difficulties during washing step. We have optimized the loading speed for the best balance of single cell trapping efficiency and cell viability. We used the flow speed of 0.8 μL/min after dropping the cells. At the same time, the loading period should be kept as short as possible within the requirement of trapping efficiency. In our case, the trapping duration was kept less than 5 mins.

The static culture after loading is essential for the attachment and spreading of cells for their healthy growth. It provided the condition for the cells to prepare the

sufficient extracellular matrix (ECM) concentration around cell and helped the cells to anchor to the surface easily. We optimized the static culture time as no more than 4 hours and no less than 2.5 hours. After cells completely attached to the bottom of the chip, continuous perfusion culture was started.

We found that the migration distance of fibroblast can be controlled by different ECM coating density. In order for fibroblast cells to attach to the culture surface, the chip was incubated with culture media for certain time period to make the glass surface hydrophilic. Because fibroblasts have high ability to secrete their own ECM, this extent of surface treatment was found enough to support them anchoring the surface and spreading out. (For other cell lines, which has less ability to secrete their own ECM, long time coating with certain type of ECM was normally necessary). We have tried different period of media incubation from 10 mins to 4 hours. With 4 hours of coating, fibroblast cells easily anchored the surface even during loading process. Thus it was difficult to wash out the extra cells. With 10 mins of coating, fibroblast cells can be easily loaded and the extra cells can be washed out, yet it took more than 5 hours for them to become the healthy spreading state. The coating time also affects the fibroblast migration. Before loading the second type of cells, with 10mins of coating, fibroblasts migrated only about 10 μm away from the gap; with 30 mins of coating, they could migrate about 50 μm away from the gap, which gave enough space for the second cell trapping. Thus, we used 30 mins of media incubation to support fibroblast migration.

D. Single-cell Co-culture Condition Optimization (Chapter 3)

The perfusion culture flow rate was balanced between media refreshment, secretion pattern formation and shear stress. We have tested different flow rate for cell culture. It was shown that in the range of 0.1 μL/min to 1 μL/min, a range of cell types are able to grow with sufficient viability from upstream to downstream. Yet in order to ensure the best culture condition for more valid observation, we have calculated the media supply rate and shear stress upon cells in the upstream and downstream (Figure A3). Using simulation of the media distribution under a flow rate, we analyzed the media replacement of the 1st chamber and the 42th (the last) chamber after the same time of media supply (20 seconds).

Generally speaking, the media replacement depends on two factors, the flow rate and diffusion rate. If the flow rate is too low (e.g. 0.1 μL/min), dilution of new media from diffusion can diminish the media replacement speed; if the flow rate is high (e.g. 1 μL/min), there is not enough time for the new media to exchange in the chamber; at a certain flow rate (0.2 μL/min), diffusion and laminar flow balances to give the best media replacement efficiency. We also calculated the shear stress to cells in the culture chamber verses flow rate. The shear stress upon cells in this platform is generally small. At the flow speed of 0.2 μL/min at the withdrawing outlet c (0.025 μL/min in each of the 8 units), shear stress is calculated to be about 0.013 Dyne/cm2, which are minimized as to not influence the cell viability. Therefore, we have chosen 0.2 μL/min as the culture flow speed.

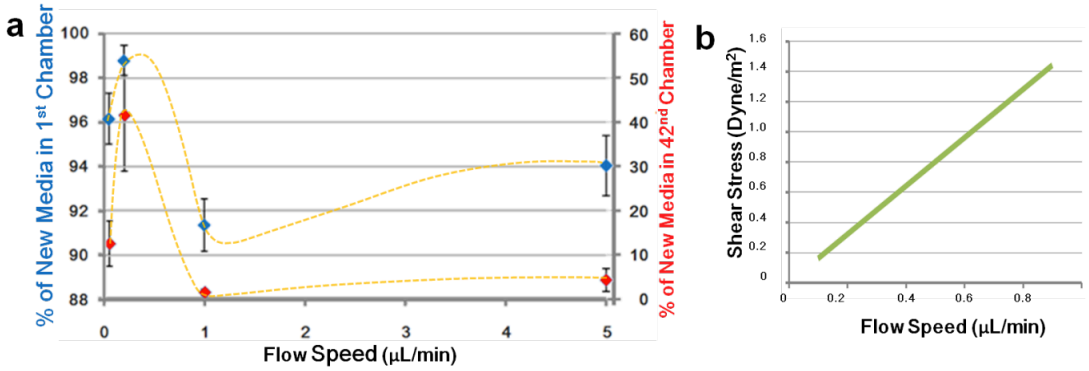

Figure A2. Calculation of the media refreshing efficiency of the first and last chamber along one wave-shaped channel (a). The blue data points are the percentage of new media supplied in the first chamber at different flow rate. The red data points are that of the last chamber. The flow speed on the X axis is the overall flow speed at the withdraw outlet, which supplies the media flow in all of the 8 units on the chip. For each unit (one of the 8 wave-shaped channels), the flow speed is one eighth of the overall speed. At optimized flow speed (0.2 μL/min), the media refreshing could achieve its maximum efficiency with a percentage of more than 96% new media even in the last chamber. (b) Shear stress upon cells cultured in the chamber at different flow speed of one unit. With the speed of 0.2 μL/min at the withdraw outlet, the flow speed of one unit is 0.025 μL/, shear stress is 0.013 Dyne/cm^2.

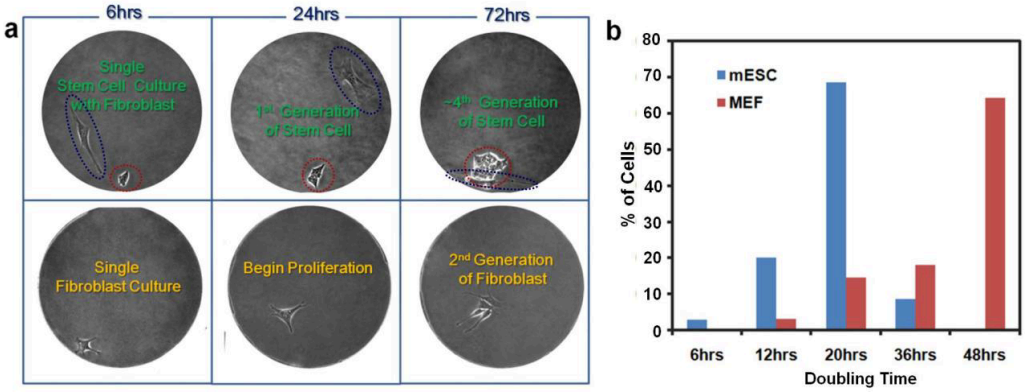

Figure A3. Long term culture of MEFs and mESCs for several generations. (a) The upper row of pictures show single-cell MEF and mESC coculture. Dotted circle in dark blue indicates MEFs and dotted circle in red indicates mESCs. During coculture for 3 days, mESC readily proliferated into colonies, and MEF maintained low proliferation rate. The lower row shows single-cell MEF been cultured alone. (b) Doubling time of mESC been cultured with MEF (blue bars) and MEF been cultured alone (red bars). The percentage of cells having a doubling time from 6 hours to 48 hours has been calculated from the collected well images. Most of mESCs have a doubling time of 20 hours and MEFs have a doubling time of 48 hours or longer.

With this optimized culture condition, we have tracked the growth of MEF and mESC single-cell pairs as well as single MEF (Figure A4). For 3 days of observation, the co-cultured MEF and mESC showed consistent proliferation for up to 4th generation. mESC was able to grow into big colonies with similar morphology as that of traditional dish culture. MEF, on the other hand, while

proliferation rate being reduced in co-culture, kept its high mobility and viability. In the case of MEF single cell culture, it proliferated with a similar speed as reported in the literature. This result shows the ability of this device to provide reliable long-term single cell culture information.

E. Amount of Magnetic Microbeads Does Not Interfere with Final MiRNA Amplified Signal (Chapter 4)

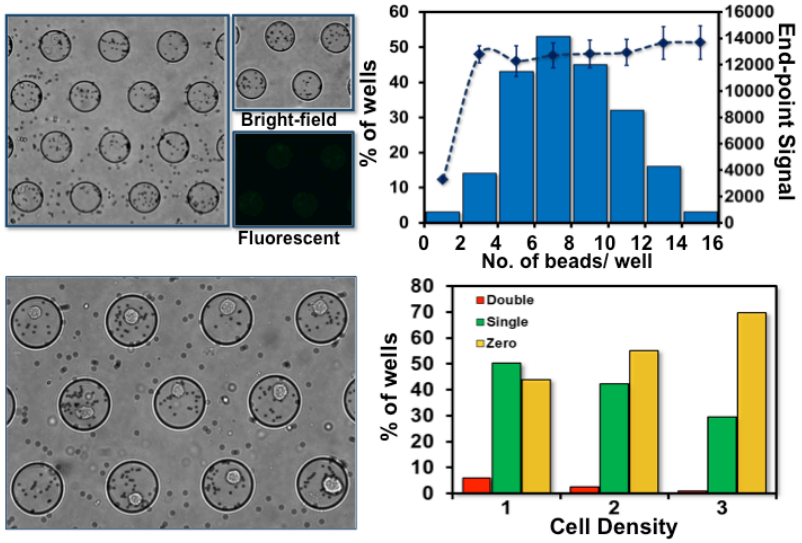

Figure A4. Number of beads in microwells does not influence end-point signal, and the optimization of single-cell trapping. Single-cell trapping efficiency is also optimized based on cell density. The cell densities for 1, 2 and 3 cases are: 0.5 x 10^{-6} cell/mL, 1.0 x 10^{-6} cell/mL and 1.5 x 10^{-6} cell/mL.

In single-cell miRNA detection, we need to confirm that trapped bead signal does not interfere with the final fluorescent signal from miRNA amplification (Chapter 3). We cannot control the number of magnetic beads trapped into each microwell, however, the binding sites on each bead is sufficient to capture all targeting miRNAs. We loaded the same concentrations of miRNA onto the chip, and measured the amplification signal. The final miRNA signal was constant throughout microwells with different numbers of beads (Figure A5). We have also optimized the single-cell trapping efficiency by analyzing the percentage of single-cell occupied microwells among all microwells under different cell densities. To get most efficient single-cell trapping, we used 0.5 x 10^{-6} cell/mL density.

F. MiRNA Amplification Kinetics (Chapter 4)

MiRNA hybridization to primary primer rate increases and reaches a plateau when all miRNAs are hybridized onto primers. The hybridization rate of B' to secondary primer increases rapidly at the beginning due to the produce of B', but decreases afterwards when the reaction became primer-controlled. The polymerase reaction rate increases due to the increased available sites on

double-stranded materials, but decreases afterwards due to depletion of dNTPs. The nicking enzyme rate increases over time due to the consistent supply of B' that can bind to secondary primer, but slows down due to decreased hybridization rate of B' to secondary primer. Combining all three types of reaction, we can also analytically predict the overall reaction rate to mimic the signal generation in the real reactions.

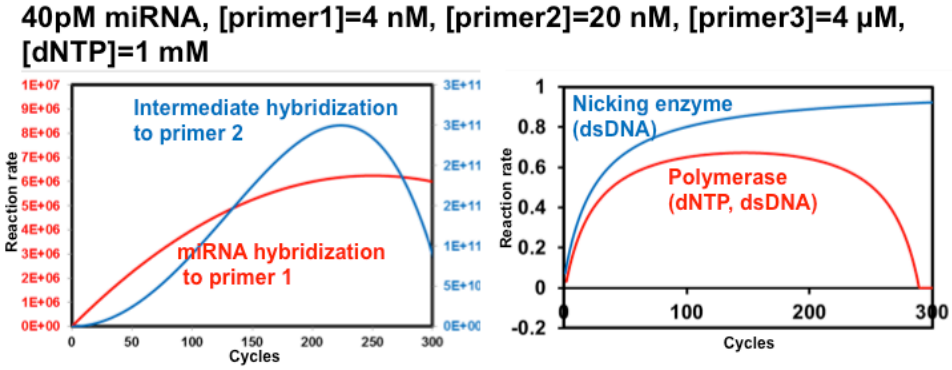

Figure A5. Analytical prediction of reaction rate for N_2 amplification: Analytical simulation for amplification mixture component reaction rate over time. Nicking enzyme keeps sufficient reaction rate over time whereas the polymerase in PCR reaction drastically decreases efficiency.

G. Temperature-controlled Electrophoretic Cytometry Device (Chapter 5)

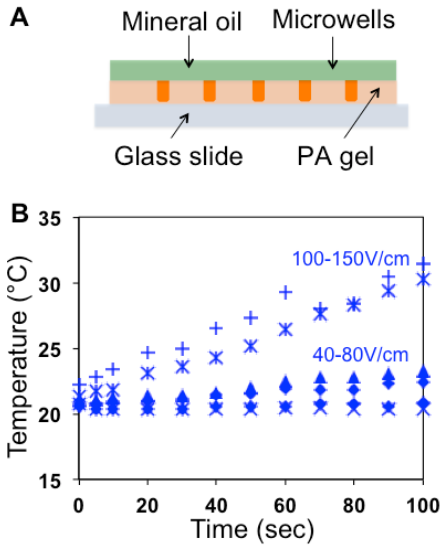

Figure A6. Temperature controlled device design (A) and time lapsed temperature profile of device when increased electric field is applied (B).

H. Predict Injected Sample Geometries (Chapter 5)

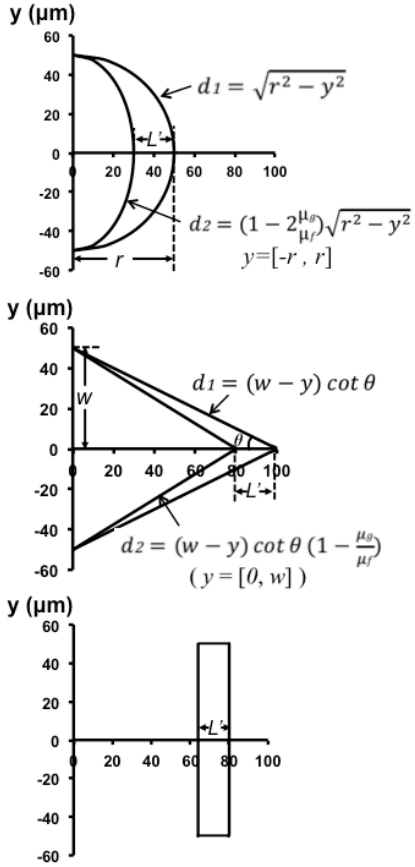

Figure A7. Geometrical illustration of peak shape after injection. The characteristic length of axial diffusion is *L'*, which can be derived from d_1 and d_2 equations.

Although the injected sample shape is greatly affected by the injector shape, it will not completely inherit the injector shape due to sample's electrophoretic mobility differences in the injector and in the gel. For different shapes of injector, we can describe the front and tail curvature of injected sample shape (d_1 and d_2) as follows.

For circular injector:

$$d1 = \sqrt{r^2 - y^2} \tag{1}$$

$$d2 = (1 - 2\frac{\mu g}{\mu f})\sqrt{r^2 - y^2} \quad (\ y = [-r, r]\ ) \tag{2}$$

Where μg and μf are the electrophoretic mobility of sample molecules in gel and in the injector, respectively; r is the radius of circular injector; and y-axis is perpendicular to the separation direction.

For triangular injector:

$$d1 = (w - y)\cot\theta \tag{3}$$

$$d2 = (w - y)\cot\theta\,(1 - \frac{\mu g}{\mu f}) \quad (\ y = [0,\ w]\ ) \tag{4}$$

Where θ is half of the vertex angle in an isosceles triangle, and *w* is half of the base length of isosceles triangle.

Due to the slower mobility of sample molecules in gel, the sample peak are stacked by a factor of $\frac{\mu g}{\mu f}$. Therefore, depending on the shapes of injector, *L'* can be expressed as follows.

Triangular injector:

$$L' = \cot\theta\,\frac{\mu g}{\mu f} w \tag{5}$$

Circular injector:

$$L' = 2\,\frac{\mu g}{\mu f} r \tag{6}$$

Rectangle injector:

$$L' = w \tag{7}$$

In the case of rectangular shaped injector, there is no radial diffusion contributing to peak dispersion, axial diffusion is the only dominant force.

In conditions where radial and axial diffusion exists, Taylor-Aris dispersion equation [1-4] can describe the temporal and spatial development of the analyte band distribution. In our case, the peak analysis is not based on the cross-sectional averaged signal intensity profile, but is based on the signal intensity along the mid-line due to the nature of 2D CCD imaging. Therefore, Taylor-Aris dispersion equation is modified to fit in this condition. The concentration distribution with triangle shaped injector is:

$$c_t(x,t) = \frac{\partial c}{\partial t} = D_i \frac{\partial^2 c}{\partial x^2} + D_i \frac{\partial^2 c}{\partial y^2} \tag{8}$$

Where

$$y = \theta(x - x\frac{\mu g}{\mu f}) \tag{9}$$

The concentration distribution with circular shaped injector is:

$$c_c(x,t) = \frac{\partial c}{\partial t} = D_i \frac{\partial^2 c}{\partial x^2} + D_i \frac{\partial^2 c}{\partial y^2} \tag{10}$$

Where

$$y = (1 - 2\frac{\mu g}{\mu f})(r - \sqrt{r^2 - 0.25x^2}) \tag{11}$$

And the concentration distribution with rectangle shaped injector is:

$$c_c(x,t) = \frac{\partial c}{\partial t} = D_i \frac{\partial^2 c}{\partial x^2} \tag{12}$$

Where D_i is diffusion coefficient of analyte and *c* is the spatial and temporal concentration of analyte. Based on these equations, analytical solutions for the development of sample peaks can be derived.

I. Affecting Factors for Dispersion Regime (Chapter 5)

The geometrical factors *w* and $\frac{L'}{w}$, and the separation conditions *E* and $\frac{L}{E}$ affect peak variances among different injector shapes. In the below section, we will discuss how these factors affect the peak variance and separation efficiency.

1. Geometrical factors

Sizes of circular injectors, as well as shapes and sizes of triangular injectors affect how much radial diffusion contributes to total peak variance. As shown in Figure A9, when the characteristic length *w* (or radius *r*) of the circular injector increases from 50 μm to 300 μm, the plateau of radial diffusion caused peak variance (σ_r^2) increases. However, the slop of peak variance increase becomes smaller. This means that with smaller circular injectors, radial diffusion has more significant effect on peak variance at the beginning of separation, but quickly saturates, whereas with larger circular injectors, radial diffusion contributes to peak variance slowly but eventually result in a larger peak variance. For triangular injectors, when keeping the vertex angle consistent (Figure A9), we get the same peak variance increase rate with different injector sizes, whereas the radial diffusion caused peak variance reaches higher plateau when injector size is larger. The shape of isosceles triangular injectors also affects the peak variance development, as shown in Figure A9 (C). Increasing the vertex angle of the triangular injector drastically decreases the peak variance caused by radial diffusion. The extreme of this case is when θ=90^o, the triangular injector becomes rectangular injector.

Examining the combination of dimensionless variables-Peclet number and $\frac{L'}{w}$ is an effective way to determine dominant dispersion forces for a particular condition. Figure A9 (D), (E) and (F) shows the corresponding distribution of the above conditions in the dispersion regime plot. When keeping the shape ($\frac{L'}{w}$) consistent, whereas larger injector size brings the condition into higher *Pe* regime, where the initial injected sample shape is more dominant. Changing the shape of triangular injector by changing the vertex angle, we not only shift $\frac{L'}{w}$, but also shift the *Pe* axis. Larger vertex angle also brings the condition into injection shape dominant regime.

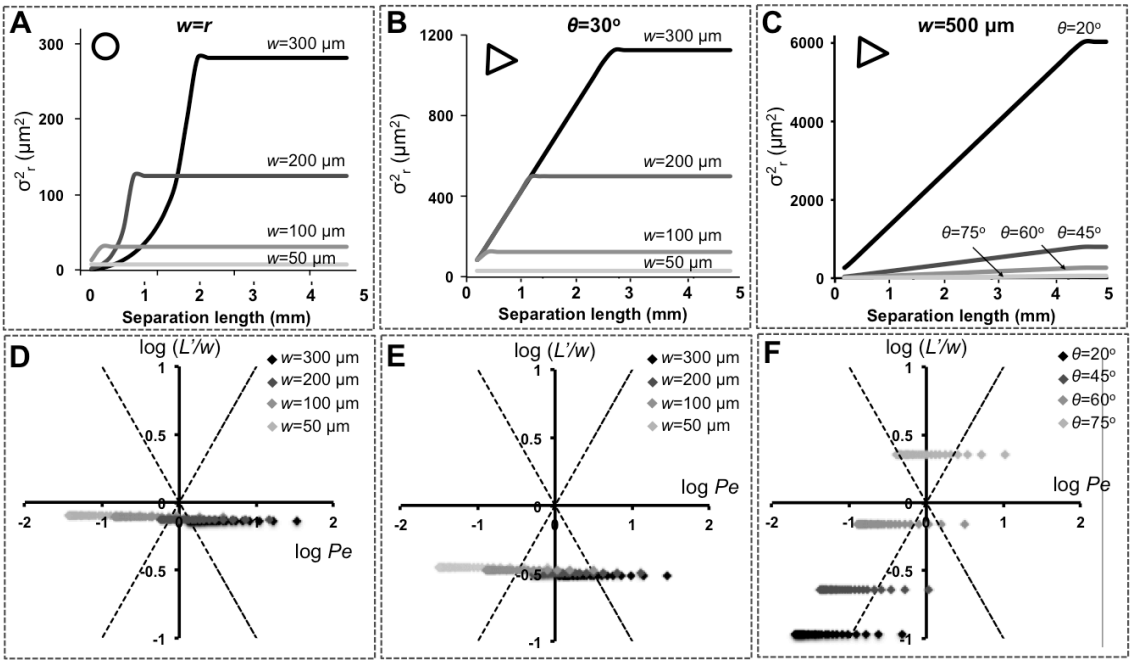

Figure A8. Peak variance progression and *log (Pe)* - *log (L'/w)* is affected by the characteristic length (*w*) and injected sample shapes. A) For circular injectors, when the characteristic length *w* (or radius *r*) increases, the plateau of radial diffusion caused peak variance (σ_r^2) increases. However, the slop of peak variance increase becomes smaller. B) For triangular injectors, when keeping the vertex angle consistent (θ=30°), we get the same peak variance increase rate with different injector sizes. However, the radial diffusion caused peak variance reaches higher plateau with larger injector sizes. C) Increasing the vertex angle of the triangular injector drastically decreases the peak variance caused by radial diffusion. D), E) and F) Corresponding distribution of the above conditions in the dispersion regime plot. When keeping the shape ($\frac{L'}{w}$) consistent, larger injector size brings the condition into higher *Pe* regime. Changing the shape of triangular injector by changing the vertex angle not only shift $\frac{L'}{w}$, but also shift the *Pe* axis.

2. Separation condition

Separation electric field used for separation and the length of separation also affects the dominant force for a particular separation. In general, increasing electric field is helpful in controlling the contribution of diffusion forces to peak variance. As shown in Figure A10 (A), (B) and (C), for all three shapes of injector, a higher electric field causes a slower increase in peak variance along a certain separation length, and a delay in reaching the plateau of radial diffusion. It is also worth noting that the plateau is not affected by separation conditions but is solely determined by the geometry of injector. In the same way, we can graph the corresponding distribution of the above conditions in the dispersion regime plot (Figure A10 (D), (E) and (F)). Keeping $\frac{L'}{w}$ consistent, increasing electric field only increases *Pe*, bringing the condition from diffusion dominant to injection shape dominant regimes.

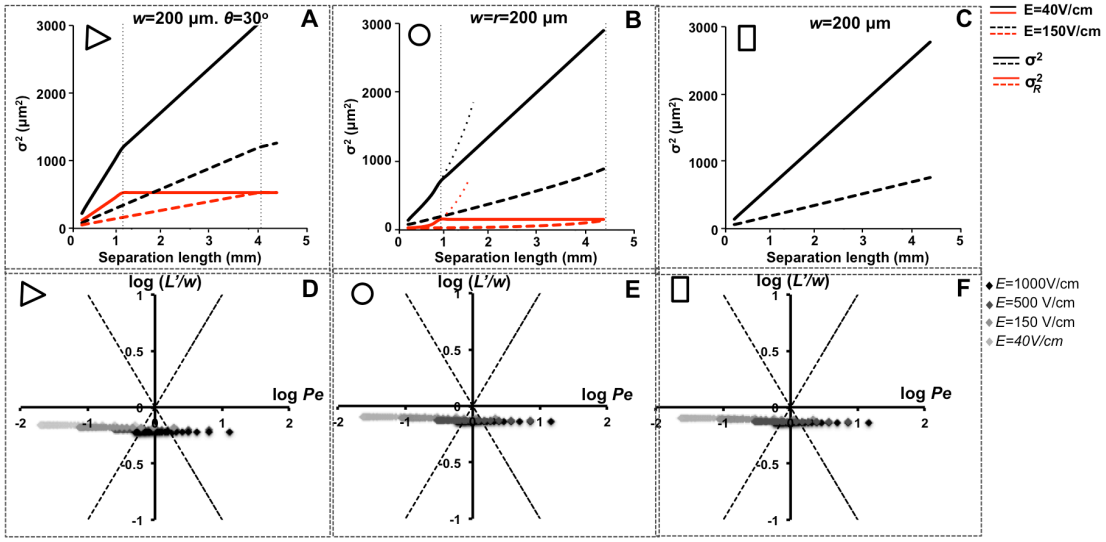

Figure A9. Peak variance progression and *log (Pe)* - *log (L'/w)* is also affected by the external factors such as electric field strength. A), B) and C) Peak variance progression at two electric field strength. The solid curves are analyzed with *E*= 40V/cm and the dashed curves are with *E*= 150V/cm. Black curves are the total peak variance and red curves are radial diffusion caused peak variance. For all three shapes of injector, a higher electric field causes a slower increase in peak variance and a delay in reaching the plateau of radial diffusion. D), E) and F) Corresponding distribution of the above conditions in the dispersion regime plot. Keeping $\frac{L\prime}{w}$ consistent, increasing electric field only increases *Pe*, bringing the condition from diffusion dominant to injection shape dominant regimes.

Furthermore, to confirm our prediction about the effect of electric field on injector shape influenced separation performance, we also conducted OVA-FITC and BSA-FITC separation on flat PA gel under two electric fields 40V/cm and 150V/cm, while setting the characteristic length *w*=100 µm. Figure 7A shows the comparison of experimental result with analytical prediction. It confirms that at higher electric field conditions, OVA-FITC peaks show higher peak variances for triangular injectors than rectangular or circular injectors, whereas in low electric field conditions, the peak variance among different shapes of injectors are less distinguishable. This confirms the conclusion in Figure 5, where using Peclet number and geometrical factor $\frac{L\prime}{w}$, one can predict the impact of injection shape on separation performances. Comparing the separation resolution (SR) among three shapes of injectors, we see that at low electric field condition, shapes distinguish considerably among three types of injectors at initial stages of separation, whereas in the later stage of separation, the peak resolution merges among different shapes. It confirms that at low *Pe*, injection shape does not affect separation resolution as significantly as in high *Pe* conditions.

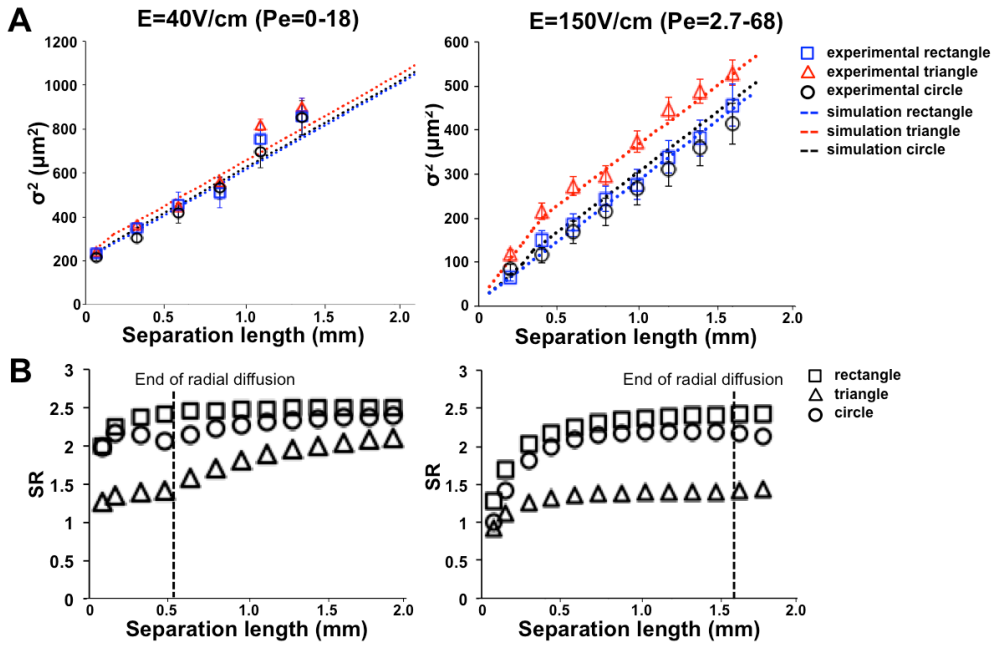

Figure A10. Compare the progression of peak variance and separation resolutions from three injector shapes at different electric fields. OVA-FITC and BSA-FITC were separated in PA gel under two electric fields 40V/cm and 150V/cm. The characteristic length of these injectors are all *w*=100 μm. A) Experimental result of OVA-FITC peak variances at two electric field strength matches with analytical prediction. At higher electric field conditions, peak variances are significantly higher for triangular injectors than rectangular or circular injectors, whereas in low electric field conditions, the peak variances of different injector shapes are less distinguishable. B) Compare separation resolution (SR) among three shapes of injectors. Similarly, at high electric field condition, triangular injectors gives poorer separation performance than other shapes, due to significant contribution of radial diffusion. At low electric field condition, shapes distinguish considerably among three types of injectors at initial stages of separation, whereas in the later stage of separation, the peak resolution merges among different shapes.

J. Configuration of Agarose Gel Lid (Chapter 6)

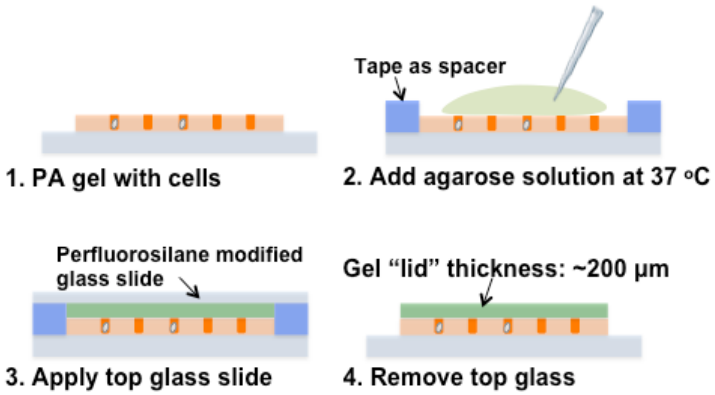

Figure A11. Procedure of making agarose gel lid before cell lyses.

We have implemented an ultra-thin agarose layer on top of PA gel to encapsulate captured single-cells in microwells (Figure A11). The agarose gel layer was cured in-situ after single-cell capture. Agarose needs to be dissolved with elevated temperature up to >75 ^{o}C in PBS buffer. To prevent heat shock to the cells, the precursor solution was cooled down to 37^{o}C before applying on top of PA gel. 0.5 mL dissolved agarose in PBS solution was pipetted on top of the cell-seeded PA gel slide. Afterwards, a glass slide was immediately applied on top of agarose to allow it to polymerize into a thin flat gel. The height of agarose gel layer was controlled by two spacers attached on the sides of PA gel. The glass slide can be removed by sliding off of one side after agarose gelation.

K. Joule Heating Reduction Methodology Rationale and Effect (Chapter 6)

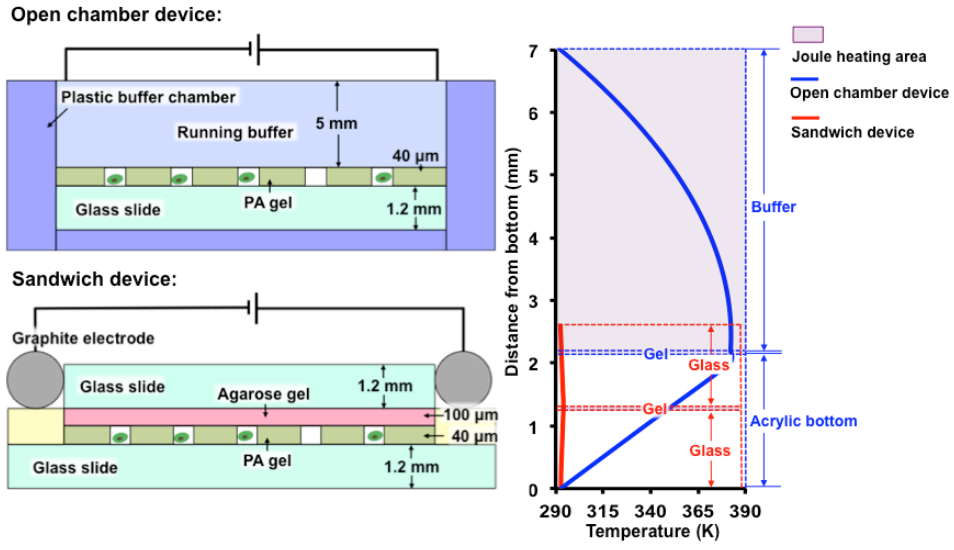

Figure A12. Enclosed device configuration and predicted temperature distribution at heat equilibrium. Red curve: enclosed device. Blue curve: open chamber device.

Several parameters control Joule heating in an electrophoresis circuit. The amount of heat generated (*Q*) due to a resistor of a length *L* and a cross sectional area *A*, with an elementary resistivity of γ, can be expressed as:

$$Q = \frac{U^2}{R} = U^2 \frac{A}{L} \frac{1}{\gamma} = E \cdot V \cdot A \frac{1}{\gamma} \quad (1)$$

Where *E* is the electric field applied, and *V* is the voltage. Depending on the geometry and material of the device, certain amount of heat is also dissipated throughout electrophoresis, acting to reduce Joule heating effect. The amount of heat dissipated (*P*) can be generally expressed as following:

$$P = \kappa \frac{T - Tw}{L2} A \quad (2)$$

Here *T* is the higher temperature in the device that drives heat dissipation, T_w is the atmosphere temperature, and *κ* is the thermal conductivity of the material, L_2 is the distance of heat dissipation, here it is proportional of the thickness of the device, and *S* is the heat dissipating area, which is the top/ bottom surface area.

In order to reduce temperature, we want a lower Joule heating and higher heat dissipation amount. Analyzing from the above equations, we can see that if we want to keep applied electric field constant, a smaller cross sectional area as well as a smaller voltage can reduce the total Joule heating amount. On the other hand, a larger dissipating area *S*, a shorter dissipating distance (i.e. a thinner device), and a material of higher thermal conductivity can facilitate heat dissipation.

According to this, we can see three fold reasons for the reduced temperature effect with enclosed device over the open chamber device:

1. Mass heat generation is smaller: The enclosed device has much smaller cross sectional area due to the use of an enclosed hydrogel structure and minimum buffer thickness on top of PA gel. The cross sectional area is 45 times smaller than the open chamber device (Figure A12). Furthermore, we reduced the distance between electrodes 3 times, so that only one third of the original voltage is needed to generate the same amount of electric field. This setting can reduce the massive Joule heating amount >100 times according to calculation based on equation (1).

2. Optimal heat dissipation geometry: In the enclosed device, the thin PA gel was enclosed between two glass slides. Geometrically, the heat dissipating distance from PA gel to surrounding atmosphere is ~2.6 times smaller than the open chamber device, resulting in a reduced thermal resistivity.

3. Thermal effective material is used. In the enclosed device, > 90% of the volume is thermal conductive glass slide and only <10% is hydrogel that participate in electrophoretical heat generation. This large ratio of glass material added to the thermal mass, acting as heat sink. In the future, replacing the glass slide with a material of better thermal conductivity, such as silicon (k_{Si} = 149 $Wm^{-1}K^{-1}$ compared to k_{SiO2} = 1.46 $Wm^{-1}K^{-1}$) can potentially result in a more uniform temperature of the device and better heat dissipation [5].

Although it might be hard to predict the actual temperature profile of the open chamber device and the enclosed device, we can make estimate based on the heat generating and dissipating amount to demonstrate the drastic temperature difference at steady state with the two device settings. In Figure A12, we describe the temperature profile from our analysis based on the above heat generation and dissipation equations to demonstrate the drastic effect of temperature reduction from enclosed device. It can be seen that the heat dissipation is so effective in the enclosed device that most of the heat is dissipated right away, and the gel temperature maintained at almost room temperature. However, due to the thick electrophoretic layer and a less thermal conductive acrylic material used in the open chamber device, the heat is mostly accumulated and caused drastic temperature increase. The highest temperature in the enclosed device is 294 K (21 ^{o}C) at a room temperature of 292K (19 ^{o}C), and 382 K (109 ^{o}C, or boiling temperature of buffer) for open chamber device. It needs to be noted that this analysis is for equilibrium condition, where dissipated heat is equal to generated heat, so that there is no further temperature increase. In the experimental conditions, the maximum temperature in the device is usually smaller than these values. However, this is a concrete illustration on the effect of enclosed device.

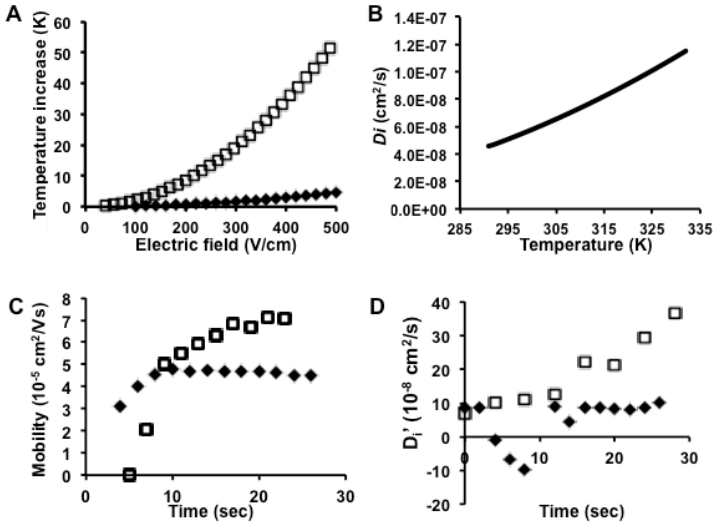

Figure A13. Effect of temperature reduction design. **(A)** Heat controlled design allows higher electric field application. The temperature increase is minimum even when higher electric field is applied. **(B)** Relationship of diffusion coefficient and temperature. **(C)** Measured electrophoretic mobility of OVA during 30 s of separation in an open chamber device and in the enclosed pattern gel. **(D)** Experimentally measured apparent diffusion coefficient of OVA during 30 s of separation in an open chamber device and in the enclosed pattern gel.

L. Additional Characterization of Separation Performance (Chapter 6)

We also measured the peak variance of OVA over 30 s of separation in the open chamber device and in enclosed patterned gel (Figure A14). The stacking

phenomenon resulted in even narrower peaks than the initial injection at the end of stacking. This helps to counteract the injection dispersion. After stacking, the peak variances increase at a slower rate in enclosed device than the ones in open chamber device. However, it seems that the peak variance control of OVA is less significant in enclosed device comparing with open chamber device, whereas the improvement on BSA is more obvious. We can explain this phenomenon by examining the diffusional loss. Since elevated temperature not only causes planar peak dispersion in open chamber device, but also causes a more rapid protein loss out of PA gel. This loss will contribute to the peak variance measurement as the edge area of protein spot will go below the detection limit, giving a seemly narrower peak width. This effect is more severe with smaller proteins, which have higher diffusion coefficient. This might be the reason that caused the seemingly smaller spots in the fluorescent images of BSA and OVA in open chamber condition and the less pronounced peak variance increase rate.

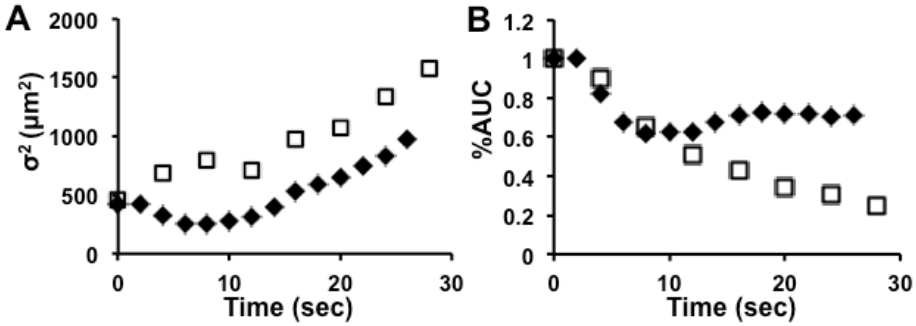

Figure A14. Additional comparison of separation performance. **(A)** Peak variance of OVA separated in an open chamber device and in the enclosed patterned gel. **(B)** OVA area under curve (AUC) normalized to the original injected signal indicates the protein retaining rate in the open chamber device and the enclosed patterned gel.

In the enclosed device setting, the protein retention rate increase as we effectively control temperature. As shown in Figure A14, the open chamber device causes ~70% protein loss during 30 sec electrophoresis due to Joule heating temperature increase, whereas the enclosed device only caused 40% protein loss for OVA. It is also seen that proteins with smaller molecular weight (OVA) is more prone to temperature change than larger proteins (BSA). The smaller retention rate of BSA may be explained by other material loss sources. The BSA sample contains several isomers, and smeared peaks of even higher molecular weight proteins were observed during BSA electrophoresis. These isomers may have reduced the BSA peak area intensity we tracked.

References

[1] Probstein, R. F., Physicochemical Hydrodynamics: An Introduction, 2nd ed., John Wiley & Sons, New York, 2006, 82-96.
[2] Sternberg, J. C., In Advances in Chromatography; Giddings, J. C., Keller, R. A., Eds.; Marcel-Dekker: New York, 1966; Vol. 2, pp 205-270.

[3] Taylor, G. I., Proc. R. Soc. London, Ser. A, 1953, 219, 186-203.
[4] Aris, R., Proc. R. Soc. London. Ser. A, 1956, 235, 67-77.
[5] Swinney, K., Bornhop, D. J., Electrophoresis, 2002, 23, 613– 620.